TECHNISCHE UNIVERSITÄT WIEN

Diese Dissertation haben begutachtet:

Prof. Dr. Wolfgang Wagner

……

Prof. Dr. Ralf Ludwig

……

DISSERTATION

Model improvements and error characterization for global ERS and METOP scatterometer soil moisture data

ausgeführt zum Zwecke der Erlangung des akademischen Grades eines Doktors der technischen Wissenschaftern unter der Leitung von

Univ. Prof. Dipl.-Ing. Dr. techn. Wolfgang Wagner
Institut für Photogrammetrie und Fernerkundung (E122)
Technische Universität Wien

eingereicht an Technische Universität Wien
Fakultät für Mathematik und Geoinformation
von

Vahid Naeimi

Mart. Nr. 0209123
Eduard Pötzl Gasse 7/3/15
A-1190 Wien

Wien, am 5.2.2009

This work was submitted as Ph.D. dissertation to the Faculty of Mathematics and Geoinformation of the Vienna University of Technology, Vienna, Austria.

Supervisor: Prof. Dr. Wolfgang Wagner
Institute of Photogrammetry and Remote Sensing, Vienna University of Technology
Gusshausstr. 27-29, 1040 Vienna, Austria. e-mail: ww@ipf.tuwien.ac.at

Reviewer: Prof. Dr. Ralf Ludwig
Department of Geography, Faculty of Geosciences, Ludwig-Maximilians-Universität München
Luisenstraße 37, 80333 Munich, Germany. e-mail: r.ludwig@lmu.de

Some parts of this study have been already published in a number of journal papers, technical reports, and conference contributions. A list of publications is given as follows:

Naeimi, V., K. Scipal, Z. Bartalis, S. Hasenauer and W. Wagner (2008), "An improved soil moisture retrieval algorithm for ERS and METOP scatterometer observations", *IEEE Transactions on Geoscience and Remote Sensing*, in press.

Naeimi V., Z. Bartalis, and W. Wagner, (2008) "ASCAT soil moisture: An assessment of the data quality and consistency with the ERS scatterometer heritage", *Journal of Hydrometeorology*, in press.

Naeimi, V., C. Kuenzer, S. Hasenauer, Z. Bartalis and W. Wagner (2007), "Evaluation of the influence of land cover on the noise level of ERS-scatterometer backscatter", *IGARSS*, Barcelona, Spain, 23-28 July 2007, pp. 3685-3688, DOI: 10.1109/IGARSS.2007.4423643.

Naeimi, V., W. Wolfgang, B. Zoltan and H. Stefan (2008), "One year of ASCAT soil moisture data", *Catchment-scale Hydrological Modelling & Data Assimilation International Workshop (CAHMDA-III Workshop)*, Melbourne, Australia, 9-11 January 2008.

Bartalis, Z., V. Naeimi, S. Hasenauer, W. Wagner (2008), "ASCAT Soil Moisture Product Handbook". *ASCAT Soil Moisture Report Series, No. 15*, Institute of Photogrammetry and Remote Sensing, Vienna University of Technology.

Abstract

Soil moisture is a key variable in the hydrologic cycle. The linkage between energy and water balance is provided through the moisture and temperature states of the soil at the soil surface/atmosphere interface. The evolution of soil moisture fields is important for numerical weather and climate models. Adequate knowledge of the soil moisture distribution is essential to predicting the mutual influence of land surface processes (e.g. evaporation, infiltration, and runoff) to weather and climate. Due to the high variability of soil moisture in time and space, a good spatio-temporal representation of the soil wetness conditions is demanding. In-situ ground observation methods of soil moisture are reasonably accurate but expensive. The other problem with in-situ measurements is that they are generally point measurements and represent small scale. Thanks to a strong relationship between water content and dielectric properties of soil, microwave remote sensing techniques have the potential to overcome the limitations of traditional methods providing areal measurements with global coverage and more frequent observations. Equally important to improved instrumentation and remote sensing techniques are the geophysical retrieval methods, which are used to extract soil moisture dynamics from microwave signal.

The scatterometers onboard the ERS and Metop satellites have been shown to be useful for monitoring soil moisture variations. The objective of thesis was to develop an improved soil moisture retrieval algorithm based on the so-called TU-Wien change detection method with new parameterization comprising an error analysis. The new algorithm, WARP5 (WAter Retrieval Package) results in a more robust and spatially uniform soil moisture product with a higher resolution than the earlier method (WARP4). Cross-comparisons of WARP4 and WARP5 datasets with field observations and also with modeled soil moisture data show that the new algorithm has a better performance and effectively corrects retrieval errors in certain areas. Parallel to soil moisture retrieval, a comprehensive uncertainty analysis is carried out. Uncertainty modeling is composed of a combined analytical error propagation and a numerical solution based on Monte Carlo simulation. Understanding the uncertainties in each processing step of the retrieval model is valuable for optimal soil moisture estimation and also for scientific applications especially for data assimilation.

Zusammenfassung

Bodenfeuchte ist eine wichtige Variable im hydrologischen Zyklus. Die Verbindung zwischen Energie- und Wasserhaushalt ist durch den Feuchtigkeits- und Temperaturzustand des Bodens an der Bodenoberfläche und Atmosphäre gegeben. Die Entwicklung von Bodenfeuchtedaten ist wichtig für die numerische Wettervorhersage und Klima-Modellierung. Die Kenntnis über die Verteilung der Bodenfeuchte ist essentiell für die Vorhersage des gegenseitigen Einflusses von Prozessen an der Bodenoberfläche (wie z.B. Evaporation, Infiltration und Abfluss) auf Wetter und Klima. Aufgrund der hohen Variabilität der Bodenfeuchte in Raum und Zeit, ist eine gute Raum-Zeit-Darstellung der Bodenfeuchte recht anspruchsvoll. In-situ Beobachtungsverfahren der Bodenfeuchte sind hinreichend genau, aber recht kostspielig. Ein weiteres Problem mit in-situ Messungen im Feld ist die Tatsache, dass diese in der Regel Punktmessungen sind und nur eine kleine Maßstabsskala abdecken. Aufgrund der engen Verbindung zwischen Wasser und den dielektrischen Eigenschaften des Bodens haben Mikrowellen-Fernerkundungsmethoden das Potenzial, die Grenzen der traditionellen Methoden zu überwinden, und darüber hinaus flächenhafte Messungen mit globaler Abdeckung und häufigeren Beobachtungen anzubieten. Gleichbedeutend mit einer Verbesserung der Instrumente und Fernerkundungstechniken sind die geophysikalischen Methoden, die verwendet werden, um die Dynamik der Bodenfeuchte aus den gemessene Mikrowellensignalen zu extrahieren.

Die Scatterometer an Bord der Europäischen Fernerkundungssatelliten ERS und MetOp haben sich als nützlich für die Überwachung der Bodenfeuchte erwiesen. Das Ziel dieser Dissertation war die Entwicklung eines verbesserten Algorithmus zur Ableitung von Bodenfeuchte, basierend auf der so genannten „TU-Wien Change Detection“ Methode mit einer neuen Parametrierung und Fehleranalyse. Der neue Algorithmus, WARP5 („WAter Retrieval Package“), führt zu einem robusteren und räumlich einheitlicheren Bodenfeuchteprodukt mit einer höheren Auflösung als mit der früheren Methode (WARP4). Eine Gegenüberstellung von WARP4 und WARP5 Datensätzen mit Feldbeobachtungen und mit modellierten Bodenfeuchtedaten zeigt, dass der neue Algorithmus über eine bessere Leistung verfügt und Fehler in bestimmten Bereichen wirksam korrigiert. Parallel zur

Ableitung der Bodenfeuchte wurde eine umfassende Fehleranalyse durchgeführt. Diese Fehleranalyse besteht aus einer Kombination von analytischer Fehlerfortpflanzung und einer numerische Lösung auf Basis einer Monte-Carlo-Simulation. Das Verständnis von Fehlern und deren Abschätzung in jedem Verarbeitungsschritt der Methode stellt einen wertvollen Beitrag für die optimale Bestimmung der Bodenfeuchte und auch für wissenschaftliche Anwendungen, insbesondere für die Datenassimilation, dar.

Acknowledgment

The research on which this thesis is based was carried out at the Institute of Photogrammetry and Remote Sensing (IPF) of the Vienna University of Technology (TU Wien). The funding was made available by the European Organization for the Exploitation of Meteorological Satellites, EUMETSAT (EUM/CO/05/1421/HGB) and Austrian Science Fund (L148-N10) projects.

I would like to thank all those who have contributed time and effort to this study. In the first place, I would like to thank Wolfgang Wagner. This work would not have been possible without his enthusiasm, inspiration and encouragement. Further, I am grateful to my co-advisor Ralf Ludwig for his kind comments and corrections.

I wish to thank my colleagues at IPF for providing a great research environment. My special thank goes to Hans Thüminger for his superior IT administration and the members of Radar group at the institute particularly Klaus Scipal, Zoltan Bartalis, Stefan Hasenauer and Marcela Doubkova for providing constructive discussions and their assistance.

I wish to express my appreciation to my mother and brother for their strong support and encouragement during the course of my studies. I am also indebted to my father for his care and love. Although he is no longer with us, he is forever remembered. Above all, I would like to thank my wife Farnaz who stood beside me and encouraged me constantly with great patience all the time.

Contents

List of Symbols and Acronyms

ε	Relative permittivity, Dielectric constant
ε'	Real component of ε (Permitivity)
ε''	Imaginary component of ε (loss factor)
θ	Incidence Angle
φ	Azimuthal Angle
σ^0	Radar cross-section, Backscattering coefficient
σ^0_{fore}, σ^0_{mid}, σ^0_{aft}	Backscattering coefficient measured respectively by the fore, mid, aft beam antennas
δ	Difference of backscatter measured by the fore and aft beam antennas
σ'	First derivative of σ^0, Slope
σ''	Second derivative of σ^0, Curvature
C', C''	Constant terms of functions describing the seasonal variation of σ' and σ'' in WARP4
D', D''	Dynamic range of functions describing the seasonal variation of σ' and σ'' in WARP4
$\psi'(t)$, $\psi''(t)$	Empirical periodic functions describing the seasonal variation of σ' and σ'' in WARP4
σ^0_{dry}, σ^0_{wet}	Backscatter from driest/wettest soil surface
θ_{dry}, θ_{wet}	Crossover angles for dry/wet soil conditions
C^0_{dry}, C^0_{wet}	Annual min. and max. backscatter at dry/wet crossover angles
Θ_S	Saturated water content
Θ_{FC}	Field Capacity
Θ_{PWP}	Permanent Wilting Point
Θ_R	Residual Water Content
Θ_{PAW}	Plant Available Water
t	Time
τ	Time window length used for calculation of slope and curvature
T	Optical depth
$\xi_{instrument}$	Instrumental noise
ξ_θ	Uncertainty of incidence angle

$\xi_{\sigma'_{40}}$	Noise of slope at 40° incidence angle
$\xi_{\sigma''_{40}}$	Noise of curvature at 40° incidence angle
$\xi_{\sigma(40)}$	Noise of normalized backscatter at 40° incidence angle
$\xi_{\sigma_{dry}(40)}$, $\xi_{\sigma_{wet}(40)}$	Uncertainties related to dry and wet references
ξ_{Θ}	Estimated noise of soil moisture
AMI	Active Microwave Instrument
ASCAT	Advanced Scatterometer onboard Metop
DGG	Discrete Global Grid
ECMWF	European Center for Medium-range Weather Forecasts
EPS	EUMETSAT Polar System
ERS	European Remote Sensing satellites
ESA	European Space Agency
ESD	Estimated Standard Deviation of backscatter
EUMETSAT	European Organization for the Exploitation of Meteorological Satellites
FWI	Fractional Water Index
GPI	Grid Point Index
GSWP	Global Soil Moisture Project
ITCZ	Intertropical Convergence Zone
Kp	Radiometric resolution of the scatterometer
MC	Monte Carlo method
Metop	METeorological OPerational satellites
NDVI	Normalized Difference Vegetation Index
R	Correlation Coefficient
RMSE	Root Mean Square Error
SAF	Satellite Application Facility
SAR	Synthetic Aperture Radar
SCAT	Scatterometers onboard ERS-1 & ERS-2
TDR	Time Domain Reflectometry
TU Wien	Vienna University of Technology
WARP	WAter Retrieval Package

1. Introduction

1.1. Water Cycle

Water is the most spread substance among other natural resources on the Earth. It is available everywhere and plays a crucial role in human life and surrounding environment. The world's water exists naturally in different forms and locations: in the air, on the surface, below the ground and in the oceans. About 97.5% of the Earth's water forms the oceans and just 2.5% is freshwater, which most of it is frozen in glaciers and ice sheets or stored underground. The remaining small fraction of the world's freshwater is found in the atmosphere and on the surface as rivers, lakes, wetlands or in form of precipitation, soil moisture and plant water content. Figure 1-1 illustrates the global water distribution on the Earth (UNESCO 2006). Water circulates naturally, unlike most other natural resources, and is constantly recharged forming a closed hydrological cycle driven by the sun (Figure 1-2). The principal natural components of this cycle are precipitation, infiltration into the soil, runoff on the surface, groundwater discharge to the surface waters and oceans, evaporation from water bodies and soil, and evapotranspiration from plants. Water is transferred around our planet in this continuous cycle and changes between being solid, gas or liquid. When water is used, it loses properties such as purity, heat content, and potential gravitational

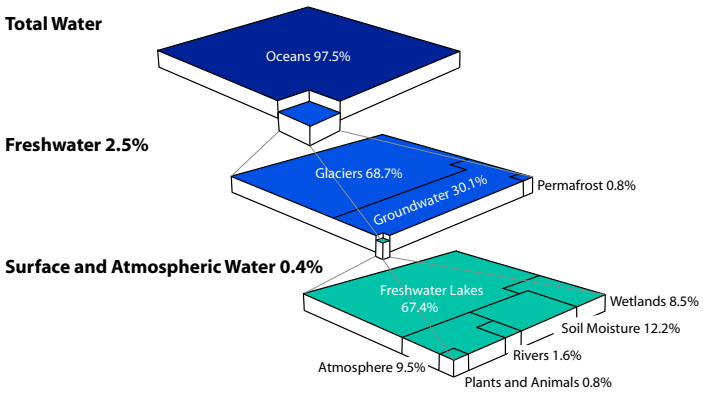

Total Water		
Oceans	97.5	%
Glaciers	1.7175	%
Groudwater	0.7525	%
Permafrost	0.02	%
Freshwater Lakes	0.00674	%
Soil Moisture	0.00122	%
Atmosphere	0.00095	%
Wetlands	0.00085	%
Rivers	0.00016	%
Plants and Animals	0.00008	%

UNESCO 2006

Figure 1-1. Global Water Distribution (source: UNESCO).

energy but eventually most degraded water resources are refreshed by natural processes in the hydrological cycle that is mostly driven by solar energy.

Of most importance for human being in global water cycle is freshwater, which is generally thought of as renewable resource, although it is very dependent on other parts of the hydrologic cycle. Freshwater is essential for the survival of humans and is required for drinking, agriculture and other uses. Even though the freshwater is naturally recycled, the circulation rate, which is determined by the climate system, has strong impact on human life and is the main focus in water resources assessments (Oki and Kanae 2006). A large part of the freshwater that returns to the atmosphere passes through soil and plants. Therefore an important part of water cycle is evapotranspiration process. Evaporation accounts for the movement of water to the air from sources such as the soil, canopy interception, and water bodies while transpiration accounts for the movement of water within a plant and the subsequent loss of water as vapor through stomata in its leaves. Types of soil and vegetation significantly affect evapotranspiration and therefore the amount of water leaving a watershed. Factors that affect evapotranspiration include the plant's growth stage or level of maturity, percentage of soil cover, solar radiation, humidity, temperature, and wind. Figure 1-3 shows the energy and water balance including terrestrial and atmospheric components of water cycle.

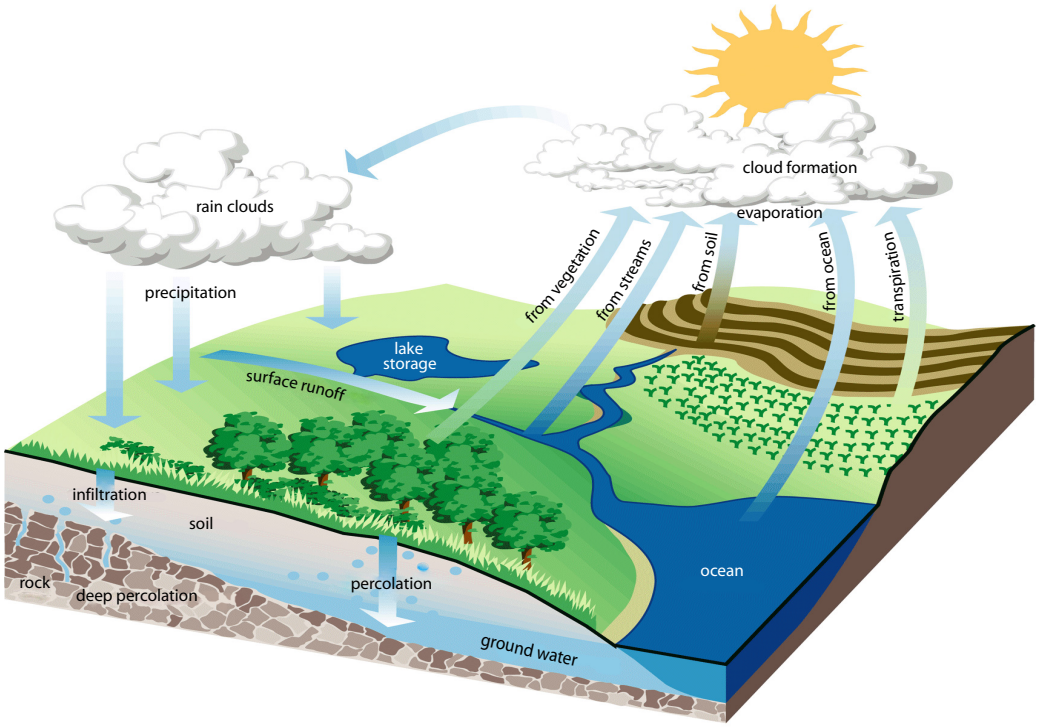

Figure 1-2. Hydrologic cycle.

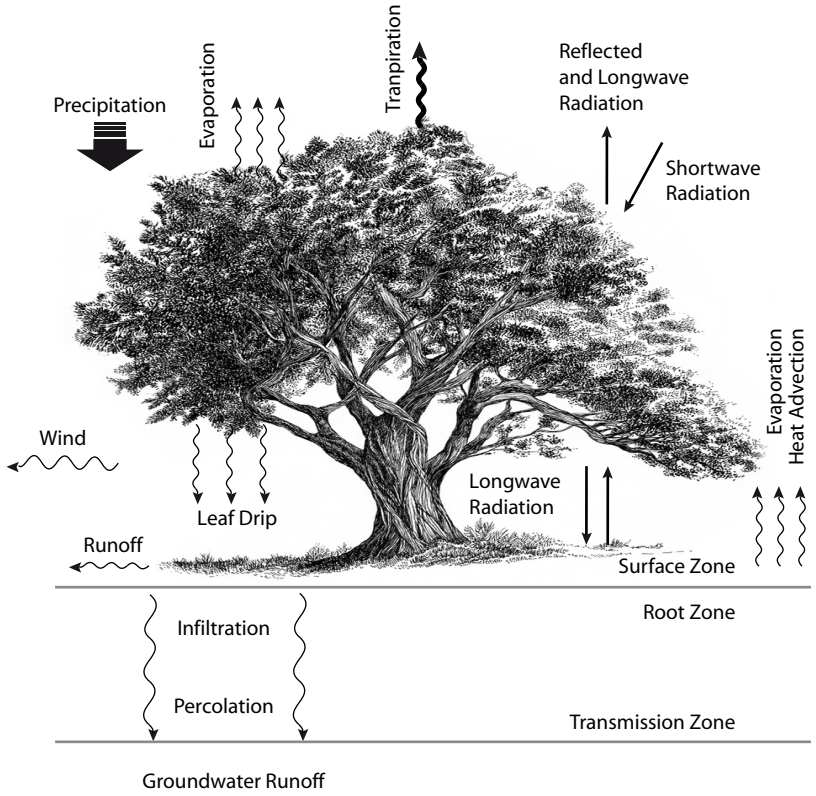

Figure 1-3. Terrestrial and atmospheric components of the water cycle (source: ESA).

1.2. Soil Moisture

Soil moisture is defined as the fraction of water contained in the soil and can be expressed in various ways on a volumetric or gravimetric basis (Hillel 1998). Although the volume of soil moisture compared to other components of water cycle is small, it is of major importance to hydrological and natural environmental processes. Soil moisture is a key variable in controlling the exchange of water and heat energy between the land surface and the atmosphere through evaporation and plant transpiration. It functions like a switch that controls infiltration into the soil sub-layers and the amount of precipitation that runs off into nearby streams. It also has influence on the rate of water absorption by the vegetation, drainage, ground stability, and near-surface climate. As a result, soil moisture information is valuable to a wide range of disciplines and applications concerned with weather and climate, early warning of droughts, runoff potential and flood control, irrigation scheduling, soil erosion and slope failure, crop yield forecasting, reservoir management, and water quality.

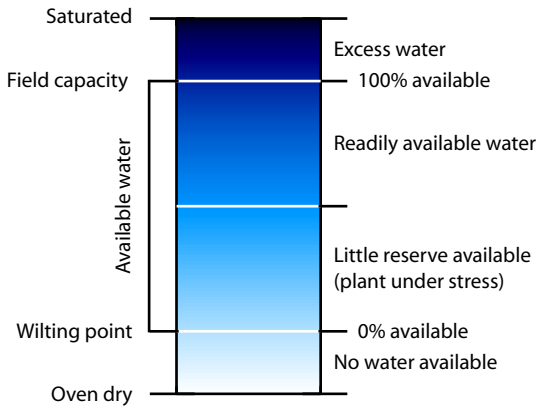

Figure 1-4. Available water in the soil.

In the Earth and agriculture sciences, soil moisture is usually measured and used in four standard quantitative levels. 1) Saturated water content Θ_S : fully saturated water, which is free to percolate down through the soil profile, equivalent to effective porosity, 2) Field capacity Θ_{FC} : amount of water remaining in the soil after percolation has occurred, 3) Permanent wilting point Θ_{PWP} : soil moisture content where most plants would experience permanent wilting, 4) Residual water content Θ_R at high tension. The amount of water between field capacity and wilting point is generally considered as plant available water content Θ_{PAW} (Figure 1-4). The amount of soil water content varies by soil type depending on soil texture, organic matter content, and structure.

Soil moisture can be measured either directly using gravimetric soil sampling or indirectly using other in-situ measurement techniques or airborne/spaceborne remote sensing. Among in-situ measurement techniques of soil moisture, the gravimetric method is a direct and absolute technique for estimating the total water content of soils. The method involves drying a soil sample in an oven (105°C) to determine the amount of water in the soil by subtracting the dry soil weight from the initial field soil weight. The weight of the water is then divided by the dry soil weight to obtain the water content by weight. Soil moisture can be also measured in volumetric basis by multiplying gravimetric water content by specific gravity of soil (Hillel 1998). This method is time consuming, labor-intensive, and requires sampling equipment. Since this method is destructive, samples cannot be taken from exactly the same point on subsequent sampling dates. Hence gravimetric soil sampling is commonly used to calibrate indirect methods. There are a variety of indirect methods for in-situ soil moisture measurements. Time Domain Reflectometry (TDR) is a newer technology based on sensing the soil dielectric constant, which increases with the water fraction of the soil (Topp et al. 1980). In this method TDR device transmits a high frequency

pulse along a cable attached to parallel probes inserted into the soil and measures the time it takes for the electromagnetic wave to travel through the soil between the probes. The velocity of transmitted signal decreases with increasing the soil dielectric constant.

The in-situ measurements are generally accurate and provide soil moisture measurements over entire root zone. The problem of traditional in-situ measurement techniques is that they are basically point measurements. Soil moisture is highly variable in time and space. Therefore a large number of samples must be taken to overcome the natural spatial variability of soils and water content. The spatial variability of soil moisture results from many processes including vertical and lateral redistribution over scales from centimeters to tens or hundreds of meters (Western et al. 1998). Variability of soil moisture can be divided in two components: the large scale forced by the atmosphere determined by precipitation and evaporation patterns, and the small scale determined by soils, topography, vegetation and root structure (Entin et al. 2000). Because of strong spatial variability of soil moisture at small scale and also logistic constraints, it is very difficult to estimate catchment average soil moisture from point measurements.

1.3. Soil Moisture Remote Sensing

Technical advances recently made in remote sensing of soil moisture are encouraging compared to the traditional in-situ soil moisture measurement, which demands intensive labor and field activities. Soil moisture remote sensing methods have the advantage of performing an automatic averaging over entire area (or footprint) that may range from a few square meters to thousands of square kilometers depending on the sensor resolution. Additionally airborne and spaceborne remote sensing techniques make it possible to acquire soil moisture data with regional or global coverage regularly and more frequent than in-situ measurements.

Since the 1970s various remote sensing methods using different sensor types operating in visible, infrared, and microwave parts of the electromagnetic spectrum have been employed for soil moisture measurement. Visible and thermal spaceborne data have been used to extract soil moisture indirectly through monitoring surface temperature and other surface state variables (Verstraeten et al. 2006) whereas microwave remote sensing specially in low frequency domain (1-10 GHz) offers a relatively direct method of soil moisture retrieval thanks to the strong relationship between the moisture content and dielectric constant of the soil (Ulaby et al. 1982). Since availability of spaceborne microwave sensors, numerous theoretical, empirical, or semi-empirical techniques have been developed to retrieve geophysical parameters from microwave data. The most important frequency bands suitable

for soil moisture retrieval reported in these studies are: L-band (1-2 GHz), C-band (4-8 GHz), and X-band (8-12.5 GHz). Figure 1-5 illustrates suitability of some of the current and future operational missions for soil moisture retrieval (Wagner et al. 2007).

1.3.1. Microwave Satellite Systems and Soil Moisture Retrieval Methods

Microwave remote sensing sensors can be divided into two types: passive sensors (radiometers) and active sensors (radars). Passive sensors are designed to measure radiation emitted by the Earth surface whereas active remote sensing systems transmit their own

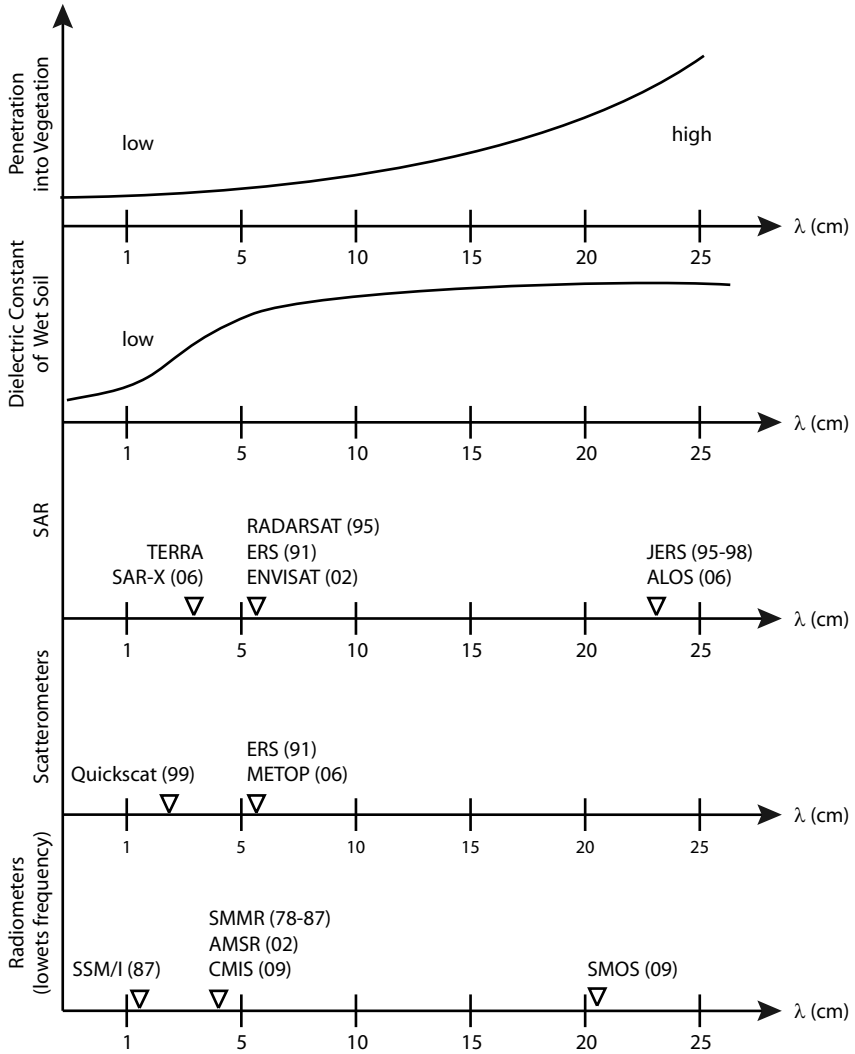

Figure 1-5. Microwave sensors suitable for soil moisture retrieval. Low frequency microwave measurements are known to be beneficial for soil moisture retrieval due to their capability to better penetrate vegetation (top) and the high sensitivity to the dielectric constant of the soil (second from top) (Wagner et al. 2007).

electromagnetic emanation to the target and record the energy reflected or scattered back to the sensor. Despite the different measurement processes, active and passive methods are closely linked through Kirchhoff's law which states that the emissivity is one minus the hemisphere integrated reflectivity (Schanda 1986).

Passive Microwave Systems

Radiometers measure the brightness temperature, which includes contributions from the soil, vegetation, and atmosphere (and snow cover if present). The primary geophysical variables influencing the brightness temperature are soil moisture, vegetation water content, and surface temperature. Other factors such as surface roughness, vegetation type, and soil texture are also important (Njoku et al. 2003). In general, soil moisture retrieval algorithms developed in recent years, are mostly based on inversion of microwave radiative transfer models that link surface geophysical variables to the observed brightness temperature. The retrieval methods are mainly different in their correction approaches for vegetation and surface temperature effects. Since 1987 several spaceborne microwave radiometers have been employed for soil moisture measurement such as the Scanning Multichannel Microwave Radiometer (SMMR) on the Nimbus-7 Satellite, the Special Sensor Microwave Imager (SSM/I) on the Defense Meteorological Satellite Program (DMSP), the Tropical Rainfall Measuring Mission (TRMM) Microwave Imager (TMI) onboard the TRMM satellite, and the Advanced Microwave Scanning Radiometer-Earth Observing System (EOS) (AMSR-E) onboard NASA's EOS Aqua Satellite. There are also missions in preparation such as the Soil Moisture and Ocean Salinity (SMOS) and the Conical-scanning Microwave Imager/Sounder (CMIS). A large number of studies have investigated the use of passive microwave sensors for soil moisture retrieval such as (Schmugge et al. 1974) (Eagleman and Lin 1976) (Wang and Schmugge 1980) (Jackson et al. 1982) (Wigneron et al. 1993) (Njoku and Entekhabi 1996) (Vinnikov et al. 1999) (Owe et al. 2001) (Kerr et al. 2001) (Entekhabi et al. 2004).

Active Microwave Systems

Radar systems measure the backscattering coefficient that is relative to the energy scattered back from the Earth's surface. There are two types of radars which have the potential for soil moisture retrieval: Synthetic Aperture Radars (SAR) and scatterometers.

A) Synthetic Aperture Radar (SAR)

SAR is a coherent radar system that generates high resolution images by processing the received signals. The backscatter signals received from the many pulses illuminating a specific target are combined into a well-focused, high resolution image. SAR systems are

normally capable to measure backscattering coefficient in different polarization modes. The first SAR was used by NASA on JPL's Seasat oceanographic satellite in 1978. Since 1990s several satellites carrying SAR onboard have been launched such as ESA's European Remote Sensing satellites (ERS-1 & ERS-2) and ENVISAT, Canada's RADARSAT series working at C-band, Japan's satellites JERS-1 and ALOS working at L-band, and Germany's Terra SAR-X working at X-band.

The intensity of the backscattering signal measured by radars depends on surface roughness, soil water content, vegetation cover, and local incidence angle of radar's beam. Experimental relationship between radar backscatter and soil moisture using empirical models have been investigated in several studies including (Oh et al. 1992), (Dubois et al. 1995), (Cognard et al. 1995), (Ahmed 1995), (Deroin et al. 1997), (Wigneron et al. 1999), (Quesney et al. 2000), (Moran et al. 2000), (Oldak et al. 2003), (Alvarez-Mozos et al. 2005). In these studies soil moisture was generally retrieved by applying theoretical bare soil scattering models such as the Integral Equation Model (IEM) (Fung et al. 1992) and vegetation models similar in form to the so-called Cloud Model (Attema and Ulaby 1978) or site-specific vegetation growth models like the one used by (Mougin et al. 1995). These approaches, in spite of their complexity, are all site-dependent and fail to accurately describe the interaction between the electromagnetic wave and the Earth's surface. Although it has not yet been demonstrated that currently available single-frequency C- and L-band SAR systems can be used for operational soil moisture applications at the field scale, still it appears feasible to implement change detection algorithms for monitoring changes in soil moisture conditions at regional scales. However, the implementation of such change detection approaches requires significant efforts to build up long SAR backscatter time series and in-situ soil moisture series for region-dependent model calibration (Wagner et al. 2007). Currently several countries are preparing for launching the next generation of land-surveying SAR satellites. Future SAR satellites will be more advanced with different polarizations and imaging modes. Combination of different frequencies, polarizations, and incidence angles can be of assistance in soil moisture retrieval (Baronti et al. 1995), (Ferrazzoli et al. 1997), (Hajnsek et al. 2003).

B) Scatterometer

Scatterometers are radars with multi-incidence angle measurement capability which have been initially designed to measure wind speed and direction at the sea surface. Recent studies showed that these instruments can also be useful for land applications. Scatterometers have been flown on space missions since the early 1970s. The first scatterometer in space flew as part of the crewed Skylab missions in 1973 and 1974, and demonstrated that spaceborne scatterometers were feasible. Investigations on the potential

use of scatterometers in geosciences achieved a major technical milestone with the launch of Seasat, carrying a Ku-band scatterometer (SASS), in 1978. Other missions have followed SASS, including the C-band European Space Agency's (ESA) Earth Remote Sensing (ERS-1 & ERS-2) mission in 1991 and 1995, the NASA Scatterometer (NSCAT) mission in 1996, SeaWinds on QuikSCAT in 1999, SeaWinds on ADEOS-II in 2003, and Advanced Scatterometer (ASCAT) onboard Metop-A launched in 2006.

Scatterometers are very similar to SAR systems in terms of soil moisture retrieval capability. Also here the major challenge of retrieving soil moisture is the presence of additional factors influencing the signal such as surface roughness and vegetation. Most studies have used inversion methods based on physical approximations of scattering process to model roughness and vegetation (Frison et al. 1997), (Pulliainen et al. 1998), (Woodhouse and Hoekman 2000), (Magagi and Kerr 2001), (Jarlan et al. 2002), (Zine et al. 2005). Although theoretical models are useful in understanding and interpreting scattering behavior of natural surfaces, the major problems of these retrieval concepts appear to be their physical validity at large scales and their parameterization. For example Davidson *et al.* (Davidson et al. 2000) demonstrated the limited range of validity of currently available bare soil backscatter models. Grippa and Woodhouse (Grippa and Woodhouse 2002) noted the difficulty of modeling backscatter from heterogeneous land cover and pointed out the need to further investigate scaling processes. A possible solution to these problems is using change detection methods rather than using complex models to describe the full range of parameters influencing the scattering process. Availability of several years of backscatter data, multi-viewing capability, and high temporal sampling rate of scatterometers make them appropriate instruments for this purpose. Wagner *et al.* (1999) presented a change detection method by utilizing the unique sensor design of the ERS scatterometers. The core of this method is described in chapter 3 in more details.

1.4. Physical Principles of Scatterometry

In microwave remote sensing the distinction between different objects on the ground is basically caused by the difference in the signal strength received by the microwave receiver sensor. Hence, the measurement of received signal strength is the most important measurement in remote sensing devices. This characteristic of the remote sensing microwave instruments is different from typical radar, where a measurement of position is often the most important characteristic of the system, and measurement of the amplitude of the signal is unimportant (Ulaby et al. 1982). The extent to which an object reflects or scatters radio waves is called its radar cross section, which is determined by the structure and the dielectric properties of the observed target.

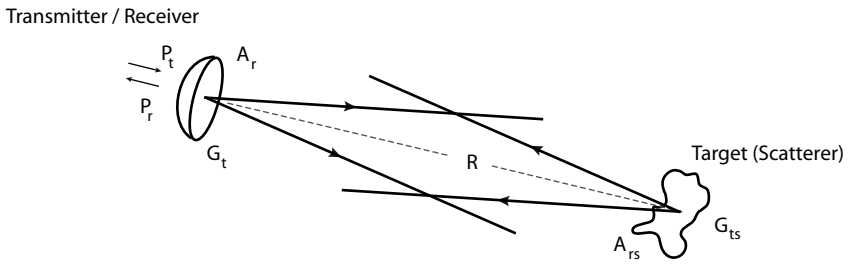

Figure 1-6. Illustration of the quantities involved in the radar equation.

1.4.1. Radar Equation

The fundamental relation between the characteristics of the radar, the target, and the received signal is called *Radar Equation*. The geometry of scattering from an isolated radar target (scatterer) is shown in the Figure 1-6 , along with the parameters that are involved in the monostatic radar equation (Ulaby et al. 1982):

$$P_r = \frac{P_t G_t A_r A_{rs} (1 - f_a) G_{ts}}{(4\pi)^2 R^4} \tag{1-1}$$

where P_t and P_r are transmitted and received power by the antenna with gain G_t. A_r is the effective aperture of the receiving antenna and A_{rs} is the effective area of the incident beam intercepted by the scatterer. f_a is the absorbed fraction of power by the scatterer and R is the distance between radar and target.

The factors associated with the scatterer are difficult to measure individually, and their relative contributions are uninteresting to one wishing to know the size of the received radar signal. Hence they are normally combined into one factor, the radar scattering cross-section:

$$\sigma = A_{rs} (1 - f_a) G_{ts} \tag{1-2}$$

The average value of the individual subtargets cross-sections per unit area is defined as differential scattering coefficient (or backscatter cross-section):

$$\sigma^0 = \left\langle \frac{\sigma_i}{\Delta A_i} \right\rangle \tag{1-3}$$

The backscatter cross-section is usually expresses in dB, which is given by:

$$\sigma^0(dB) = 10\log\sigma^0(m^2 m^{-2}). \tag{1-4}$$

Equation (1-1) can be reexpressed as

$$\overline{P}_r = \frac{\lambda^2}{(4\pi)^3}\int_{\substack{\text{area}\\ \text{illuminated}}} \frac{P_t G^2 \sigma^0 dA}{R^4}, \tag{1-5}$$

since the effective area of an antenna is related to its gain by

$$A = \frac{\lambda^2 G_t}{4\pi} \tag{1-6}$$

1.4.2. Scattering Mechanism

When an electromagnetic wave impinges from above upon the boundary surface between two semi-infinite media, a portion of the incident energy is scattered backward and the rest is transmitted forward into the lower medium. In the special situation where the lower medium is homogeneous or can be considered as such, the problem in question is *surface scattering* problem, since scattering takes place only at the surface boundary. It is seen that the scattering amplitude along the specular direction decreases while backscattering increases as the surface gets rougher. On the other hand, if the lower medium is inhomogeneous or is a mixture of materials of different dielectric properties, then a portion of the transmitted wave scattered backward by the inhomogeneities may across the boundary surface into the upper medium. In this case scattering takes place within the volume of the lower medium and is referred to as *volume scattering*. The mechanism of volume scattering causes a redistribution of the energy in the transmitted wave (Ulaby et al. 1982). Qualitative illustrations of different scattering conditions are shown in Figure 1-7. Reflection from a smooth surface boundary is called specular reflection. In this case no energy is scattered backwards to the sensor, except for normal incidence. The solution for

specular case is given by Fresnel reflection laws. When the surface is slightly rough the incident wave will partly reflected in the specular direction and partly scattered in all directions. The reflected specular component is often referred as the coherent because the phase front of the coherent wave is conversed and the scattered component referred as the diffuse or noncoherent component. As the surface becomes rougher, the coherent component becomes negligible. For very rough surface, the radiation pattern approaches that of Lambertian surface, which consists of only diffuse scattering. Figure 1-8 illustrates the angular radiation patterns of the backscattering coefficient for different surfaces.

Roughness is a relative concept depending upon wavelength and incidence angle. A surface is considered "rough" if its surface structure has dimensions that are comparable to the incident wavelength. A given surface that may appear very rough to an optical wave, may appear very smooth to a microwave. According to the Rayleigh criterion, a surface is considered rough if:

$$h > \frac{\lambda}{8 \cdot \cos\theta} \tag{1-7}$$

where h is mean height of surface variations, λ wavelength, and θ incidence angle.

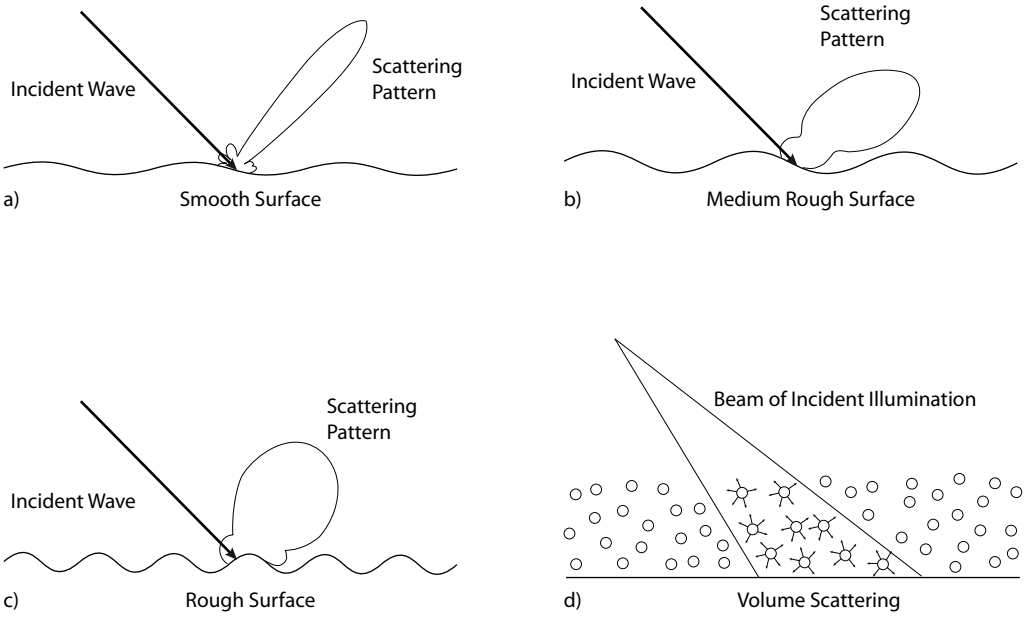

Figure 1-7. Surface and volume scattering patterns (after Ulaby et al. 1982).

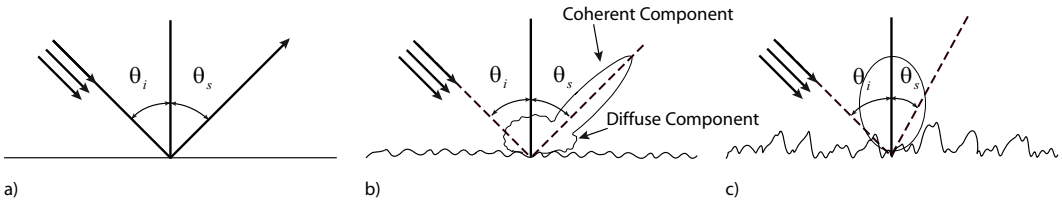

Figure 1-8. Contributions of coherent and diffuse scattering components for different surface roughness conditions: a) specular, b) slightly rough, c) very rough (after Ulaby et al. 1982).

The frequency of the incident wave determines also the penetration depth. Penetration depth tends to be longer with longer wavelengths. In addition to the frequency, the moisture content of the target influences the penetration depth. For example for C-band microwaves it varies from about 10 cm when dry to less than 1 cm when wet. This is because of the increasing of the dielectric loss factor (as is described below) of the water with respect to other natural materials that provokes a change in penetration depth of microwave.

1.4.3. Dielectric Properties of Natural Mediums

The behavior of the matter under the influence of the electric field of a propagating wave is characterized by dielectric properties of the materials. The reaction of materials to the electric field is caused microscopically by polarization/displacement of charge carriers, which are contained in the material. The materials which are neither perfect conductive nor perfect transparent to the electromagnetic radiation are dielectric mediums or lossy mediums (mediums that absorb some electromagnetic radiation). The dielectric property of mediums that influences radar returns is referred to as dielectric constant, which is described as a complex number and consists of two parts (permittivity and conductivity) that are both highly dependent on the moisture content of the material considered. When incident microwave radiation strikes the interface between two media with different dielectric properties, the wave form is changed and undergone attenuation if the medium is able to absorb or scatter the wave. The complex dielectric constant of material ε is given as:

$$\varepsilon = \varepsilon' - j\varepsilon'' \tag{1-8}$$

where ε' is permittivity or dielectric constant of the material, the real component defining the velocity and wavelength of the refracted wave in the material; and ε'' is the dielectric loss factor, the imaginary component expressing energy lost through absorption of the wave in the medium.

The relative dielectric constants of some materials are given in Table 1-1. By convention, the relative dielectric constant is defined as the absolute dielectric constant divided by the

dielectric constant of free space. In the microwave region, most natural materials have a dielectric constant between 3 and 8, in dry conditions. Amongst naturally abundant materials, liquid water shows strong orientational polarization and has a high dielectric constant. As a result, a change in moisture content generally provokes a significant change in the dielectric properties of natural materials.

Dielectric Constant of Soil

The dielectric properties of soil are governed by the volumetric moisture content and to a lesser extend by soil type and textural composition. In the absence of liquid water the real part of the dielectric constant ε' varies over the range from two to four and the imaginary part ε'' is typically lower than 0.05 (Ulaby et al. 1986). A wet soil medium is a mixture of soil particles, air pockets, and liquid water. Hallikainen *et al.* (1985) evaluated the microwave dielectric behavior of soil-water mixtures as a function of water content, temperature, and soil textural composition for different soil types at frequencies between 1.4 and 18 GHz. As moisture content of soil increases, both components of the complex dielectric constant, real and imaginary, increase. This rate of increase is frequency dependent. As frequency increases in the microwave spectrum, the sensitivity to increasing soil moisture decreases for the real component and increases for the imaginary component. Contrary, for dry soil die dielectric constant is essentially independent of soil texture and frequency. These relationships are illustrated in Figure 1-9 for a loamy soil (Ulaby et al. 1986). When soil temperature drops below 0°C, dielectric constant decreases strongly because when water freezes polarization by orientation is not possible any longer. Hence the dielectric properties of a frozen soil are similar to the dry soil. However, some soil water does not freeze even at temperatures around -50°C and therefore ε of the frozen soil still shows some dependency on the moisture content before freezing.

Table 1-1. Relative static permittivities (dielectric constants) of some materials.

Vacuum	1.0 (by definition)	**Water**	
Air	1.00054	At 0°C	88.0
Paper (Dry)	2.0	At 18°C	81.1
Rubber	3.0	At 40°C	73.4
Diamond	5.5 - 10.0	**Sulfuric Acid**	100.0 (25°c)
Salt	3.0 - 15.0	**Methanol**	32.6 (25°c)
Wood, Dry	2.0 - 6.0	**Gasoline**	2.0
Wood, Wet	10.0 - 30.0	**Paraffin-Oil**	2.1
Graphite	12.0 - 15.0	**Heavy Oil**	3.0

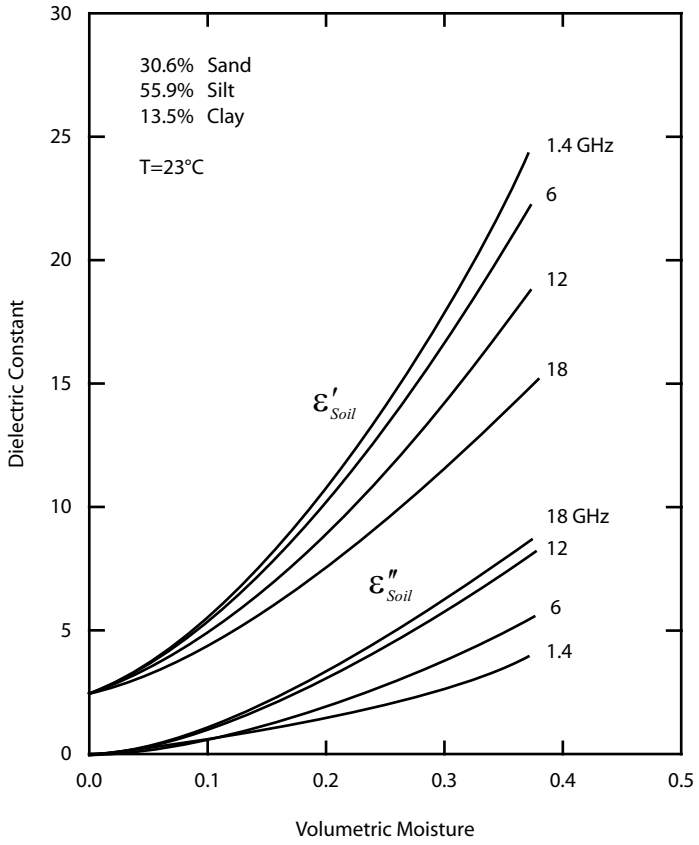

Figure 1-9. Measured dielectric constant as a function of volumetric moisture content for a loamy soil at four microwave frequencies.

1.5. Uncertainty Analysis

An experiment aimed to determine the numerical value of a physical variable will be affected from errors due to instrumentation, data acquisition and reduction limitations, methodology, environmental factors and so on. Therefore determination of truth requires estimation of the experimental errors, which is referred to as uncertainty analysis. Different sources of uncertainty include statistical error/random variation of replicate measurements, spatial and temporal variability, systematic error (bias), unrepresentative samples, and uncertainty in data reduction function (Stern et al. 1999). Here we discuss about the uncertainties made because of knowledge deficiency which should be distinguished from measurement variability. Uncertainties due to lack of knowledge can be separated into two categories: Those that resulted from fluctuations in measurements and those associated with the theoretical description of our result (Bevington 1969). It is important to differentiate

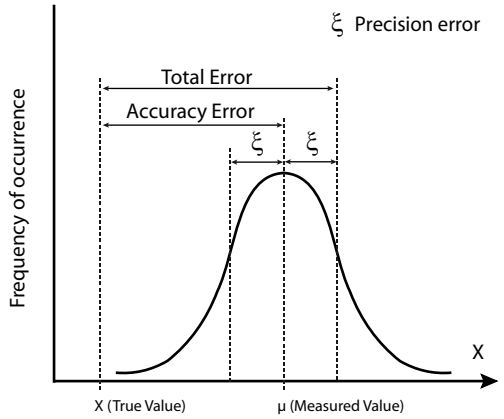

Figure 1-10. Accuracy, precision, and total error of measurement.

between the terms *accuracy* and *precision*. Measurement uncertainty is related with the systematic and random error and depends on both the accuracy and precision of the measurement. The accuracy is the degree of closeness of a measured or calculated quantity to its actual (true) value. The precision is the degree to which further measurements or calculations show the same or similar result. Difference between the measured and true value indicates total error (Figure 1-10). The least the accuracy and precision of experiment are, the larger the measurement uncertainty is.

In general, we are not able to determine the actual error in the result if no true data are available for evaluation of the experimental model. Therefore we need to develop a consistent error model for uncertainty determination. There are many analytical and numerical methodologies of uncertainty analysis including: 1) analytical variance propagation equation; 2) sensitivity analysis (Cacuci 1981), in which the partial derivatives of the model response with respect to the parameters are used to estimate uncertainty; 3) Monte Carlo analysis (Morgen 1984); 4) nonprobabilistic methods (e.g. fuzzy sets, fuzzy arithmetic) (Klir and Folger 1988)

1.5.1. Forward Uncertainty Propagation

Uncertainty can be propagated using prior assumptions about the different sources of uncertainty without the use of additional data. The assumptions that need to be made, include information about the distribution for input parameters. In forward feeding uncertainty analysis it is assumed that all the approximations made are correct or negligible and that the methodology/model is reasonable representative of the real physical system. Figure 1-11 illustrates a simple schematic map of forward error propagation.

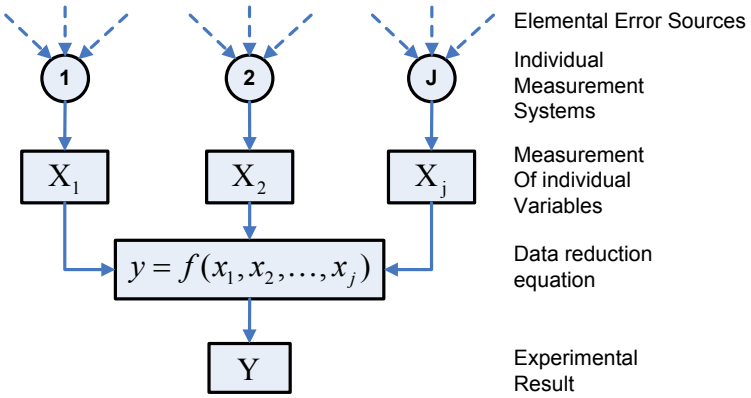

Figure 1-11. Uncertainty propagation diagram.

Error Propagation Equation: Method of Moments-design

We often want to determine a variable y that is a function of one or more different measured variables $y = f(u,v,\ldots)$. We must know how to propagate the uncertainties in the measured variables to determine the uncertainty in the dependent variable (Bevington 1969). The method of moments is a very general technique for estimating the moments of y-its first moment (mean), its second moment (variance or standard deviation), its third moment (skewness) based on various approximations to the function f. The most commonly used form, called first-order second-moment uncertainty analysis, estimates the second moment of y (its spread), based on a first-order approximation to f (that is, approximating the function f by a flat plane tangent to the curved surface of f at the mean of $u,v,\ldots$. Higher-order approximations are possible but they are rarely used because they are much more complex to calculate, and require higher moments (skewness, kurtosis, etc.) of the input variables, which are difficult to estimate reliably (Kirchner 2001). The simplest case is a single-variable function $y = f(x)$ (Figure 1-12). f can be approximated as the tangent line (which has a slope of dy/dx) at the mean of x. The standard error of y is approximated as:

$$s_{\bar{y}} \approx \left|\frac{dy}{dx}\right| s_{\bar{x}} \tag{1-9}$$

where $s_{\bar{y}}$ the uncertainty in y, which depends on the uncertainty of x, $s_{\bar{x}}$ and how sensitive y is to x (that is, dy/dx).

In a more general case $y = f(u,v,\ldots)$, the deviation of y can be expressed as a function of the deviations in $u,v,\ldots$:

$$y_i - \bar{y} \approx (u_i - \bar{u})\left(\frac{\partial y}{\partial u}\right) + (v_i - \bar{v})\left(\frac{\partial y}{\partial v}\right) + \cdots \tag{1-10}$$

Then the variance of y using equation (1-10) is expressed as:

$$s_y^2 \approx \frac{1}{1-N}\sum_i^N (y_i - \bar{y})^2 = \frac{1}{1-N}\sum_i^N \left[(u_i - \bar{u})\left(\frac{\partial y}{\partial u}\right) + (v_i - \bar{v})\left(\frac{\partial y}{\partial v}\right) + \cdots\right]^2 \tag{1-11}$$

$$s_y^2 \approx s_u^2\left(\frac{\partial y}{\partial u}\right)^2 + s_v^2\left(\frac{\partial y}{\partial v}\right)^2 + \cdots + 2s_{uv}^2\left(\frac{\partial y}{\partial u}\right)\left(\frac{\partial y}{\partial v}\right) + \cdots \tag{1-12}$$

where s_y^2, s_u^2, and s_v^2 are the variances of y, u, and v. s_{uv}^2 is the covariance of u and v, which is defined as $s_{uv}^2 = r_{uv}s_u s_v$. r_{uv} is the correlation coefficient of the relationship between u and v. The covariance of u and v is positive if they tend to vary together. The covariance is negative if they vary in opposite directions, and it is zero if they are uncorrelated with one another. In general, first two terms in equation (1-12) dominate the uncertainties. If u and v are uncorrelated, the third term vanishes and the formula becomes the so-called *Gaussian error propagation (ISO/GUM 1995) method.*

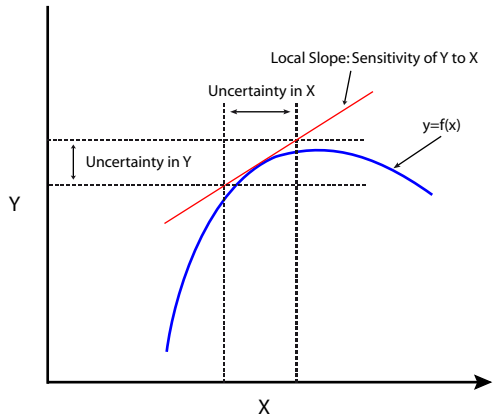

Figure 1-12. Uncertainty estimation of dependent variable y from measured variable x.

Monte Carlo Propagation

The conventional uncertainty analysis methods, which are basically analytical methods (ISO/GUM 1995), become sometimes extremely difficult as the separate effect of each input quantity on the final result (partial derivative) is needed to be determined. It becomes even more unreliable when multiple measured input variables in a complex measurement system are correlated (perfectly or partially). For such complex calculations, variance propagation techniques are complicated to apply analytically, and in some cases their use may not be practical or possible. To overcome problems encountered with analytical methods, numerical techniques are useful in performing an uncertainty analysis. With the availability of computers, numerical experiments have become an increasingly popular method for analyzing physical engineering systems. One of the most commonly applied numerical technique is Monte Carlo simulation. The Monte Carlo method of error propagation consists of repeated calculation of a quantity, each time varying the input data randomly within their stated limits of precision. The statistical distribution of the calculated quantity then shows the effects of the imprecision of the data (Figure 1-13). The Monte Carlo method is just one of many methods for analyzing uncertainty propagation, where the goal is to determine how random variation, lack of knowledge, or error affects the sensitivity, performance, or reliability of the system that is being modeled.

The term Monte Carlo method was presented by Ulam and Metropolis (Metropolis and Ulam 1949) in reference to games of chance, a popular attraction in Monte Carlo, Monaco. Monte Carlo methods are useful for obtaining numerical solutions for problems, which are usually too complicated to solve analytically. Monte Carlo simulation is a method for iteratively evaluating a model using sets of random numbers as inputs. A simulation can typically involve over thousands of evaluations of the model, a task which in the past was only practical using super computers. Simulation of model allows examining system behavior under different scenarios in virtual computational world (Hoffman 1998). Monte

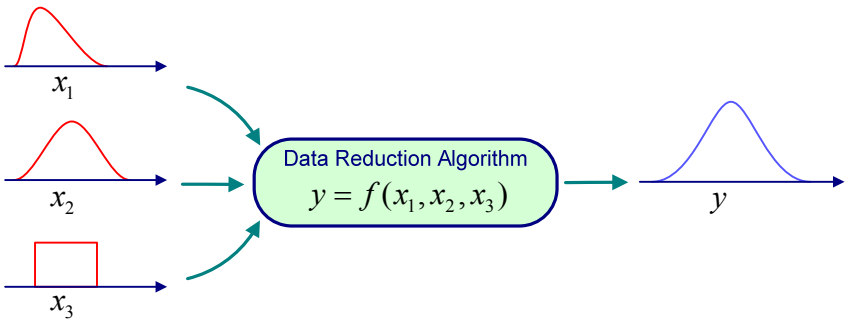

Figure 1-13. Monte Carlo uncertainty propagation.

Carlo simulation is categorized as a sampling method because the inputs are randomly generated from probability distributions to simulate the process of sampling from an actual population. So, we try to choose a distribution for the inputs that most closely matches data we already have, or best represents our current state of knowledge. A successful Monte Carlo calculation requires a reliable set of random numbers. By using random inputs, we are essentially turning the deterministic model into a stochastic model. It is generally preferable to use pseudorandom numbers, numbers generated by a computer algorithm designed to produce a sequence of apparently uncorrelated numbers that are uniformly distributed over a predefined range.

The Monte Carlo propagation method has the advantage of including all sources of uncertainty and is not restricted to a specific set of distributions. Complexity is not a limiting factor in Monte Carlo method as in so many other methodologies. The method permits direct computation of uncertainty even when the function f contains discontinuities or extreme nonlinearities. However, as the methodology is computational intensive, it becomes infeasible with models which have a long run time or too many sources of uncertainty.

1.6. Scope of Work

The microwave backscatter data measured by scatterometers have been shown to be valuable for monitoring surface soil moisture using so-called TU-Wien change detection method (Wagner et al. 1999b). The launch of Metop-A (Meteorological Operation satellite), the first of a new series of three satellites carrying ASCAT (Advanced SCATteromer) for the next 15 years, ensures continuity of soil moisture retrieval from scatterometers' data for more than 30 years considering available ERS-1&2 scatterometer observation datasets.

This study was motivated by the need of revisiting the soil moisture retrieval method due to some shortcomings found in earlier algorithm and to provide consistence integration of ASCAT measurements into retrieval procedure. There was also necessity of developing an error model to quantify uncertainties related to measurements and retrieval algorithm.

The thesis is structured as follows: Chapter 2 gives a short summary about the scatterometers's specifications and relative missions. In chapter 3 a brief review of the TU-Wien soil moisture retrieval concept is presented. The new retrieval algorithm based on the TU-Wien method with new parameterization is introduced in chapter 4. Uncertainty analysis and error propagation is the subject of chapter 5 and 6. Finally in chapter 7 to evaluate the impact of the retrieval modifications on soil moisture estimates, the results are compared with in-situ soil moisture observations as well as global modeled datasets.

2. Scatterometers

Scatterometers are microwave radar sensors used to measure the normalized radar cross section σ^0 of the surface while scanning the surface of the earth from an aircraft or a satellite. They provide day and night time measurement capability which is unaffected by cloud cover. The primary application of the spaceborne scatterometry has been the measurement of near-surface winds over the ocean. The wind measuring principle relies on the fact that winds over the sea cause small-scale disturbances of the sea surface, which modify its radar backscattering characteristics in a particular way. These backscattering properties are well known and are dependent on both the wind speed over the sea and the direction of the wind with respect to the point from which the sea surface is observed. By combining σ^0 measurements from different azimuth angles, the near-surface wind vector over the ocean's surface can be determined using a geophysical model function (GMF) which relates wind and backscatter. Beside its intended application, the measurement of near-surface wind over the ocean, scatterometer data are also used to study polar ice, vegetation, and soil surface properties. There is increasing evidence that the scatterometers also facilitates the measurement of soil moisture. From a physical point of view, scatterometers offer a relatively direct opportunity to measure soil moisture due to the high sensitivity of microwaves to the water content in the soil surface layer. This is specifically the case in the low frequency domain (1-10 GHz).

2.1. European Remote Sensing Satellites (ERS)

ERS-1, launched in July 1991, was the first Earth observation satellite developed by the European Space Agency (ESA) with the overall objectives to provide environmental monitoring in particular in the microwave spectrum. The ERS program, initiated in 1981, had a pioneering character in the field of instrument development (especially active sensors). ERS data have been used in a broad range of disciplines and topics: Observation of oceans, polar ice, land ecology, geology, forestry, wave phenomena, bathymetry, atmospheric physics, meteorology, etc. ERS-1 has been placed in a near-polar orbit at a

mean altitude of about 780 km with an instrument payload comprising active and passive microwave sensors and a thermal infra-red radiometer. Unlike optical instruments, radar systems function quite independently of light conditions and cloud cover which means they can operate around the clock.

ERS-2 is the follow-up ESA mission of ERS-1, launched in April 1995 from Kourou on an Ariane-4 vehicle. The ERS-2 satellite is essentially a copy of ERS-1, except that it includes a number of enhancements; it is also carrying a new payload instrument to measure the chemical composition of the atmosphere, named GOME (Global Ozone Monitoring Experiment). ERS-2 continued data acquiring until January 2001 while all ERS-2 instruments were temporarily switched off due to a failure of a gyroscope. In June 2003, ERS-2 lost its onboard data storage facility, effectively ending its global coverage capability. This implied that only real-time observations could be supported starting by the end of June 2003. From this point on, the spacecraft returns data when in line of sight of an appropriately equipped ground station, which is limited to selected regions (i.e. North America, Europe, Northwest Africa, China and Australia). The ERS-2 spacecraft reached 12 years in orbit on April 2007. All platform subsystems and payload instruments are working nominally and are providing good data. The ERS-2 mission was recently approved to continue for three more years until 2011.

ERS-1 and ERS-2 flew in tandem operations starting September 1995. The tandem mission was completed after nine months of successful operation in May/June 1996. In the orbital tandem configuration, both spacecraft has the same orbit. ERS-2 follows ERS-1 with an approximate delay (referred to as orbit phasing) of 35 minutes. The configuration was

Table 2-1. ERS satellites parameters.

	ERS-1	ERS-2
Launch	17 July 1991	21 April 1995
Launch mass	2354 kg	2516 kg
launcher	Ariane 4	
Spacecraft altitude	770 to 785 km	
Inclination	98.52°	
Orbit	Near-circular, polar, Sun-synchronous	
Local Solar Time	10:30 am at the descending node	
Orbits per day	14.3	
Orbit period	About 100 minutes	
Repeat cycle	3-day, 35-day and 176-day	

that of two-pass measurements of a single-antenna SAR platform (the same SAR instrument on both satellites observing the same area on the ground), permitting the superposition technique of imagery (in data processing) of fairly close repeat tracks.

2.1.1. AMI-SCAT Instrument Description

AMI is an Active Microwave Instrument on board ERS-1 & ERS-2 satellites operating in C-band (5.6 GHz) at VV polarization. Two separate radars, Synthetic Aperture Radar (SAR) and Wind Scatterometer (SCAT), are incorporated within the AMI instrument in three different modes of operation (SAR for Image and Wave mode operation, and scatterometer for Wind mode operation). The Wind and Wave modes are capable of

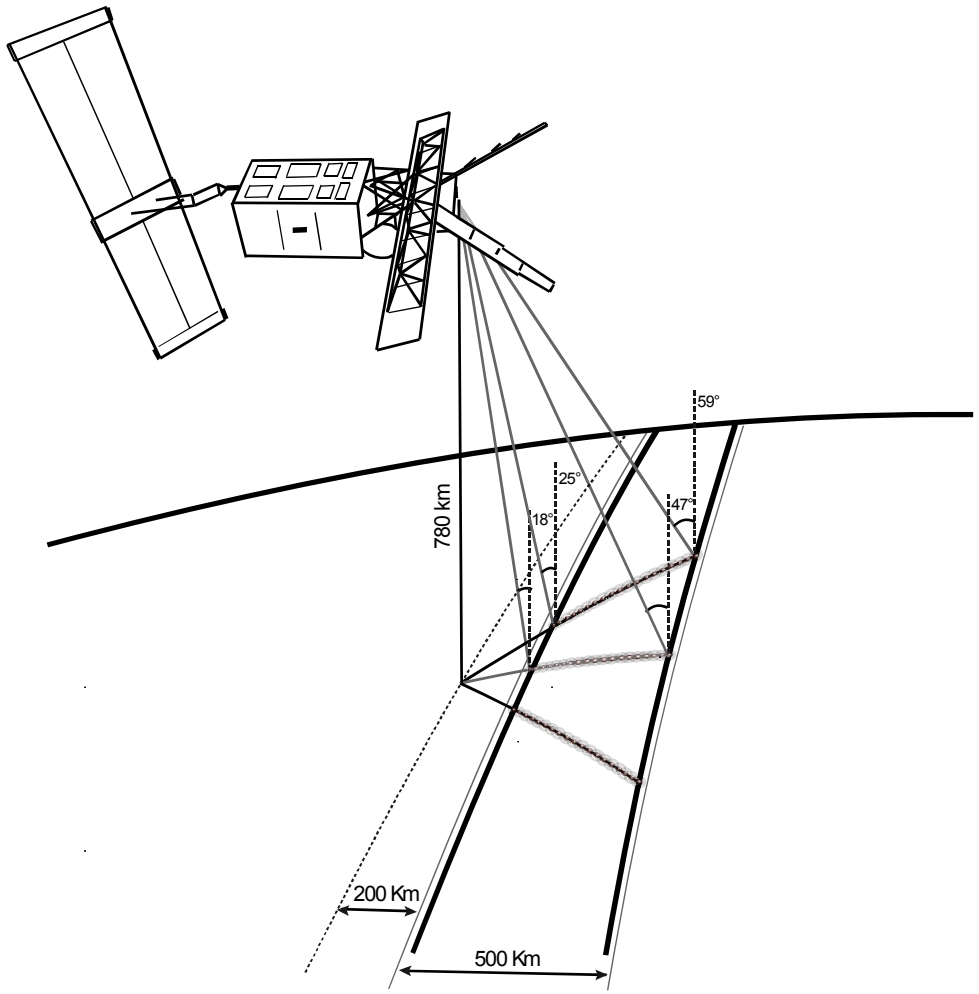

Figure 2-1. AMI-SCAT onboard ERS.

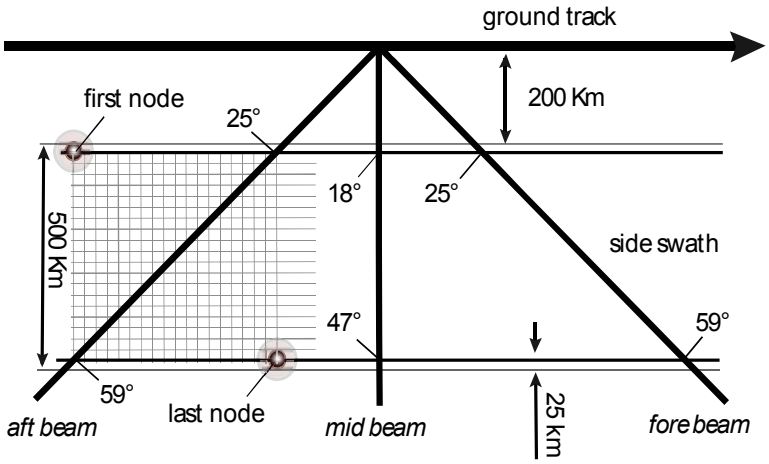

Figure 2-2. AMI-SCAT viewing geometry.

interleaved operation, i.e so-called Wind/Wave mode, but the operation in Image mode excludes the operation of the other two modes. The AMI-SCAT has three antennas generating radar beams looking 45° forward, 90° sideways, and 135° backwards with respect to the satellite's flight direction at different incidence angles ranging from 18° to 59°. The three antenna beams continuously illuminate a swath of 500 km each measuring the radar backscatter from the surface for overlapping 50 km resolution cells using 25 km grid spacing. The result is three independent backscatter measurements so-called *"triplets"* at different viewing angles relating to the cell center nodes (Attema 1991)(Figure 2-2)

Table 2-2. AMI-SCAT instrument specifications.

Frequency	5.3 GHz. (C-Band)		
Polarization	VV		
Swath Width	500 km		
Swath Stand-off	200 km to the right of sub-satellite track		
Localization Accuracy	5 km		
Spatial Resolution	≥ 45 km (along and cross track)		
Sampling Interval / Orbit Grid Spacing	25 km		
	fore	***mid***	***aft***
Antenna length	3.6 m	2.3 m	3.6 m
Azimuthal Angle	45°	90°	135°
Incidence Angle Range	25°-59°	18-47°	25°-59°
Radiometric Resolution (*kp*)	≤ 7.0%	≤ 6.5%	≤ 7.0%

Table 2-3. METOP-A specifications.

Launch	19 October 2006
Launch mass	4093 kg
launcher	Soyuz/ST
Life Time	5 years
Spacecraft altitude	800 to 850 km
Inclination	98.7°
Orbit	Near-circular, Polar, Sun-synchronous
Local Solar Time	9:30 am at the descending node
Orbit period	About 101 minutes
Repeat cycle	29 days (412 orbits)

2.2. EPS Program

EPS (EUMETSAT Polar System) is the European component of a joint European/US polar satellite system, the Initial Joint Polar System (IJPS) to support operational meteorology and climate monitoring. The objective of the IJPS is to share the operations between NOAA and EUMETSAT and to ensure the continuity and timely availability of meteorological data through a series of polar orbiting satellites with a mid-morning equator crossing time of 09:30 h (Europe) and an afternoon equator crossing time of 14:00 h (USA) (Klaes and Holmlund 2007).

2.2.1. Meteorological Operational Satellites (METOP)

The EUMETSAT Polar System is made up of a space and a ground segment. The space component is composed of the METOP series of spacecraft jointly developed by ESA and EUMETSAT. The ground component is has a central part and decentralized facilities, in particular the Satellite Application Facilities (SAF), which perform higher level product generation for specific meteorological application areas. Three METOP satellites are foreseen to be launched sequentially with a lifetime of 5 years each in order to provide data at least 14 years of operational service for meteorology and climate monitoring.

METOP-A, launched on 19 October 2006, is the first satellite in the series foreseen in EPS program carrying a new generation of European instruments that offer improved remote sensing capabilities to both meteorologists and climatologists with a set of 'heritage' instruments provided by the United States.

2.2.2. ASCAT Instrument Description

The Advanced Scatterometer (ASCAT) is one of the new-generation instruments carried on METOP. ASCAT is a real aperture, vertically polarized C-band radar with high radiometric stability. It transmits long pulses with linear Frequency Modulation (chirp) at a carrier frequency of 5.255 GHz. The received echoes are dechirped and Fourier-transformed on board, resulting in a signal where the frequency components map to slant range. The averages raw echoes together with averaged noise measurements are sent to the ground in source packets. ASCAT builds the operational continuation of the ERS scatterometer mission. Like the SCAT, the ASCAT system uses a fan-beam antenna technology. Contrary to SCAT it uses two sets of three antennas instead of one. For ASCAT also the incidence angle range has been extended from 25° to 65°. Hence ASCAT covers two 550 km swaths to the left and right of the satellite ground track which are separated from the satellite ground track by about 336 km. This results in over twice faster global-coverage capability than its predecessors SCAT.

Beside an optimized viewing geometry, ASCAT also features a number of technical improvements. The improved instrument design and radiometric performance results in higher stability and reliability of ASCAT measurements. Additionally EUMETSAT foresees to generate a research product at a resolution of 25 km (Figa-Saldana et al. 2002). The major improvements of ASCAT with respect to SCAT are:

Table 2-4. ASCAT instrument specifications.

Frequency	5.255 GHz. (C-Band)		
Polarization	VV		
Swath Width	500 km (on both sides - double swath)		
Swath Stand-off	336 km to the right/left of the sub-satellite track		
Localization Accuracy	4.4 km		
	Nominal Mode	***High-Resolution Mode***	
Spatial Resolution	50 km	25 - 34 km	
Sampling Interval / Orbit Grid Spacing	25 km	12.5 km	
Radiometric Resolution (*kp*)	2%-5%	4%-11%	
	fore	***mid***	***aft***
Antenna length	3 m	2 m	3 m
Azimuthal Angle	45°	90°	135°
Incidence Angle Range	34°-64°	25-53°	34°-64°

- Enhanced coverage due to double swath operation.
- Higher incidence angle range towards an area.
- Additional generation of a research product at a higher resolution of 25-37 km on a 12.5 km nodal grid.
- Improved instrument design and radiometric performance, resulting in higher stability and reliability.
- Reduced downlink data rate due to on-board data processing (from 1.4 Mbit/s on AMI-SCAT to 55 kbit/s on ASCAT).
- In addition to the processing of echo signals, the instrument also performs an internal calibration process within each pulse repetition interval.
- Reduced power needed for the transmission of continuous-wave pulses (about 120 W of peak power are needed for ASCAT compared to 4.8 kW for SCAT).
- Continuous data acquisition and product generation without sharing operation time in orbit with other instruments, which would increase the data coverage.

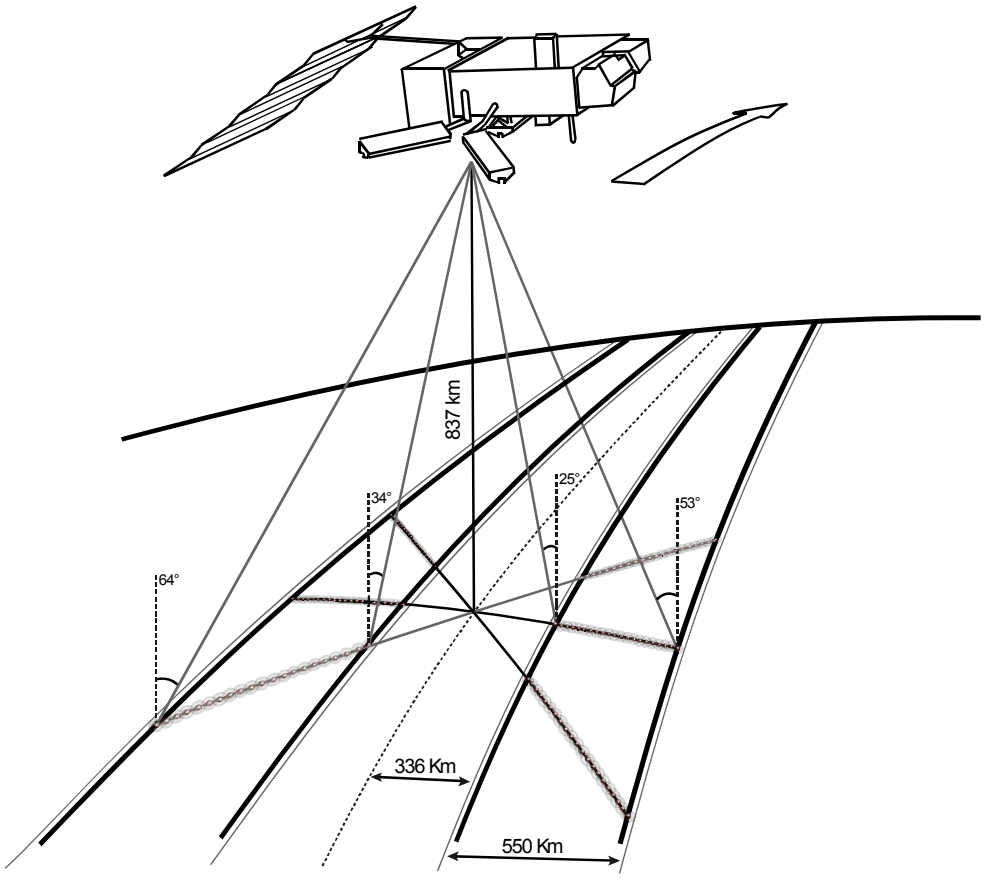

Figure 2-3. ASCAT onboard METOP.

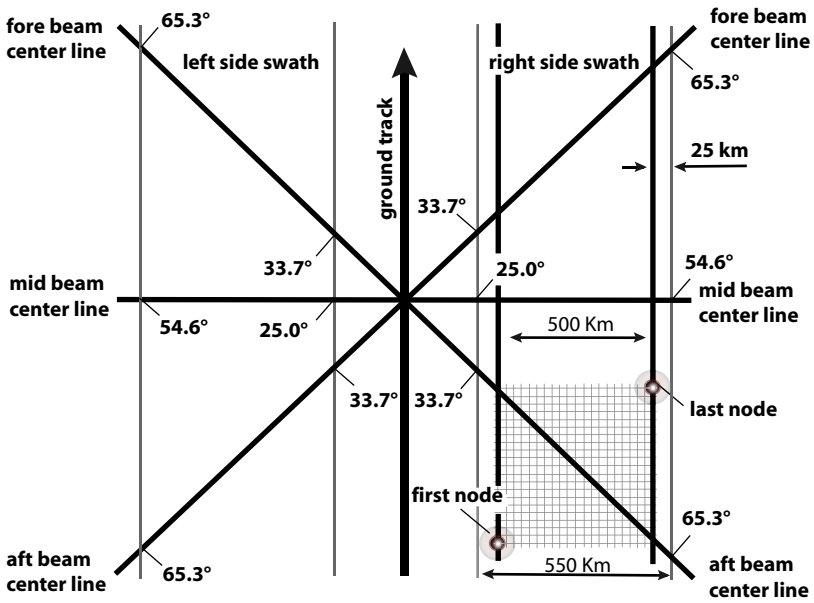

Figure 2-4. ASCAT Viewing geometry.

3. TU-Wien Soil Moisture Retrieval Method

Scatterometers measure the intensity of backscattering signal, which is affected by roughness, vegetation structure, vegetation water content, and soil moisture. These factors influence the backscattering coefficient σ^0 on different time scales. At the resolution of the ERS and Metop scatterometers, surface roughness can be in general considered as a temporally invariant parameter. Surface soil moisture changes rapidly within hours to days, contrary to the vegetation canopy and vegetation water content, which vary within several days to weeks. Scattering from vegetated surface is a complex phenomenon. There have been several canopy scattering models developed to describe σ^0 in terms of vegetation and soil surface parameters based on a solution of the radiative transfer equation (Ulaby et al. 1990); (Karam et al. 1992); (Saatchi et al. 1994). Radiative transfer theory describes the propagation of radiation through a medium affected by absorption, emission and scattering processes. Equation 3-1 formulates the first-order radiative transfer solution for the scattering problem of the vertically polarized radiation by a vegetation canopy (Fung 1994):

$$\sigma_{can}^0 = \sigma_{vol}^0 + \sigma_{sur}^0 + \sigma_{\text{int}}^0 = \frac{\omega\cos\theta}{2}(1 - e^{-\frac{2T}{\cos\theta}}) + \sigma_s^0(\theta)e^{-\frac{2T}{\cos\theta}} + 2\Gamma_v(\theta)\omega T e^{-\frac{2T}{\cos\theta}}, \qquad (3\text{-}1)$$

where σ_{can}^0 is Backscattering coefficient of the vegetation canopy, σ_{vol}^0 volume scattering, σ_{sur}^0 surface scattering, σ_{int}^0 surface-volume interaction, σ_s^0 back scattering coefficient of soil surface, ω single-scattering albedo of the canopy, T optical depth or thickness of the canopy, and Γ_v Fresnel power reflectivity for vertically polarized radiation.

The problem with more complex theoretical scattering models is that their input data requirements are very challenging and for solving the equations many parameters are needed such as leaf diameter, branch length, trunk moisture, and probability functions representing the orientational distribution of leaves, branches, and trunks.

The TU-Wien soil moisture retrieval method initially presented by Wagner *et al.* (1999b) is principally an empirical model based on change detection. Several studies showed that the change detection technique can overcome some of the problems of physically based inversion models as it directly accounts for the scattering process of rough and heterogeneous land surfaces if sufficient long-term data are available. The potential of using such methods has been demonstrated for both active and passive microwave data (Moeremans and Dautrebande 1998), (Quesney et al. 2000), (Moran et al. 2000), (Le Hegarat-Mascle et al. 2002), (De Ridder 2000), (Njoku et al. 2002). Wagner (1998b) used a backscattering model for sensitivity analysis of ERS scatterometer data in which backscatter from vegetated land surface is described as a mixture of nontransparent (forests, bushes, shrubs) and translucent (grassland, agriculture land) vegetation:

$$\sigma^0 = (1 - A_{nt}) \cdot \sigma^0_{tr} + A_{nt} \cdot \sigma^0_{nt}, \tag{3-2}$$

where σ^0_{tr} is the backscatter from translucent vegetation, σ^0_{nt} is the backscatter from nontransparent vegetation, and A_{nt} is the percentage area of nontransparent vegetation.

The σ^0 of natural targets depends strongly on the incidence angle. The growth of translucent vegetation types such as grasses or agricultural crops results in a less steep decline of σ^0 with the incidence angle, and σ^0 may increase or decrees depending on the incidence angle and soil wetness. In general with increasing the percentage area of nontransparent vegetation A_{nt}, the backscattering coefficient in very low incidence angles may decrease whereas in higher incidence angles the backscatter intensity measured by scatterometer increases. In the TU-Wien method soil moisture dynamics are extracted after modeling the behavior of σ^0 with respect to the surface roughness and the local variability of vegetation and eventually subtracting them from the backscatter signal. In the retrieval algorithm the multi-looking direction ability of scatterometer is used to describe the incidence angle behavior of the backscatter signal as a seasonal function. Table 3-1 summarizes the mathematical formulations involved in TU-Wien algorithm.

3.1. Normalization of Viewing Geometry

Both SCAT and ASCAT instruments onboard ERS-1&2 and Metop take the σ^0 measurements at different azimuthal and incidence angles, which vary from acquisition to acquisition. As the intensity of backscatter signal strongly depends on the incidence angle, it is not possible to compare σ^0 observations directly. Therefore the backscattering coefficients have to be normalized to a reference incidence angle. Since in most areas of the

Table 3-1. Mathematical formulations of the TU-Wien soil moisture retrieval model.

Incidence angle dependency of backscatter:

$$\sigma^0(\theta,t) = \sigma^0(40,t) + \sigma'(40,t)(\theta - 40) + \frac{1}{2}\sigma''(40,t)(\theta - 40)^2 \quad (3\text{-}3)$$

σ', and σ'' are defined as the first and second derivatives of $\sigma(\theta)$.

Seasonal variation of the slope:

$$\sigma'(40,t) = C' + D'\psi'(t) \quad (3\text{-}4)$$

C' is the annual minimum slope value and D' is the dynamic range of slope.
$\psi'(t)$ is an empirical periodic function describing the annual variation of slope.

Seasonal variation of the curvature:

$$\sigma''(40,t) = C'' + D''\psi''(t) \quad (3\text{-}5)$$

C'' is the annual minimum curvature value and D'' is the dynamic range of curvature.
$\psi''(t)$ is an empirical periodic function describing the annual variation of curvature.

Normalized backscatter coefficient:

$$\sigma_i^0(40,t) = \sigma_i^0(\theta_i,t) - \sigma'(40,t)(\theta_i - 40) - \frac{1}{2}\sigma''(40,t)(\theta_i - 40)^2 \quad (3\text{-}6)$$

$\sigma_i^0(40,t)$ is the normalized backscatter of ith beam at 40°.

Backscatter under dry and wet conditions:

$$\sigma_{dry}^0(40,t) = C_{dry}^0 - D'\psi'(t)(\theta_{dry} - 40) - \frac{1}{2}D''\psi''(t)(\theta_{dry} - 40)^2 \quad (3\text{-}7)$$

$$\sigma_{wet}^0(40,t) = C_{wet}^0 - D'\psi'(t)(\theta_{wet} - 40) - \frac{1}{2}D''\psi''(t)(\theta_{wet} - 40)^2 \quad (3\text{-}8)$$

σ_{dry}^0 and σ_{wet}^0 are backscatter from dryest/wettest soil, θ_{dry} and θ_{wet} are the crossover angles for dry/wet soil conditions, C_{dry}^0 and C_{wet}^0 are the annual minimum and maximum backscatter.

Surface Soil moisture:

$$\Theta_s(t) = \frac{\sigma^0(40,t) - \sigma_{dry}^0(40,t)}{\sigma_{wet}^0(40,t) - \sigma_{dry}^0(40,t)} \times 100 \quad (3\text{-}9)$$

Θ_s is defined as the degree of saturation ranging between 0 and 100%

Earth the azimuthal look direction does not have a significant effect on backscattering observations, the azimuthal angle was not considered in normalization of viewing geometry in the TU-Wien method.

3.1.1. Incidence Angle Dependency of Backscatter

The backscattered energy received by the scatterometer sensor increases with decreasing incidence angle. As it mentioned above the rate of backscatter change due to incidence angle variation, depends on the surface roughness. Bare soil roughness is basically constant in time but vegetation can have a seasonal influence on the incidence angle dependency behavior of backscatter. With increasing the vegetation density, the shape of incidence angle dependency of backscatter will change depending on the type and density of vegetation as well as the orientation of vegetation elements. In figure 3-1 two different scenarios of backscattering are illustrated. The first diagram (figure 3-1-a) indicates altering the backscatter because of soil moisture change and the other plot (figure 3-1-b) shows backscatter change due to vegetation growth. A second degree polynomial is usually sufficient to describe backscatter dependency on incidence angle. The shape of the polynomial fitted to the backscatter measurements indicates the dominating scattering mechanism. As an example, figure 3-2 shows monthly polynomials fitted to the measurements in two different regions. In the first region the fitting curves indicate predominantly volume scattering having more or less the same shape in different months of year (figure 3-2-a). However, in the other region (figure 3-2-b) the shape of monthly polynomial fits changes with changing the time of year indicating strong surface scattering. In the TU-Wien method a simple model (equation 3-3 in table 3-1) is used to describe σ^0 - θ relationship. In this approach it is assumed that soil moisture variations do not or

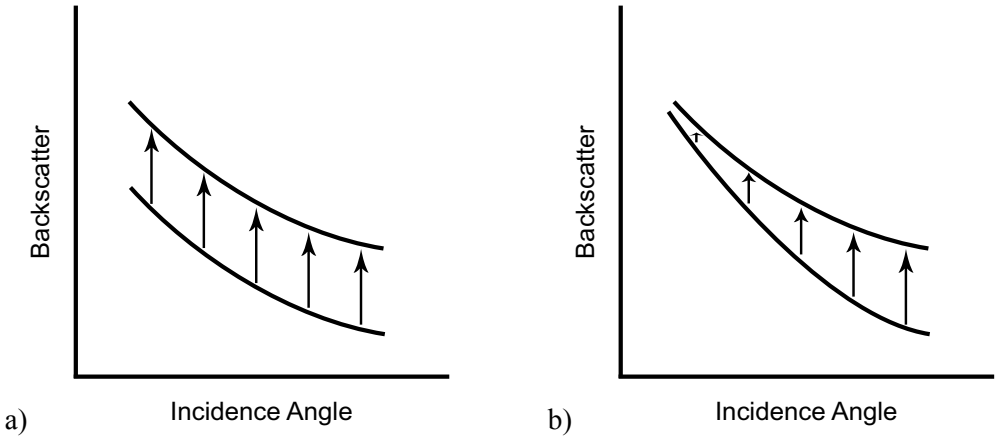

Figure 3-1. Incidence angle dependency of backscatter while a) soil moisture, b) vegetation change.

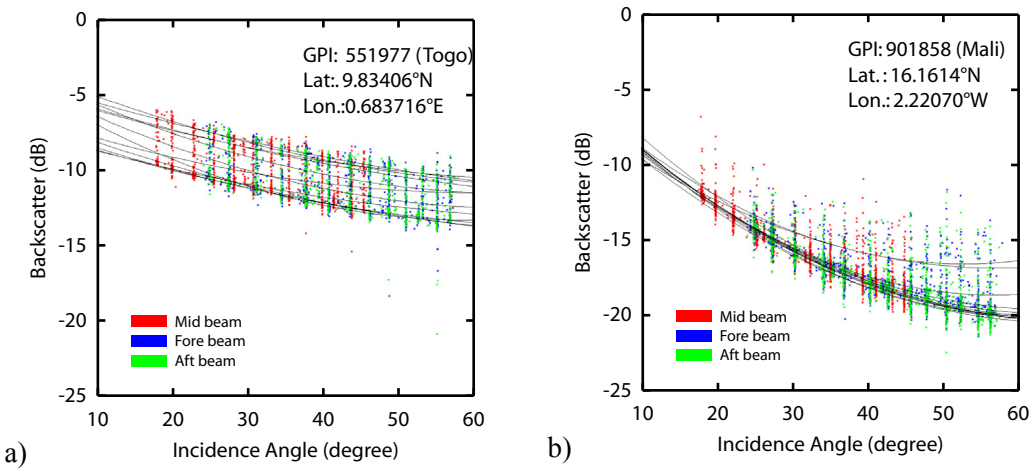

Figure 3-2. Examples of incidence angle dependency in two different regions.

only minimally affect the incidence angle dependency. Therefore to remove the impact of soil moisture variations on calculations, instead of modeling σ^0 a first degree polynomial is fitted to the σ' values which is described as:

$$\sigma'(\theta) = \frac{d\sigma^0(\theta)}{d\theta} \tag{3-10}$$

The slope $\sigma'(\theta)$ is in general a negative number as σ^0 decreases with increasing incidence angle θ. A first order approximation of the $\sigma'(\theta)$ according to the Taylor series expansion around a reference incidence angle, which is here chosen as 40°, is expressed as:

$$\sigma'(\theta) = \sigma'(40) + \sigma''(40)(\theta - 40) \tag{3-11}$$

where σ' and σ'' are the first and second derivatives of σ^0, called slope and curvature respectively. The σ' and σ'' are sensitive to the vegetation and surface structure, whereas it is assumed to be independent of the dielectric properties. It has to be mentioned that each $\sigma'(40)$ triplet only allows calculating an approximation, which is only valid near the respective incidence angle and which is disturbed by measurement noise.

The exact shape of the polynomial expressed in equation 3-3 depends on the land surface properties, i.e. it is sensitive to the vegetation and surface structure. Smooth surfaces with no vegetation result in a steep decline of σ^0 with respect to θ and therefore low, negative σ'

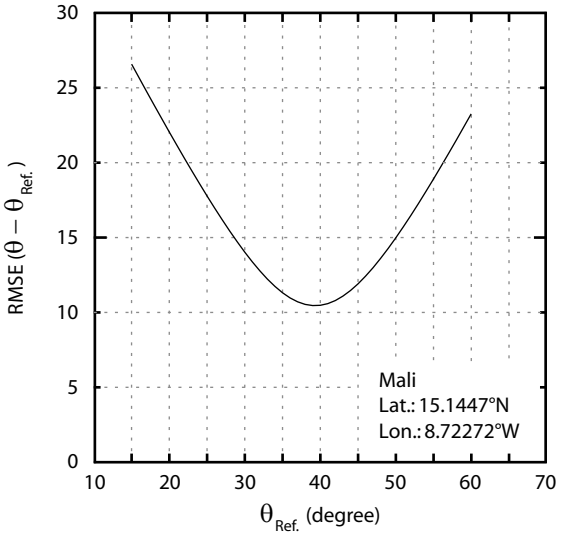

Figure 3-3. Choosing 40° incidence angle as reference angle.

values. Vegetation and rough surfaces generally result in higher σ' values. This is important to note, as the normalization of σ^0 has to take vegetation growth/decay effects into account. Therefore the parameters are estimated for each month of year. This also ensures that the parameters are calculated for a large number of $\sigma^0(\theta)$ measurements, which are evenly distributed over the entire incidence angle range. As a result, twelve values of $\sigma'(40)$ and $\sigma''(40)$ for each month of year are obtained. The slope and curvature periodic functions $\sigma'(40,t)$, $\sigma''(40,t)$ are consequently calculated from monthly values by using empirical trigonometric functions according to equation 3-4 and equation 3-5. Using prescribed empirical functions instead of a simple interpolation, has the advantage of a controlled interpolation leading to robust estimates.

3.1.2. Normalized Backscattering Coefficients

Using the incidence angle dependency function, the backscatter coefficients can be extrapolated to the reference incidence angle according to equation 3-6 with respect to the time of year. The index *i* in equation 3-6 stands for one of the three beams. Averaging over three beams has the effect that the uncertainty due to instrument noise, speckle, and azimuthal effects is lowered by a factor of $\sqrt{3}$. In TU-Wien algorithm the reference incidence angle is selected as 40° to minimize extrapolation errors (Wagner et al. 1999c) considering the incidence angle range of ERS scatterometer (18°-59°). Figure 3-3 indicates the Root Mean Square Error (RMSE) between the actual incidence angle measurements and different presumed reference incidence angles (calculated for a grid point located in Mali). As the RMSE has the lowest value at 40°, this incidence angle is chosen as reference in extrapolating backscatter measurements.

3.2. Surface Soil Moisture Retrieval

The TU-Wien method is based on a change detection model that compares the normalized backscatter to the lowest and highest values that have been ever measured within the long-term $\sigma^0(40)$ time series. According to equation 3-2, the $\sigma^0(40)$ measurement is composed of two fractions: 1) backscatter from bare soil; 2) backscatter from heterogeneous vegetation canopy. Surface soil moisture corresponds to the scaled $\sigma^0(40)$ after subtracting the backscatter of the vegetated land surface under dry soil condition from the actual backscatter measurement

3.2.1. Vegetation Correction

Temporal variations of σ^0 are due to volume scattering effects in the vegetation canopy and surface scattering from the underlying soil surface (Fung 1994). In simple radiative transfer models like the Cloud Model (Attema and Ulaby 1978), the effect of vegetation is largely controlled by the optical depth which weights the relative contribution of surface and volume scattering. Although the TU-Wien model uses a different parameterization, it is similar in functionality to these models. When vegetation grows, the optical depth increases, and the volume scattering term becomes more important. This does not necessarily mean that backscatter increases. In situations where the reduced contribution from the underlying ground is more important than the enhanced volume scattering, σ^0 decreases. For low incidence angles, the effect of vegetation is mainly attenuation of the signal returned by underlying soil (Taconet et al. 1994). In other words backscattering from bare soil is in general stronger than vegetated soil in near range. Because of rapid drop-off of the bare soil

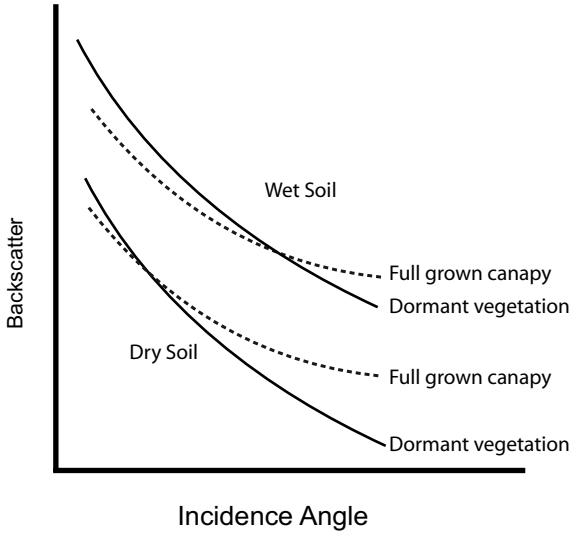

Figure 3-4. Illustration of the crossover angle concept.

backscattering the situation may be reversed at high incidence angles. Therefore at some incidence angle $\sigma^0(\theta)$ curves of a developing and a full grown vegetation canopy should cross over (Wagner et al. 1999a). In the TU-Wien model it is assumed that the effect of vegetation is minimal at the so called "crossover" angles θ_{dry} and θ_{wet}, which differ for dry and wet soil conditions. If such crossover angle exists then for dry conditions it should be found at lower incidence angles than for wet conditions (figure 3-4). By considering crossover angle concept and using equations 3-4 and 3-5 into 3-3 after separating the time-dependent and constant terms, the lowest and highest levels of the backscatter σ^0_{dry}, σ^0_{wet} at 40° are given by equation 3-7 and 3-8. Equations 3-7 and 3-8 imply that the dry and wet references vary during the year depending on the incidence angle deviation from θ_{dry} and θ_{wet} and also the condition of vegetation canopy, which is reflected in the slope and curvature parameters. Since soil moisture and vegetation both induce an increase on backscatter intensity, the $\sigma^0_{wet}(40,t)$ is more or less independent of vegetation status but $\sigma^0_{dry}(40,t)$ increases from winter to summer due to vegetation growth. This automates a vegetation correction in soil moisture estimation if the crossover angles are chosen correctly.

3.2.2. Wet Reference Correction

σ^0_{dry} and σ^0_{wet} are calculated from the lowest and highest $\sigma^0(40)$ extremes acquired from the long-term scatterometer measurements. Hence the reference values will likely represent the respective driest and wettest soil conditions. But in some extreme dry climates such as deserts, where soil saturation is probably never observed, an empirical bias-correction factor is needed to be applied to σ^0_{wet} in order to obtain spatially consistent soil moisture estimates. Such areas can be identified by using external climate data.

3.2.3. Relative Surface Soil Moisture

Assuming a linear relationship between $\sigma^0(40)$ and the surface soil moisture content (Ulaby et al. 1982), the normalized soil water content Θ_s in the surface layer is estimated by equation 3-9. Θ_s is a relative value representing surface soil moisture at topmost few centimeters of soil that are accessible to C-band microwaves (0.5 - 2 cm) and ranging between 0% and 100%.. If σ^0_{dry} and σ^0_{wet} represent completely dry and saturated soil surface then Θ_s is equal to the degree of saturation which is the soil water content expressed in percent of porosity

4. An improved Soil Moisture Retrieval Algorithm Based on TU-Wien Method

On basis of the TU-Wien change detection method a processing algorithm, WARP (WAter Retrieval Package), has been developed at the Institute of Photogrammetry and remote Sensing (IPF) at Vienna University of Technology (TU-Wien). In WARP, the ERS-1&2 scatterometer long-term observations are used to extract model parameters describing surface backscatter and consequently to retrieve relative soil moisture. The original method as proposed by Wagner *et al.* (1999b) was developed and examined over different regions of the world; Mali, Iberian Peninsula, Ukraine and Canadian prairies. The choice of study areas was mainly due to availability of reference data. Scipal (2002) used the method to derive the first remotely sensed global soil moisture dataset. During recent years the dataset produced with WARP4 has been evaluated in several validation studies (Wagner et al. 2003) (Drusch et al. 2004) (Dirmeyer et al. 2004) (Ceballos et al. 2005) (Pellarin et al. 2006) (Crow and Zhan 2007) (de Jeu et al. 2008) (Albergel et al. 2008) (Ruediger et al. 2008). The data was also used successfully in hydrologic (Scipal et al. 2005) (Parajka et al. 2006) (Vischel et al. 2008) and climate studies (Fontaine et al. 2007) and in first assimilation experiments (de Wit and van Diepen 2007) (Scipal et al. 2008).

Although Wagner *et al.* (2003) found that the transfer of the methods to a global scale lead to satisfactory results, some shortcomings of the algorithm have been recognized. That is, 1) the azimuthal look direction of the sensor is not explicitly incorporated in the retrieval; 2) the backscatter normalization parameters of the model, which correspond to yearly vegetation change, are determined on a monthly basis neglecting higher frequency variations; 3) the estimation of the dry/wet references lead to spatially inconsistent results, especially in the presence of high noise; and 4) lack of a persistent error model. This chapter presents an enhanced retrieval algorithm based on TU-Wien method with new parameterization and modifications. The new algorithm overcomes some limitations identified in the earlier algorithm WARP4 and results in a more uniform performance of the model and consequently spatially more consistent soil moisture estimates with a better resolution. Figure 4-1 shows the processing chain of the WARP5 algorithm.

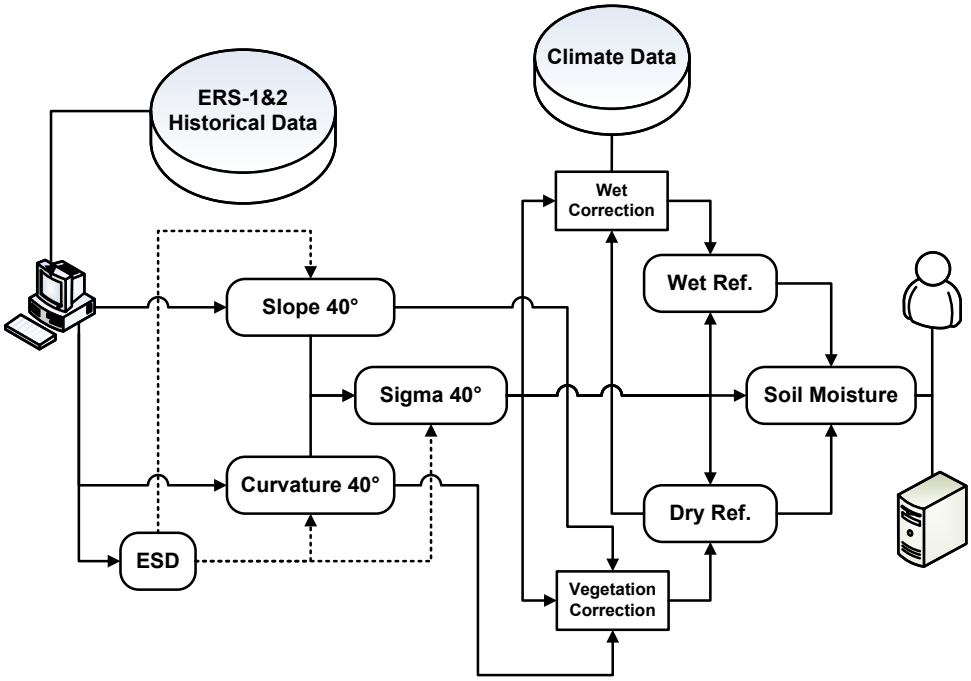

Figure 4-1. WARP5 algorithm processing chain.

4.1. Scatterometer Data Collocation in WARP5

WARP algorithm is principally characterized by a number of parameters derived from long-term time series of backscatter measurements. In order to apply a change detection method for retrieving relative soil moisture, σ^0 measurements are required as time series. Therefore the scatterometer measurements are needed to be re-gridded from orbit geometry into a Discrete Global Grid (DGG). In this way each defined grid point is associated with time series of measurements and holds its own entry in the backscatter database.

4.1.1. Discrete Global Grid (DGG)

The DGG used for data aggregation in WARP4 was an adapted version of a sinusoidal grid and is generated by an adapted partitioning of the globe with about 25 km equal grid spacing (Wagner 1998a). To provide enough measurements for the interpolation procedure in each satellite pass, the radius of the sampling area was set to 36 km, considering the 25 km SCAT orbit grid. This area includes the adjacent grid points of each DGG point also in diagonal direction, located at about 35.4 km at most. The WARP4 grid was based on simplified assumptions to disburden data resampling. These are: 1) a spherical model of the Earth; 2) a geocentric coordinate system; and 3) no full compliance with the requirement for

Table 4-1. WARP5 Discrete Global Grid (DGG) specifications.

Ellipsoid	GEM6	
Type	Partitioned: Adapted Geodetic Grid	
Dimension	**Latitude**	**Longitude**
Extent	89.0S : 89.0N	180.0W : 180.0 E
Grid Spacing	12.5 km	12.5 km
Number of elements	1583	3207

uniform grid spacing. Using a simplified model of the Earth, not compliant with the model used during the data generation process, leads to collocation and coordinate transformation errors. To minimize these errors a new grid is implemented in WARP5. Apart from a new physical definition of the analysis grid, the grid point spacing is reduced by a factor of two. This makes it possible to: 1) include directly the ASCAT fine resolution (25km) product in the analysis; and 2) build up a consistent soil moisture dataset including both SCAT and ASCAT data. The new grid is based upon the GEM6 ellipsoid, which is also used during the ground range projection of SCAT and ASCAT data (Lecomte 1998), and generated by an adapted partitioning of the globe with about 12.5 km equal grid spacing (Kidd 2005). Table 4-1 indicates the WARP5 grid specifications. To facilitate data processing, the globe is structured as 180 cells, where each grid point is connected with a cell number. Furthermore the data processing is limited to areas between 60°S and 80°N latitudes. Coastal zones, inland water bodies, and areas covered with permanent ice are excluded from analysis and only 839826 grid points are practically used (figure 4-2). There are 91 cells from 180 cells containing at least one land grid point.

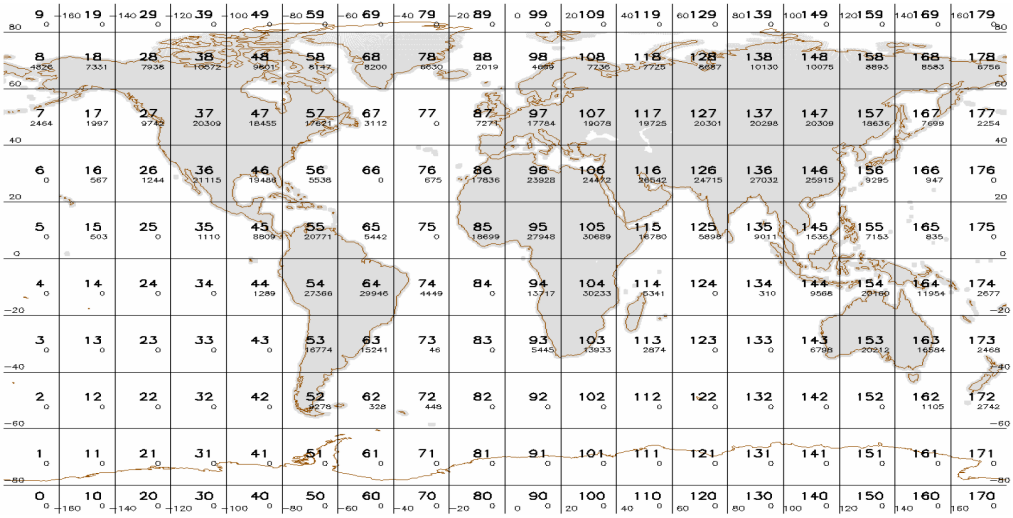

Figure 4-2. Partitioning the grid points into 180 cells. Each cell contains a certain number of grid points holding actual reprocessed data.

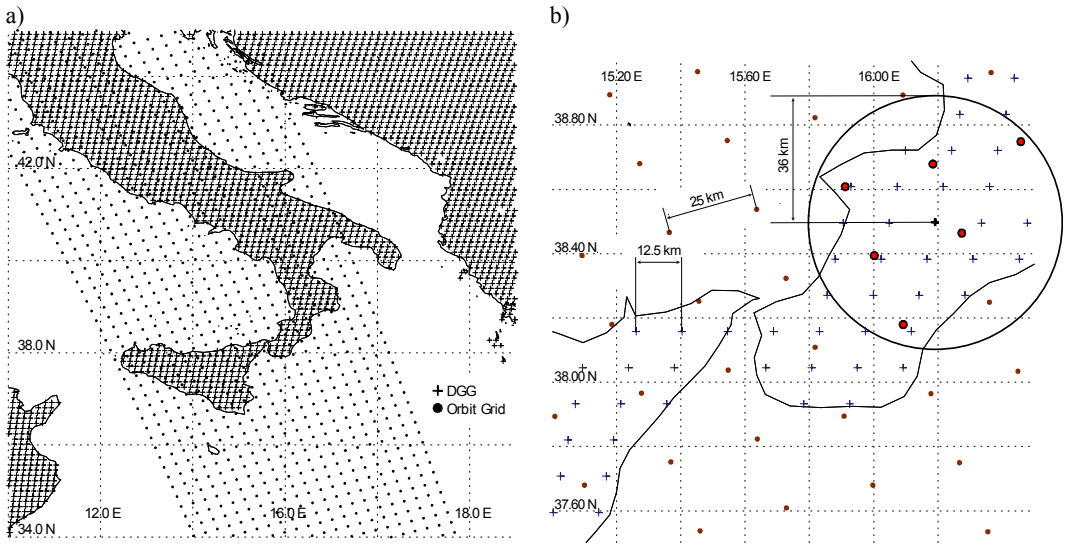

Figure 4-3. a) ERS sctterometer orbit grid and DGG. b) Resampling area around each DGG point.

4.1.2. Oversampling of Measurements to DGG

A 36km search radius around each DGG point is defined in WARP to collocate the incoming σ^0 triplets in orbit geometry and from their corresponding swath node (figure 4-3). This certain search radius is explicitly set to have at least 3 measurements in each satellite pass over the DGG point considering that the orbit grid is a 25km spaced grid.

Interpolating Scatterometer Measurements: Hamming Window Function

The oversampled data are spatially distributed within the search radius area of each DGG point. In signal processing, a common way of resampling such irregularly distributed data is using a window function (or apodization function) that is zero valued outside of a chosen interval. When the data signal is multiplied by the window function, the product is also zero-valued outside the interval. All that is left is the "view" through the window. In WARP algorithm, the Hamming window function is used for this purpose. This is a function frequently used in radar remote sensing, described as:

$$H(x) = 0.54 + 0.46\cos\left(\frac{\pi x}{r}\right), \tag{4-1}$$

where x is the distance to the center of the window and r is the radius of the window.

The Hamming window is a weighting function, which assigns more weight to the points closer to its center value and less to those further away (Blackman and Tukey 1959). In addition to the new grid in WARP5, the way that the observations are handled has also been modified. In WARP4 the Hamming function defined as (4-1) is used once the normalized backscatter is derived. In WARP5 the Hamming function is applied at the very first step of the processing for the backscatter coefficients σ^0 as well as the azimuthal and incidence angles φ, θ separately for each beam according to equation 4-2. This results in a more accurate calculation of the model parameters which leads to a more consistent and spatially uniform estimation of soil moisture.

$$P = \frac{\sum_{i}^{m} P_i H(x_i)}{\sum_{i}^{m} H(x_i)}, \tag{4-2}$$

where P is the interpolated parameter and m is the number of measurements within the searching radius around DGG point.

The position of the scatterometer measurements within the search radius of each DGG point differs basically in each satellite pass. The distance of the nearest measurement to the center of DGG point ranges from 0 to ~26km with the average of 10km (figure 4-4). However, there are few suspected measurements with a distance farther than 26km from the center of the resampling area. Figure 4-5 shows geographical distribution of such cases with

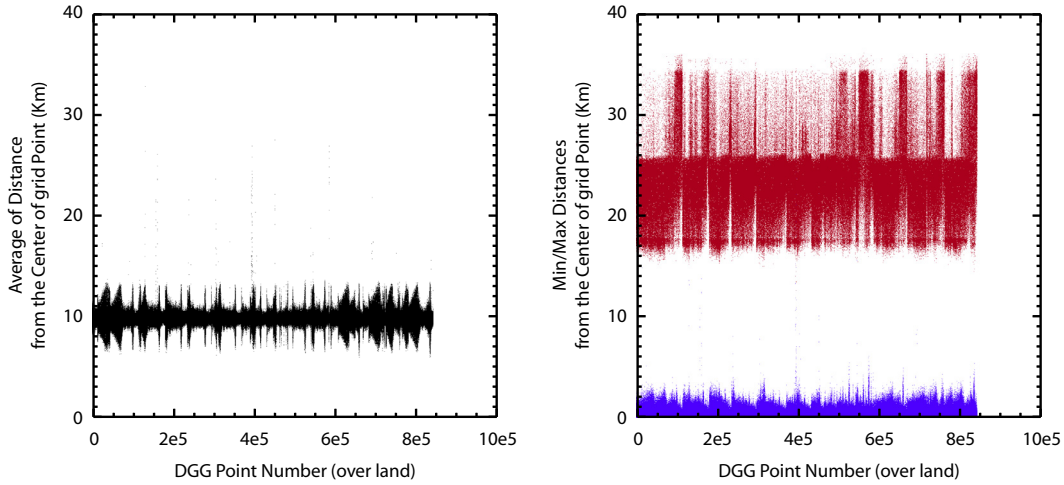

Figure 4-4. Mean, max., and min. distance of resampled measurements from the center in each DGG point.

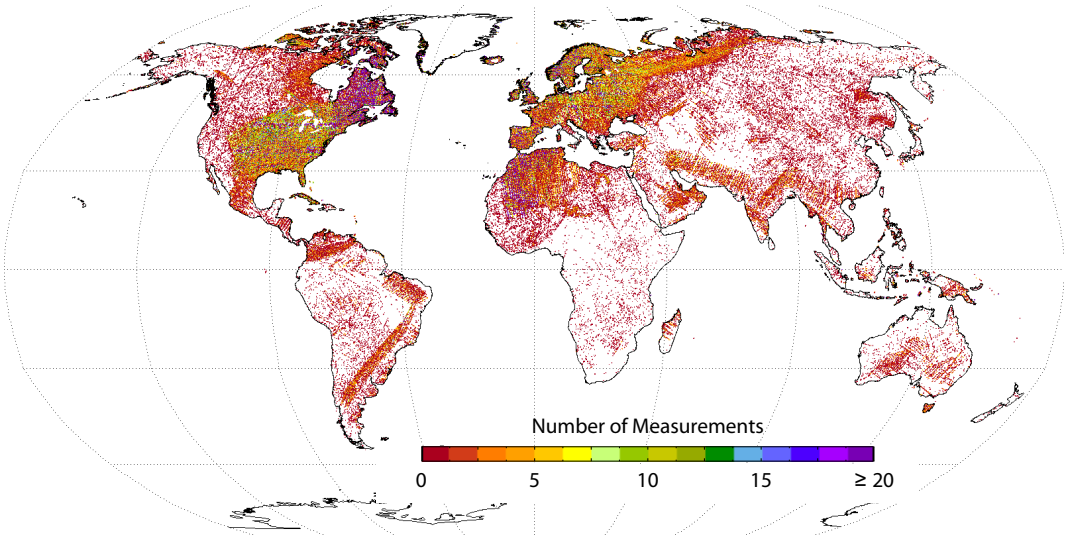

Figure 4-5. Oversampled measurements with more than 26km distance from the respective DGG points.

the number of occurrence. These measurements could be displaced due to some geocoding errors in the preprocessing of the backscatter signals. Therefore such data points are flagged as suspected in WARP5 data processing chain and left out from the model's parameters calculations. The total number of available ERS-1&2 scatterometer measurements aggregated between August 1991 and May 2007 are shown in figure 4-6. The number of ascending and descending measurements are globally different because of exclusive operation of SAR and scatterometer instruments. Figure 4-7 illustrates the distribution of scatterometer measurements in ascending and descending passes according to (4-3).

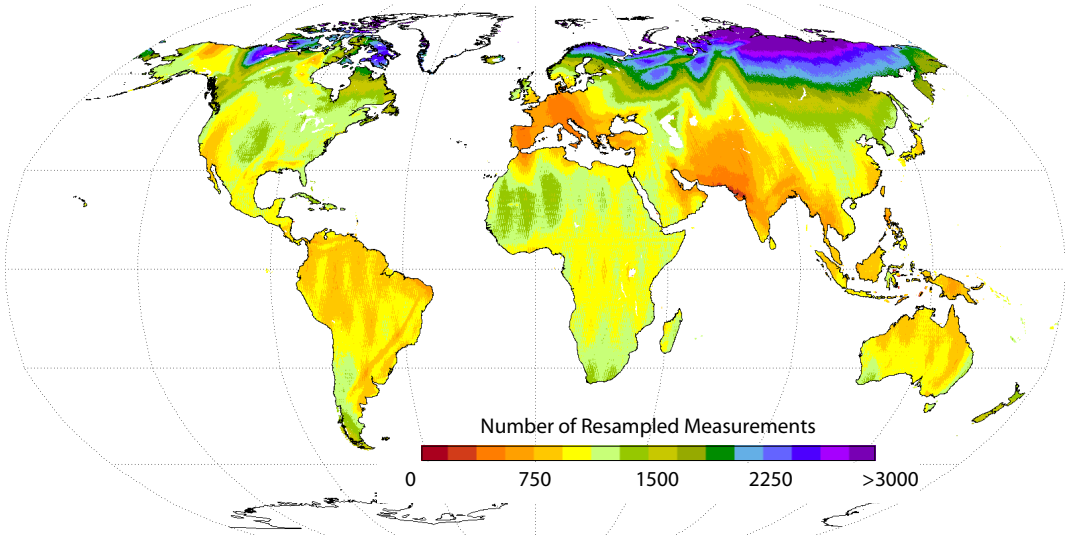

Figure 4-6. Number of measurements aggregated in DGG points.

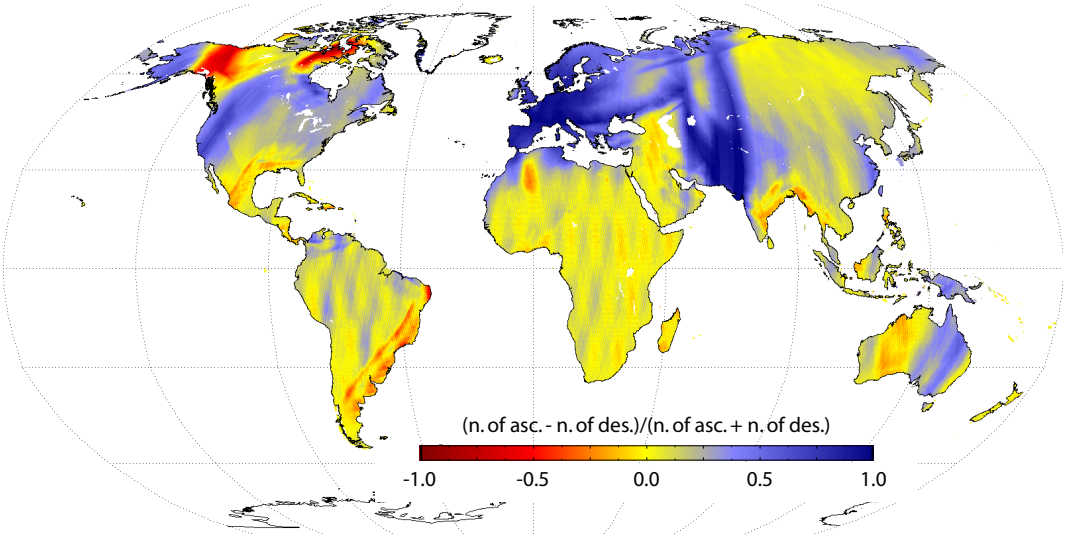

Figure 4-7. Normalized difference between number of ascending and descending measurements.

$$NN = \frac{Number\ of\ ascending - Number\ of\ descending}{Number\ of\ ascending + Number\ of\ descending} \tag{4-3}$$

4.2. Correction of Azimuthal Anisotropy of Backscatter

As it mentioned in chapter 3, in the TU-Wien method as implemented in WARP4, the azimuthal look direction is not taken into account in normalization of viewing geometry. Two of the three side looking antennas of SCAT look at the surface with the same incidence angle but from two different azimuth angles (the same is valid for ASCAT having two antenna triplets on each side of the satellite track). The intensity of the backscattered signal does not only depend on the incidence angle, but also on the azimuthal look direction. The WARP4 implementation of TU-Wien does not explicitly incorporate these effects, as they are generally weak. This simplification results in an artificial modulation of the signal in regions characterized by surface patterns and microreliefs (e.g. sand desert) with a distinct azimuthal orientation. Hence in the WARP retrieval method, the azimuthal anisotropy of backscatter is considered as noise of measurement. In WARP5 such effects are partly corrected using a normalization technique presented by Bartalis *et al.* (2006). In this method, a correction factor is applied to the backscatter measurements of each beam separately. To calculate the correction factors, a second order polynomial is applied to model the σ^0 variations with respect to the incidence angle θ for three possible azimuth angles (i.e. for each beam and for ascending and descending passes separately). The difference between these polynomials and the polynomial derived for the entire dataset is used as a correction bias. More detailed explanation of azimuthal noise before and after correction is given in chapter 5.

4.3. Calculation of Slope and Curvature

The relationship between σ^0 and θ in equation 3-3 is described by the slope σ' and curvature σ'' parameters. These two parameters characterize surface roughness and phenological cycle of the vegetation. The rate of vegetation change refers to the vegetation growth length, which varies depending on mean annual temperature, precipitation, incoming solar radiation as well as land cover type. Because of different soil moisture conditions during the year and therefore different backscatter values, it is not in practice possible to specify the incidence angle dependency of backscatter accurately by simply fitting a polynomial to the historical backscatter measurements. In WARP algorithm, instead of fitting polynomials to the σ^0 measurements, the multi-incidence angle capability of the instrument is used to calculate σ' and σ'' parameters from local slope values extracted from simultaneous observations.

4.3.1. Local Slope

Each backscatter triplet contains three concurrent measurements from a unique target on the surface that is observed from different incidence angles. Local slope values can be calculated by comparing the measurements from *mid* beam antenna with *for* and *aft* beam measurements (figure 4-8):

$$\sigma'_L\left(\frac{\theta_m-\theta_{a/f}}{2}\right)=\frac{\sigma^0_m(\theta_m)-\sigma^0_{a/f}(\theta_{a/f})}{\theta_m-\theta_{a/f}}, \tag{4-4}$$

where the index m stands for the mid-beam and the indices *a, f* for the aft or fore-beam.

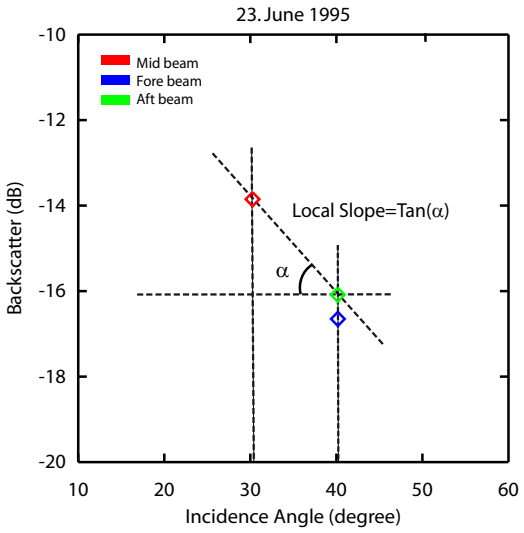

Figure 4-8. Calculation of local slope value.

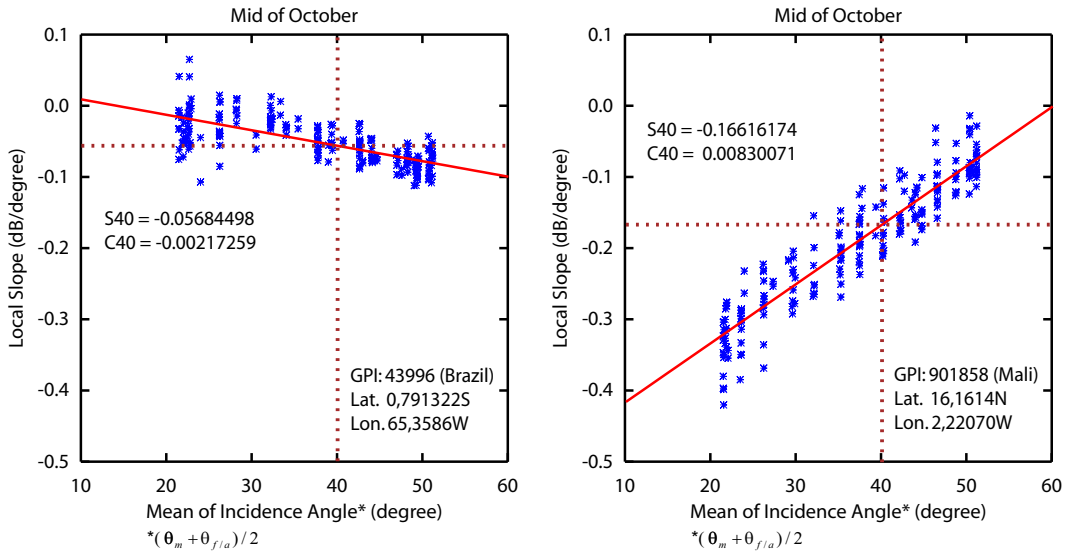

Figure 4-9. Slope and curvature parameters calculated from local slope values in two different regions.

4.3.2. Slope and curvature at 40° Incidence Angle

In order to parameterize the seasonal behavior of σ^0 with respect to θ, a first order polynomial is fitted to the local slope values calculated using equation 4-4 on a time window basis to estimate $\sigma'(\theta,t)$ and $\sigma''(\theta,t)$ parameters. Local slope values are calculated for a given day t from the paired backscatter measurements, which are observed within a given period τ. In this way, $\sigma'(40,t)$ and $\sigma''(40,t)$, the first and second derivatives of backscatter at 40° incidence angle are acquired, which are needed in equation 3-6 for the normalization of backscattering coefficients. Figure 4-9 shows local slope values versus the mean of incidence angles $\theta_{mean} = (\theta_m - \theta_{a/f})/2$ calculated for the mid of October in a period of one month in two different regions. It is assumed that 1) soil moisture variations do not or only minimally effect the local slope calculation and; 2) there is a linear relationship between local slope values and incidence angle. Considering these basic assumptions, the regression lines determine $\sigma'(40)$ and $\sigma''(40)$ values for the time t. By taking larger time window length τ, a more steady regression line fit is obtained. The model's goodness-of-fit for the slope parameter in global scale is illustrated in figure 4-10. In the older formulation the time window is set to one month. The reason for using monthly estimates was robustness with respect of noise, but one month sampling window filters high frequency variations. Furthermore, in some cases the applied empirical function $\psi(t)$ used in equations 3-4 and 3-5 can not satisfactorily describe natural variations. This problem is especially evident at the beginning of the vegetation development or vegetation dormancy onset.

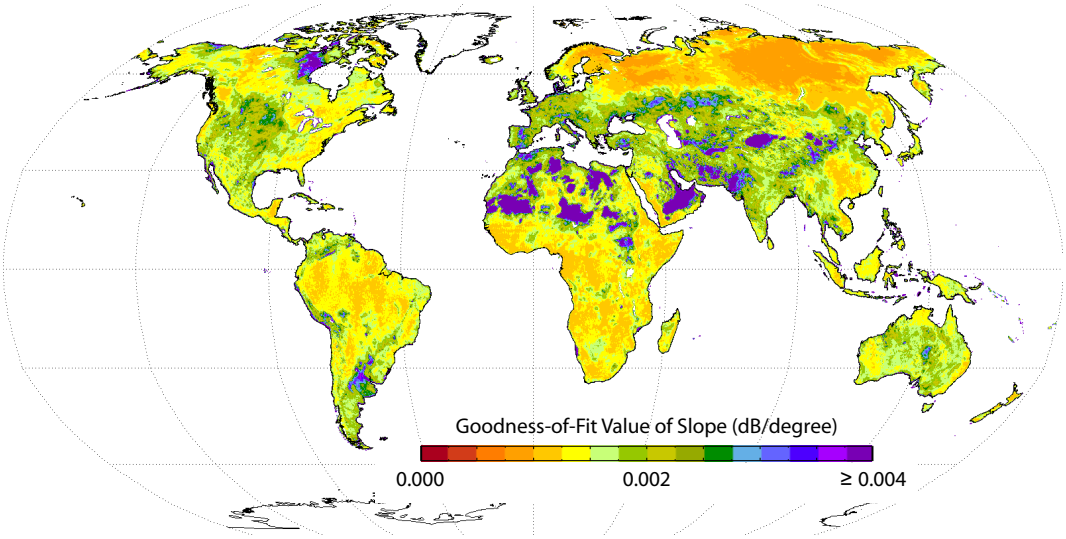

Figure 4-10. Global regression error (fitting error) of the slope parameter.

In WARP5 to quantify the impact of the time window length in estimation of σ' in equation 3-11, σ' is calculated for different values of τ , the period for which σ^0 measurements are sampled for the slope calculation:

$$\sigma'(\theta,\tau)=\sigma'(40,\tau)+\sigma''(40,\tau)(\theta-40) \tag{4-5}$$

In determination of slope and curvature functions $\sigma'(40,t)$, $\sigma''(40,t)$ it is important to catch all temporal surface roughness variations which is assumed to be mainly vegetation change during the year. In other words the period τ should be chosen short enough that vegetation can be consider invariant in that period. It should however be noted that there is a lower limit in defining τ , as the noise of the slope and curvature functions $\sigma'(40,t)$ and $\sigma''(40,t)$ increase with a decreasing number of measurements. On the other hand the period, in which vegetation can be considered constant, differs regarding the diversity of global climate. For example vegetation growth length in southern regions of high latitudes takes three times longer than in northern parts (Zhang et al. 2002). In addition, the vegetation growth length in some regions varies slightly from year to year due to the regional climate change (White et al. 1999). Figure 4-11 shows daily slope and curvature in a grid point located in Kansas, USA. In this example σ' and σ'' parameters are calculated by setting τ value respectively to 1 and 12 weeks. Setting τ to one week guarantees that seasonal variations of the slope and curvature are well captured. However, the resulting estimates appear very noisy. Setting τ to 12 weeks results in a smooth estimate which reflects the general vegetation cycle but this eliminates a considerable part of the variation. Therefore

calculation of slope and curvature functions with a fixed time window length for the whole globe does not seem to be an appropriate solution. To overcome this caveat and have a trade off between a noisy but sensitive and a stable but less responsive σ' a method similar to Monte Carlo (MC) simulation (Niederreiter 1992) is employed with a range of τ values to have an averaged estimate of slope and curvature parameters. It is in general assumed that for 50km resolution the vegetation change is not globally remarkable in less than 2 weeks period and the seasonal vegetation change does not take longer than 12 weeks. In this way $\sigma'(40)$ is determined as the mean of simulated $\sigma'(40,\tau)$ values given a large quasi-random numbers of τ ranging between 2 and 12 weeks as input of the simulation:

$$\sigma'(40) = \frac{1}{M}\sum_{i=1}^{M}\sigma'(40,\tau_i), \tag{4-6}$$

where M is the number of the evaluations in the MC simulation and τ is random numbers ranging between $[14,84]$ days.

The same method used for the slope calculation is applied for determination of the curvature $\sigma''(40)$, the second derivative of $\sigma^0(\theta)$ at 40°:

$$\sigma''(40) = \frac{1}{M}\sum_{i=1}^{M}\sigma''(40,\tau_i) \tag{4-7}$$

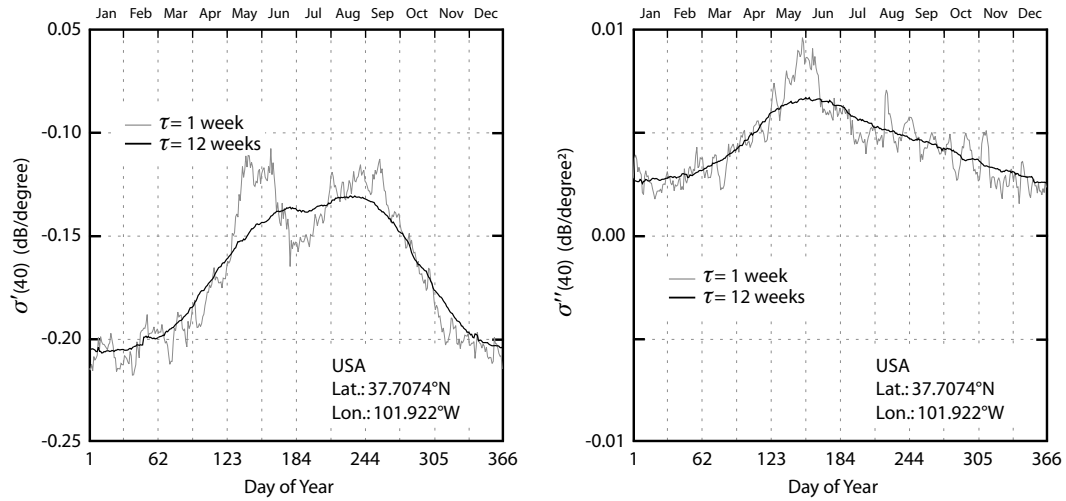

Figure 4-11. Daily slope and curvature parameters calculated for two different time window lengths.

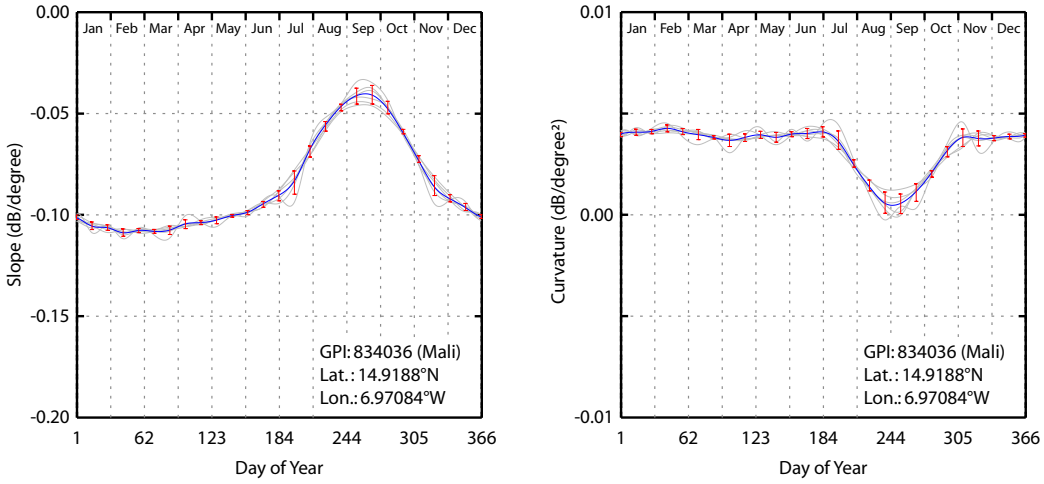

Figure 4-12. Mali; Africa, calculation of the slope and curvature functions.

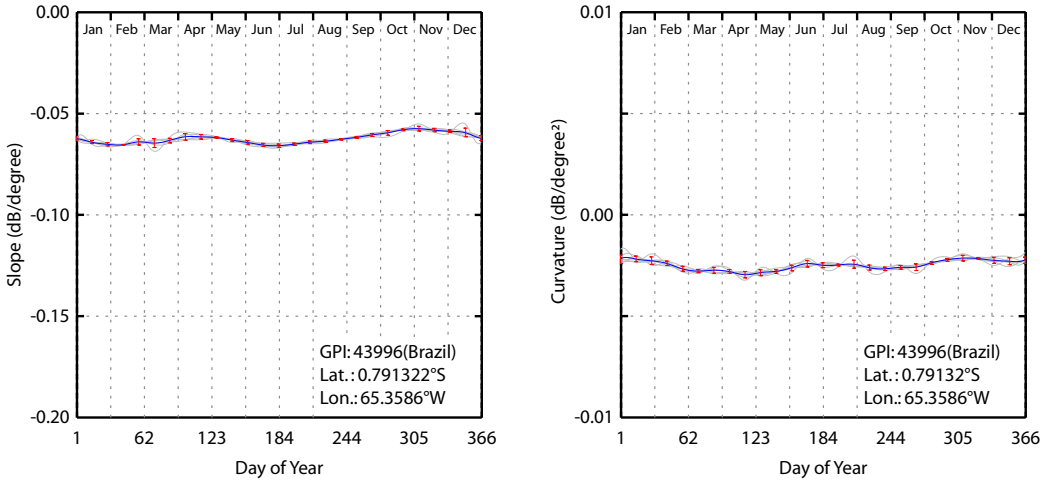

Figure 4-13. Brazil, S. America; calculation of the slope and curvature functions.

In WARP5 instead of using empirical functions $\psi'(t)$ and $\psi''(t)$ introduced in WARP4, a cubic spline interpolation technique with biweekly intervals is performed to obtain uniform slope and curvature functions $\sigma'(40,t)$, $\sigma''(40,t)$. Figure 4-12 and 4-13 show the new slope and curvature functions calculated for two different WARP5 grid points. Figure 4-12 indicate slope and curvature in a grid point located in Mali, Africa with high annual vegetation variation. Figure 4-13 illustrates another example of $\sigma'(40,t)$ and $\sigma''(40,t)$ functions estimated for a grid point located in rainforest in Brazil without significant change in vegetation during the year. Figure 4-14 compares the slope and curvature functions calculated in WARP4 and WARP5 algorithms for the grid point indicated in Figure 4-11 located in Kansas, USA. As it is evident in this figure, the WARP5 slope and curvature functions (blue curves) follow the natural variations much better than the applied empirical functions, $\psi'(t)$ and $\psi''(t)$ in WARP4. The double peaks observable

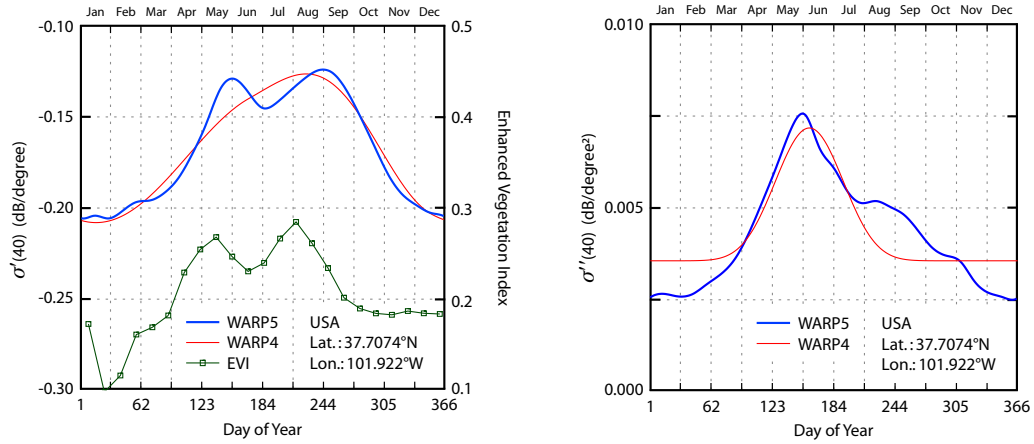

Figure 4-14. Kansas, USA; the slope and curvature functions calculated in WARP4 and WARP5. The slope function is compared with 16-day MODIS Enhanced Vegetation Index data, which are averaged over 3 years (2000-2002).

in the WARP5 slope function, caused probably by farming activities in the region, could not be detected by the old method. Such rapid variations of the vegetation canopy within a year can also be observed in vegetation indices extracted from the 16-day MODIS/Terra data (Huete et al. 2002). Using the new method, a more accurate fit of the slope and curvature functions are established, especially at the beginning of the vegetation development or vegetation dormancy onset and when the biomass reaches its maximum maturity.

Inaccurate calculation of slope and curvature parameters leads eventually to increasing uncertainty in soil moisture estimation. Figure 4-15 shows a simulation example of how a

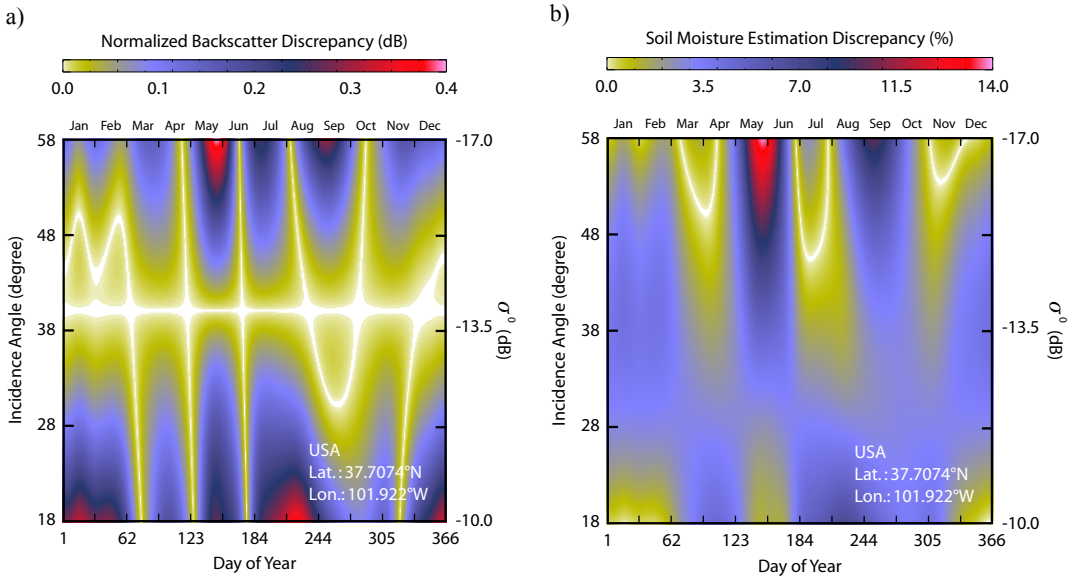

Figure 4-15. Simulation of; a) normalized backscatter b) and soil moisture regarding deviation of slope and curvature functions in WARP4 algorithm compared toWARP5.

wrong slope estimation influence the calculation of normalized backscatter and soil moisture. The impact of wrong slope calculation on soil moisture varies depending on backscattering coefficient, incidence angle, and time of the year. In general with increasing incidence angle the backscattering coefficient decreases. The effect of slope parameter is intensified with increasing the deviation of incidence angle from the reference incidence angle and also time of year when the slope reaches to its maximum value. In this example wrong slope value makes up to 14% error in soil moisture estimation. Discrepancy between slope and curvature functions in WARP4 and WARP5 are illustrated in figure 4-16 in terms of Root Mean Square Error (RMSE).

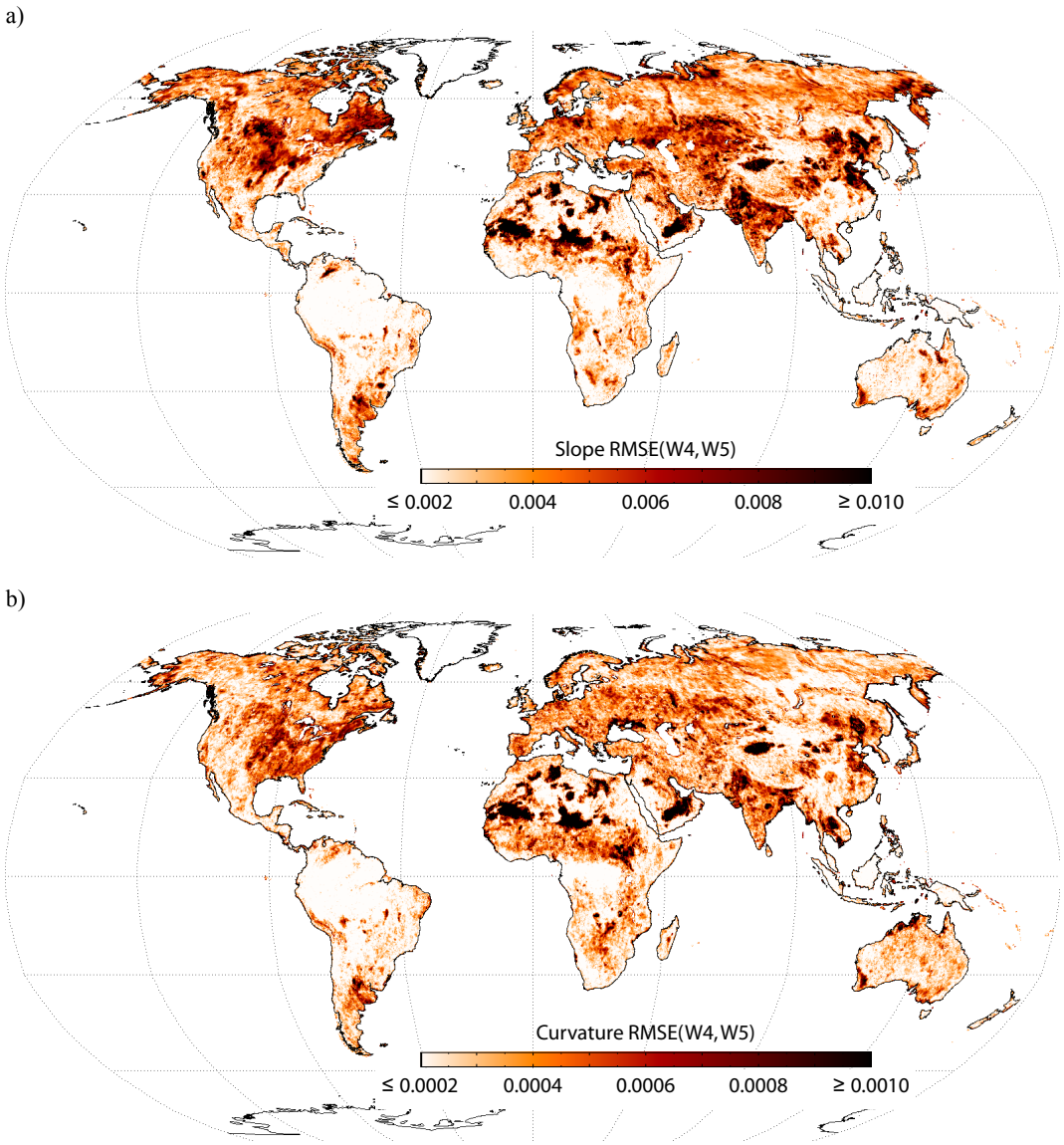

Figure 4-16. a) Root mean square difference of the slope and; b) curvature functions calculated respectively in WARP4 and WARP5 algorithms.

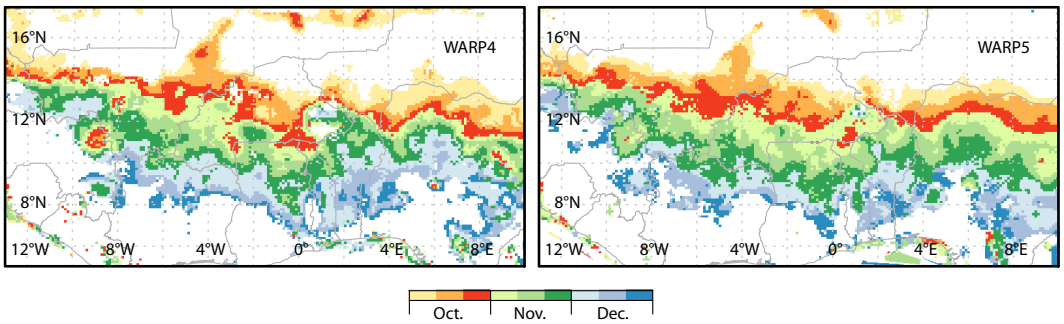

Figure 4-17. Time of year when the slope reaches its maximum value across Sahelian zone in Africa.

Figure 4-17 indicates the time of year when the slope function reaches its highest value in two different algorithms. In some instances, there is more than 10 days difference in estimation of the maximum slope meaning that the calculated slope function is shifted from its actual value.

4.3.3. Seasonal Variations of Slope and Curvature

As it was mentioned in chapter 3, the incidence angle dependency of backscatter from bare soil is remarkably different than from vegetation canopy. The backscattering from bare soil decreases rapidly with increasing incidence angle. Conversely, the governing mechanism of backscatter from vegetated surface is mainly volume scattering and the backscattering is quite uniform over a large range of incidence angles. By increasing the biomass the transmissivity of the vegetation canopy decreases, the volume scattering is intensified compared to the surface scattering contribution and the slope function becomes less steep. In general, slope parameter follows the climatic conditions. It is maximum (with low gradient) in summer when the biomass reaches to its highest value and minimum (with higher gradient) in winter when the biomass has its lowest value. Variations of slope and curvature parameters can be seen distinctly from scatterometer data. Figure 4-18-a and b show the slope and curvature dynamics. The highest variations of the slope parameter are observed in farming lands and steppe. The slope and curvature both have the lowest dynamic over rain forest, where the vegetation is dense, and also over the areas where vegetation is not changing remarkably during the year and consequently have no influence on backscattering behavior of surface when the season changes. Figure 4-19 and 4-20 illustrate the slope and curvature values in the mid of January and July. The time of year where the maximum and minimum of slope parameter is observed show respectively the highest and the lowest biomass during the year (Figure 4-21-a and b). The highest slope values can be observed around July and August for the most parts of northern hemisphere and from October to March for the areas located in southern hemisphere. In Africa, north of

the Equator, the maximum slope is observed during September to December depending on the position of Intertropical Convergence Zone (ITCZ). In this regions Biomass growth depends strongly on the period of rainfall season and the temperature cycle. Plants cannot grow during the dry period from November to May. The vegetation development begins in July after rainfall season and reaches to its maximum with some delays in different latitudes following the fluctuations of ITCZ within the year.

a)

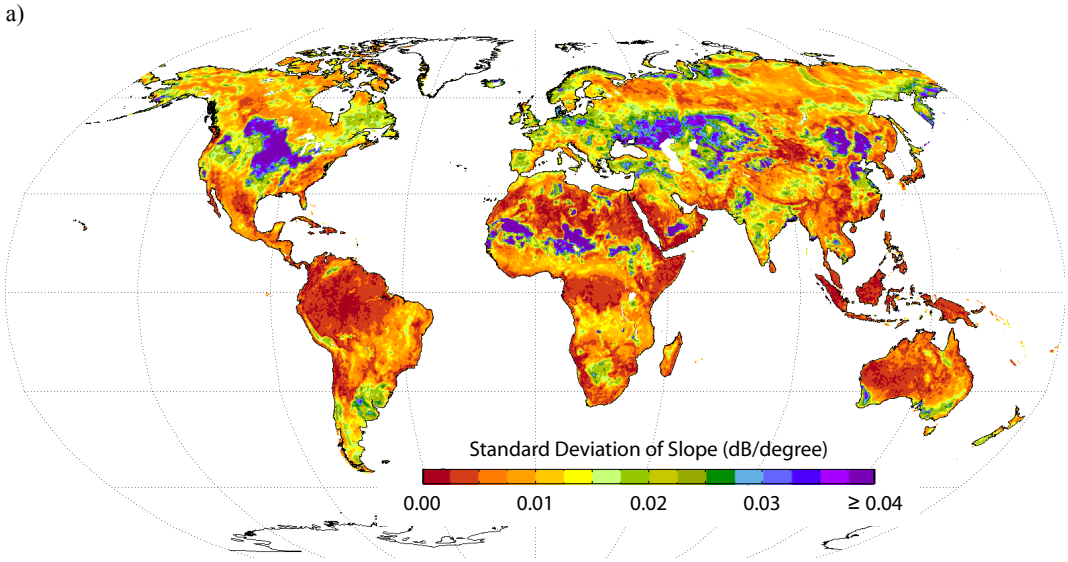

b)

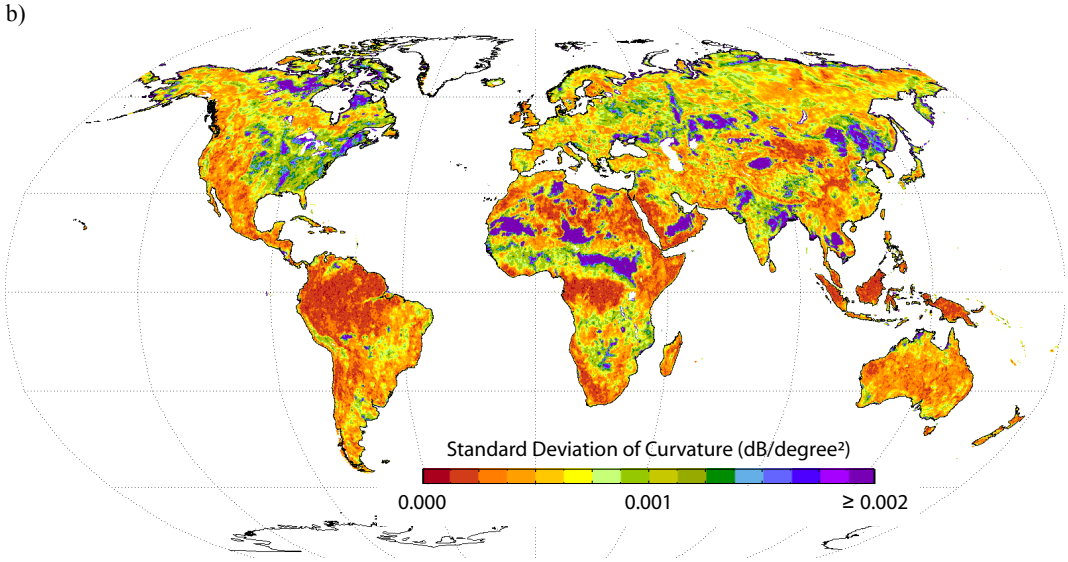

Figure 4-18. a) Standard deviation of slope function. b) Standard deviation of curvature function.

a)

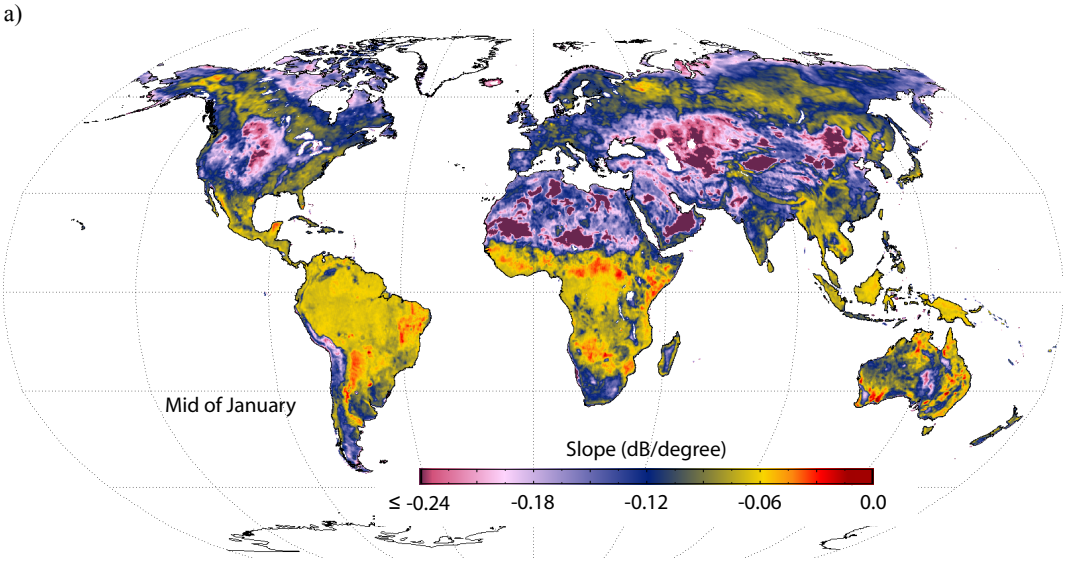

b)

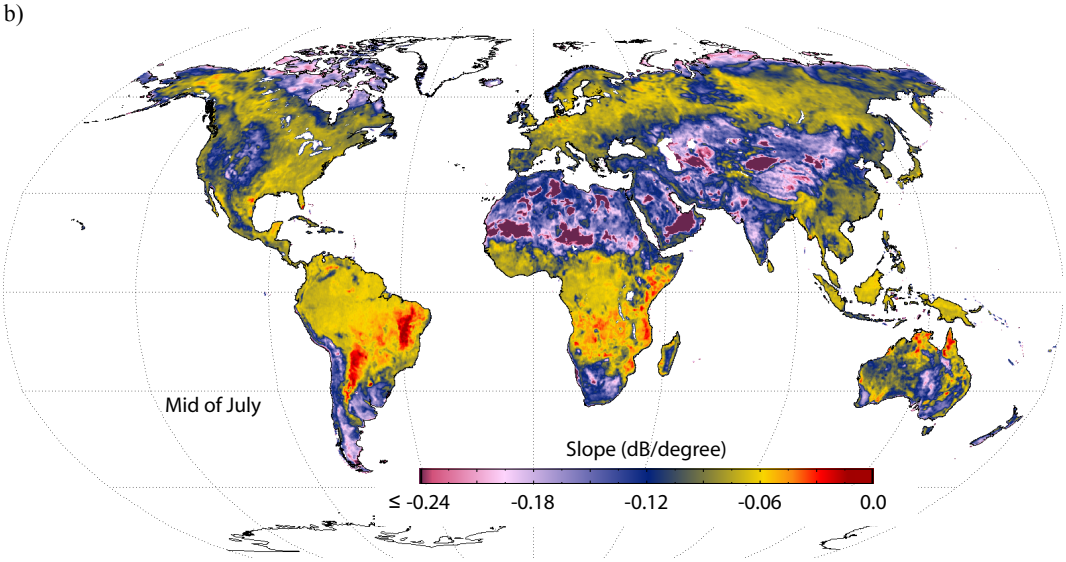

Figure 4-19. a) Slope values in January. b) Slope values in July.

a)

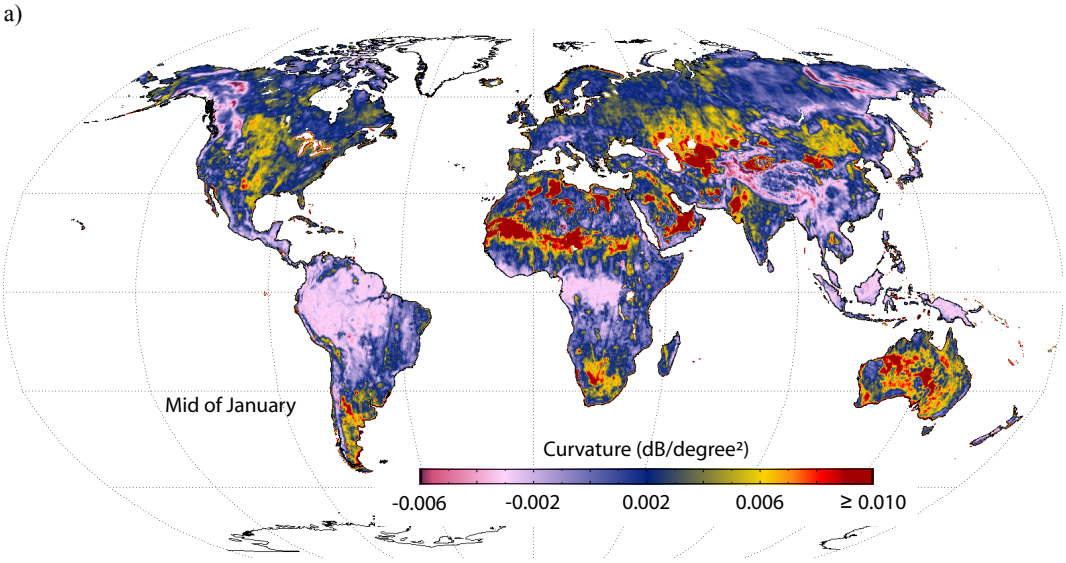

b)

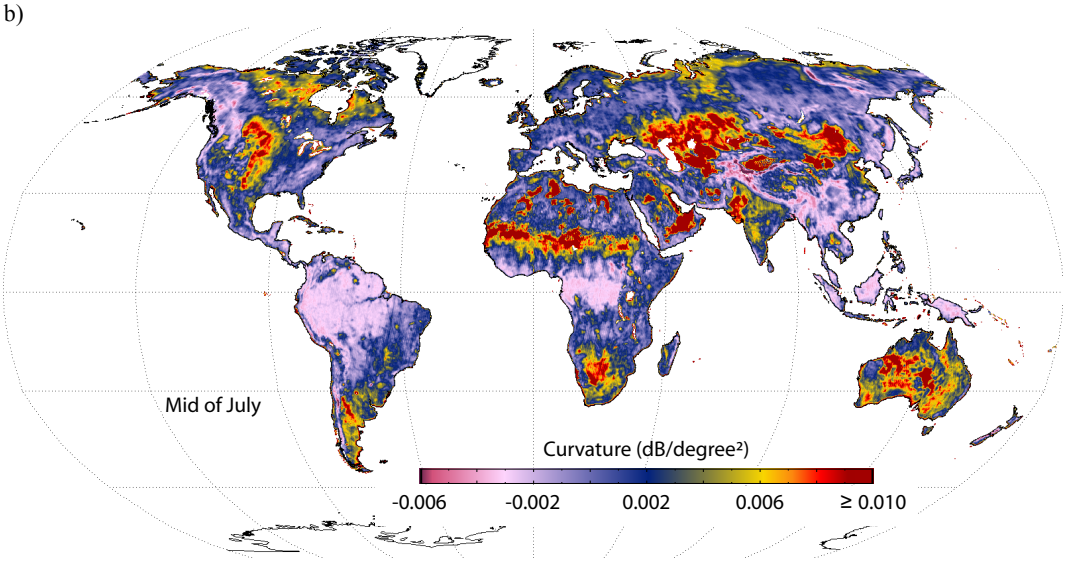

Figure 4-20. a) Curvature values in January. b) Curvature values in July.

a)

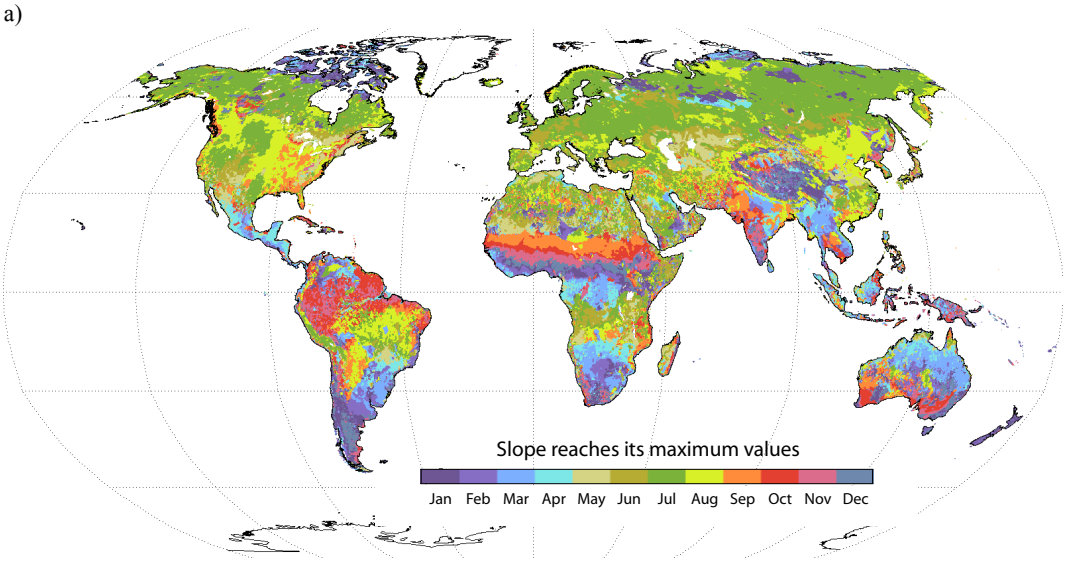

b)

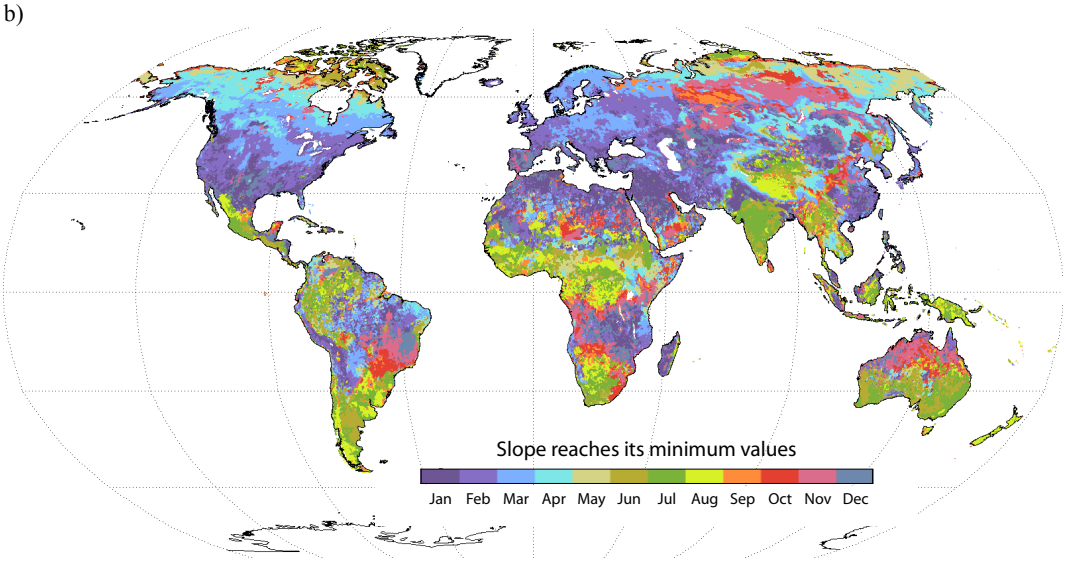

Figure 4-21. Time of year with; a) maximum and b) minimum slope value.

4.4. Normalization of Backscatter

According to the Taylor series expansion, the backscattering coefficients can be extrapolated about a reference incidence angle if the values of derivatives at the reference incidence angle are known. Equation 3-3 is used in WARP algorithm as an approximation of the Taylor expansion with two derivatives. Using the slope and curvature functions obtained from (4-6) and (4-7), the normalized backscattering coefficients are calculated separately for each beam of scatterometer. Subsequently the normalized backscattering coefficients, acquired from triplet measurements, are averaged:

$$\sigma^0(40,t) = \frac{1}{3}\sum_{i=1}^{3}\sigma_i^0(40,t) \tag{4-8}$$

Figure 4-22 illustrates the mean of normalized backscatter on global scale. In general, high backscatter values are observable in areas with dense vegetation or regions characterized with complex topography. The normalized backscatter varies depending on soil moisture condition and vegetation change. As it is mentioned in chapter 4, there is a linear relationship between $\sigma^0(40)$ and surface soil moisture content (Ulaby et al. 1982). In order to extract soil moisture dynamics, $\sigma^0(40)$ measurements should be scaled between the lowest and the highest values of long-term backscatter observations after excluding vegetation contribution in backscatter signal.

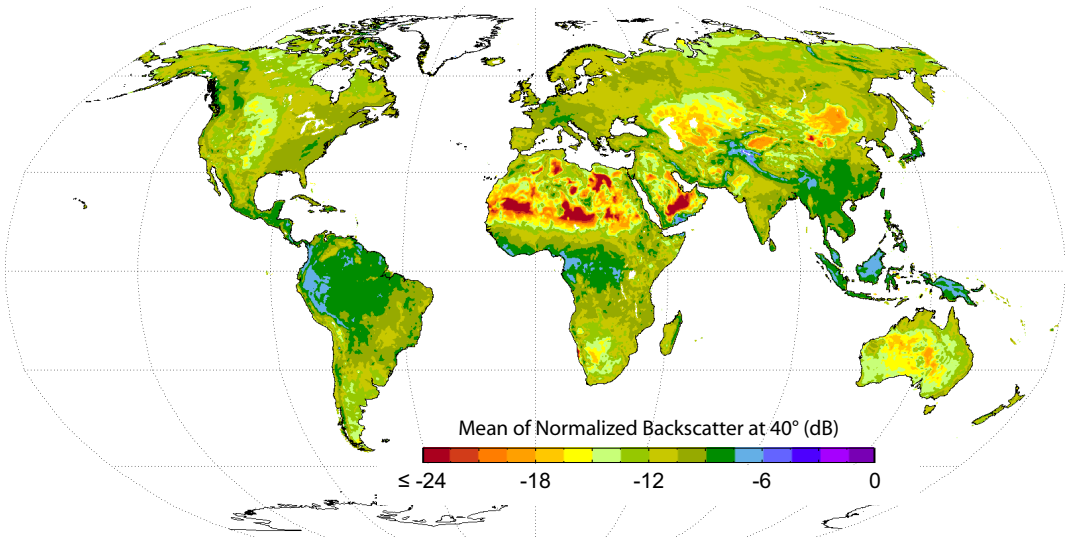

Figure 4-22. Average of normalized backscatter globally.

4.5. Scaling of Normalized Backscatter

The TU-Wien soil moisture retrieval algorithm is in principle a change-detection method that relates $\sigma^0(40,t)$ to the lowest and highest values of $\sigma^0(40)$ that have ever been recorded. The lowest and highest values, $\sigma^0_{dry}(40,t)$ and $\sigma^0_{wet}(40,t)$ are supposed to be references of the driest and the wettest conditions of soil surface. A significant step before determination of the dry and wet references, is removing outliers in the $\sigma^0(40)$ time series. This should be done carefully to avoid taking out the true measurements.

4.5.1. Outliers Removal

By definition outliers are data points that are further away from their expected values than what is supposed reasonable. To detect outliers in a distribution, a simple definition of being far away in this context is being below $(Q_1 - C \cdot IQR)$ or beyond $(Q_3 + C \cdot IQR)$. The Q_1 and Q_3 are the 1st and 3rd quartiles, IQR is the inter-quartile $(Q_3 - Q_1)$, and C is a coefficient, which is set according to each data distribution (Renze 2007).

The outliers in the $\sigma^0(40)$ distribution are representing faulty data because of systematic errors like instrument malfunctioning or situations where the algorithm might not be valid. Figure 4-23 indicates the utmost values of the normalized backscatter distribution, an example of existing outliers in measurements. In WARP5, such outliers are detected in two separate phases during the calculation of dry and wet references. In the first step, values greater than $3 \times IQR$ from the first and third quartiles are removed from the $\sigma^0(40)$ distribution. After separating extreme low and high values in the $\sigma^0(40)$ distribution, the outlier removal procedure is performed once again to remove values greater than $3 \times IQR$ beyond Q_1 and Q_3 in both groups of the extreme low and high observations.

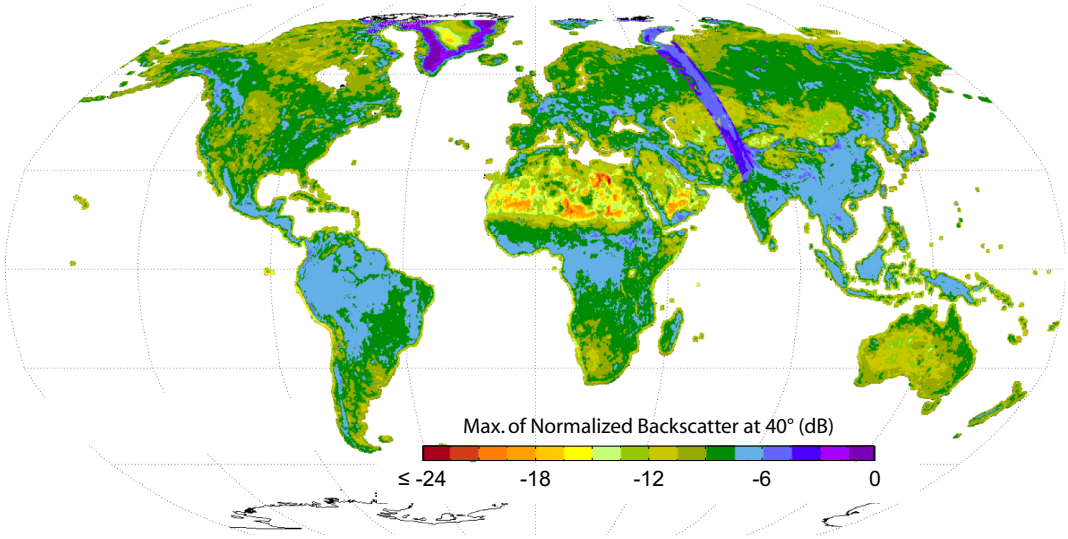

Figure 4-23. Outliers in the global distribution of the highest normalized backscatter values.

4.5.2. Determination of Dry and Wet References

The backscatter coefficients under dry and wet conditions are estimated by taking the average of the extreme lowest and highest measurements. In WARP4 the number of observations, which are used for averaging of the extreme measurements, is kept constant ignoring the regional differences in noise level. In WARP5, the extreme low values in $\sigma^0(\theta_{dry})$ and the extreme high values in $\sigma^0(\theta_{wet})$ distributions are separated with respect to an explicit uncertainty range, defined as a 95% 2-sided confidence interval of the measurements. The confidence interval of the extreme low and high values is obtained by considering the noise of $\sigma^0(\theta_{dry})$ and $\sigma^0(\theta_{wet})$:

$$\text{Confidence Interval} = \pm 1.96 \times (\text{Noise of } \sigma^0(\theta)) \tag{4-9}$$

The value 1.96 represents the 97.5 percentile of the standard normal distribution, which is often rounded to 2 for simplicity. The calculation method of the noise of $\sigma^0(\theta)$ is presented in chapter 7. Consequently, the mean values of the separated extreme observations are considered as dry and wet references at the presumed crossover angles:

$$C^0_{dry} = \frac{1}{N_{lower}} \sum_{j=1}^{N_{lowet}} \sigma^0_j(\theta_{dry}), \tag{4-10}$$

$$C^0_{wet} = \frac{1}{N_{upper}} \sum_{j=1}^{N_{upper}} \sigma^0_j(\theta_{wet}), \tag{4-11}$$

where N_{lower} and N_{upper} are the number of low and high extreme values in the $\sigma^0(\theta_{dry})$ and $\sigma^0(\theta_{wet})$ distributions respectively.

4.5.3. Vegetation Correction

To scale $\sigma^0(40)$, dry and wet references are needed at the reference incidence angle. Knowing C^0_{dry} and C^0_{wet} and considering equation 3-6, dry and wet references at 40° are calculated as follows:

$$\sigma^0_{dry}(40,t) = C^0_{dry} - \sigma'(40,t)(\theta_{dry} - 40) - \frac{1}{2}\sigma''(40,t)(\theta_{dry} - 40)^2, \tag{4-12}$$

$$\sigma^0_{wet}(40,t) = C^0_{wet} - \sigma'(40,t)(\theta_{wet} - 40) - \frac{1}{2}\sigma''(40,t)(\theta_{wet} - 40)^2. \tag{4-13}$$

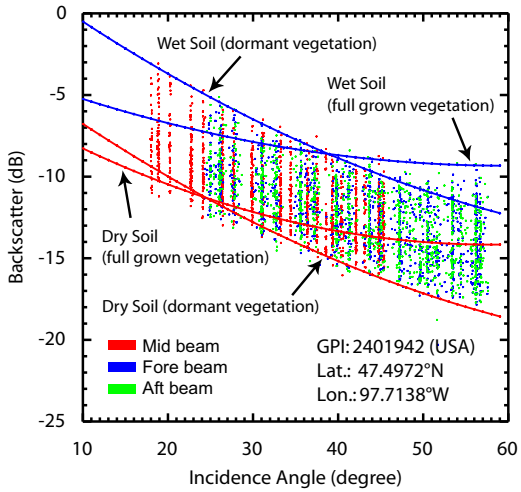

Figure 4-24. Crossover angles are points where vegetation has no effect.

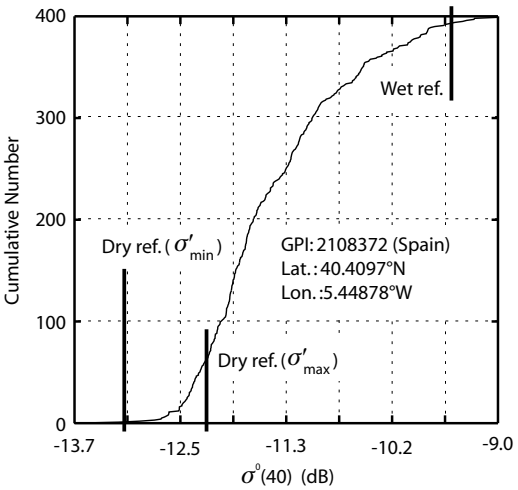

Figure 4-25. Cumulative distribution of normalized backscatter and dry/wet references.

Equations 4-12 and 4-13 imply that the dry and wet references vary during the year depending on the incidence angle deviation from the dry/wet crossover angles and also the condition of vegetation canopy, which is reflected in the slope and curvature. This comprises a vegetation correction in soil moisture estimation if the crossover angles are chosen correctly. In WARP algorithm, crossover angles are set to $\theta_{wet} = 40°$ and $\theta_{dry} = 25°$ (figure 4-24). Figure 4-25 indicates the dry and wet references calculated in WARP5 together with the cumulative distribution of $\sigma^0(40)$ for a grid point in Spain. Setting $\theta_{wet} = 40°$ and $\theta_{dry} = 25°$ generate a constant wet reference but dynamic dry reference (figure 4-26). Figure 4-27 illustrates global extent of the minimum level of dry reference, wet reference, and the sensitivity ($\sigma^0_{wet}(40) - \sigma^0_{dry}(40)$).

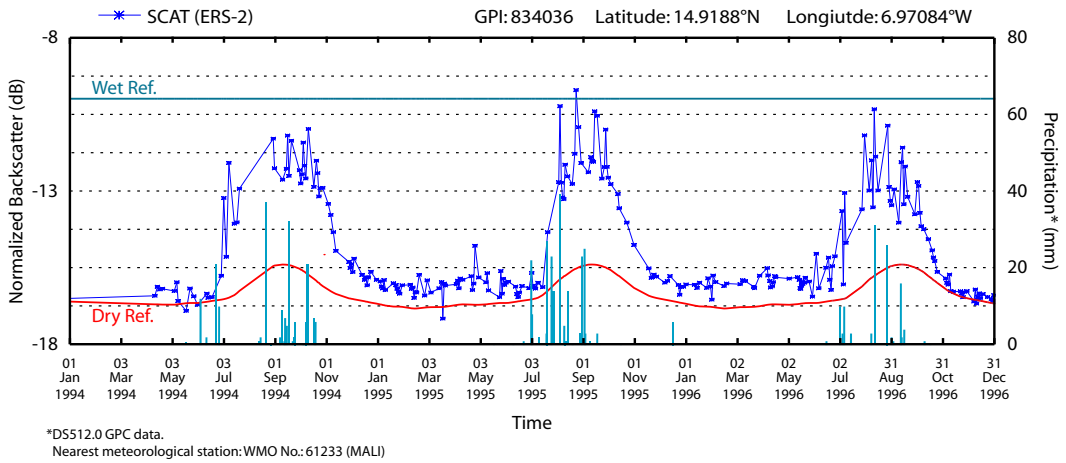

Figure 4-26. Mali, Africa; time series of normalized backscatter and dry/wet references.

a)

b)

c)

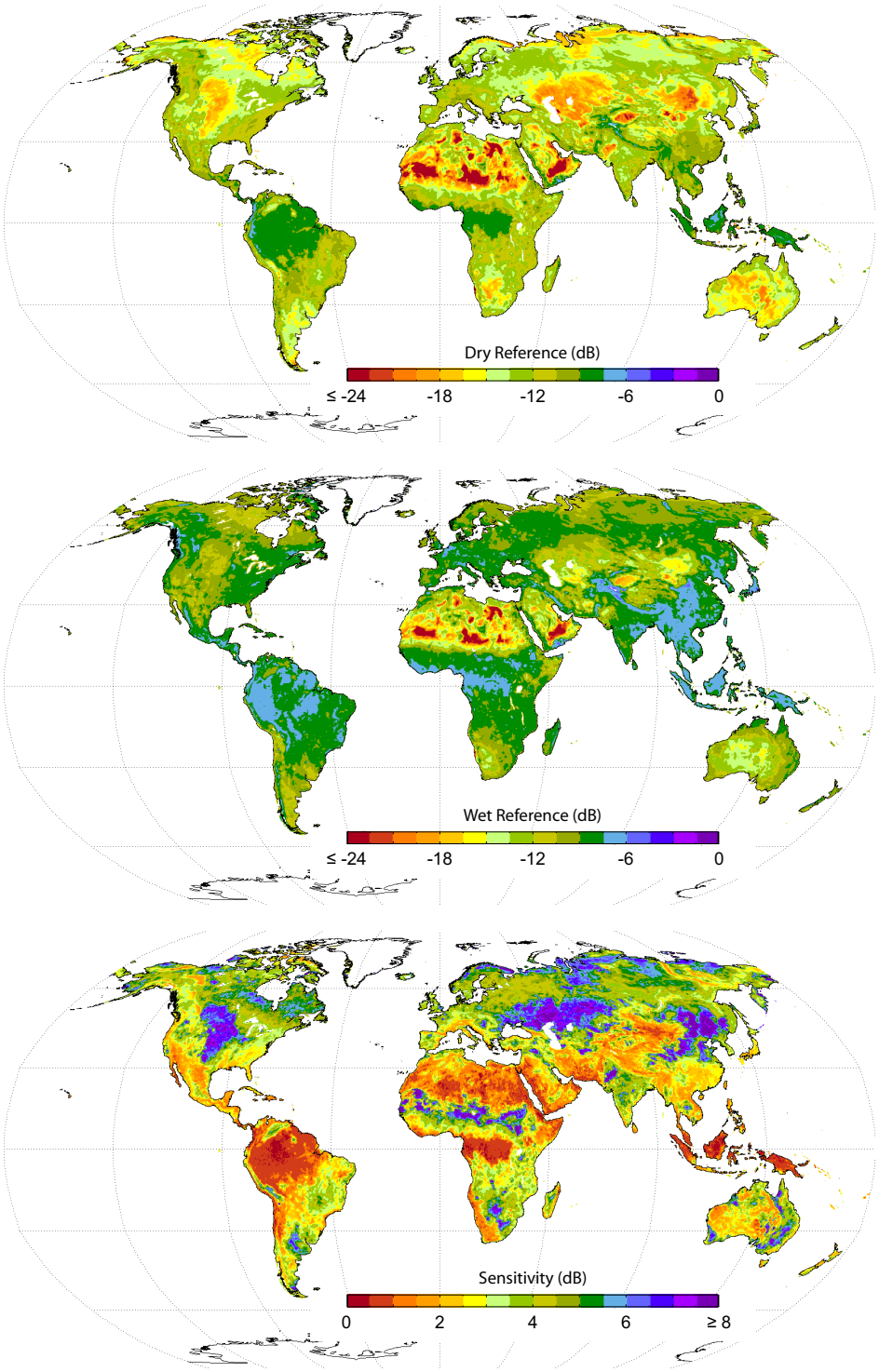

Figure 4-27. Global maps of the; a) lowest level of dry reference, b) wet reference, c) sensitivity.

4.5.4. Wet Correction

In WARP5, an empirical bias-correction factor is applied to $\sigma^0_{wet}(40)$ based on the wet reference and sensitivity. The bias-correction is performed in two steps. In the first step the lowest level of the wet reference is set to -10dB. Then in areas with dry and hot climate where the saturation condition is probably never observed, the $\sigma^0_{wet}(40)$ values are raised until the sensitivity reaches to at least 5dB. Extreme dry regions are identified by using the external climate data (Kottek et al. 2006). Although the new correction method provides a more spatially uniform wet correction, it is still an interim solution like the earlier method.

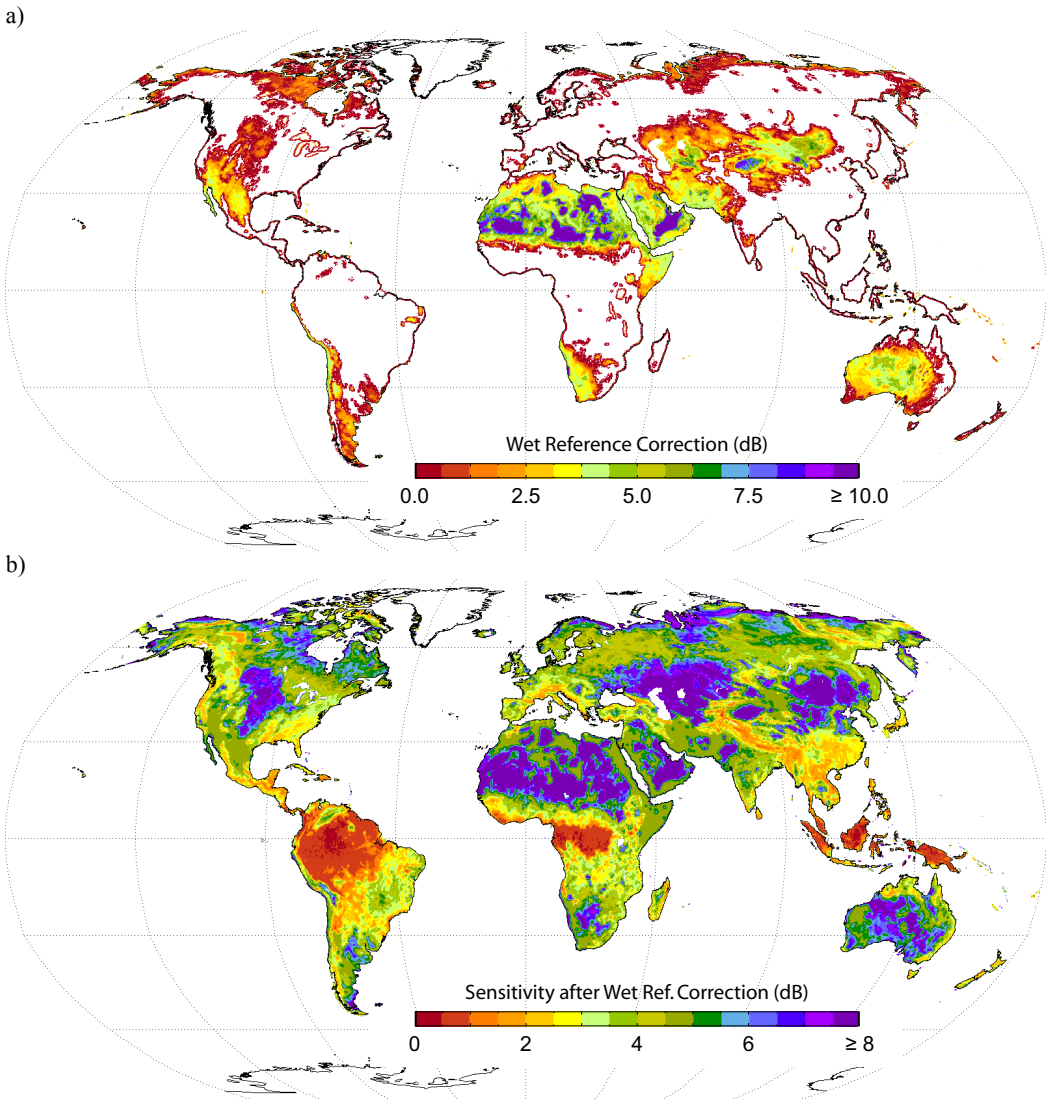

Figure 4-28. a) Wet correction. B) Sensitivity after wet correction.

4.5.5. Surface Soil Moisture

According to equation 3-9, the normalized backscatter $\sigma^0(40)$ is scaled between $\sigma^0_{dry}(40,t)$ and $\sigma^0_{wet}(40)$, which are calculated for each day of year t, to obtain the degree of saturation Θ_s equivalent to normalized volumetric soil water content. The Θ_s represents soil moisture dynamics and ranges between 0 and 1 (0%-100%). Figure 4-29 shows a qualitative comparison of surface soil moisture time series derived from SCAT and ASCAT observations with the precipitation measurements at the nearest synoptic station in lower Austria. The scatterometer observations correlate well with precipitation records. High Θ_s values are clearly linked to rainfall events and low Θ_s values occur after a period without rain or during frost periods.

Figure 4-30-a and b illustrate the mean of Θ_s calculated for the mid of January and July. The $\overline{\Theta}_s$ is extracted from the available long-term ERS-1 and ERS-2 scatterometers data acquired from August 1991 to May 2007. The spatial variability of the $\overline{\Theta}_s$ reflects atmospheric-forcing related soil moisture signal. The averaged degree of saturation generally follows the climatic trends with low values during dry season and high values during spring and autumn. However, in high latitudes, where the average temperature of the soil during the cold season is often far below 0°C, soil appears dry in scatterometer observations as backscatter from frozen soil behaves similar to dry soil. During spring when the soil temperature increases to above frozen point, wet soil becomes again visible for scatterometer observations. At microwave frequencies, freezing results in a strong decrease of the dielectric constant of soil and vegetation. Therefore, it is not possible to retrieve soil moisture information from scatterometer data when the soil is frozen.

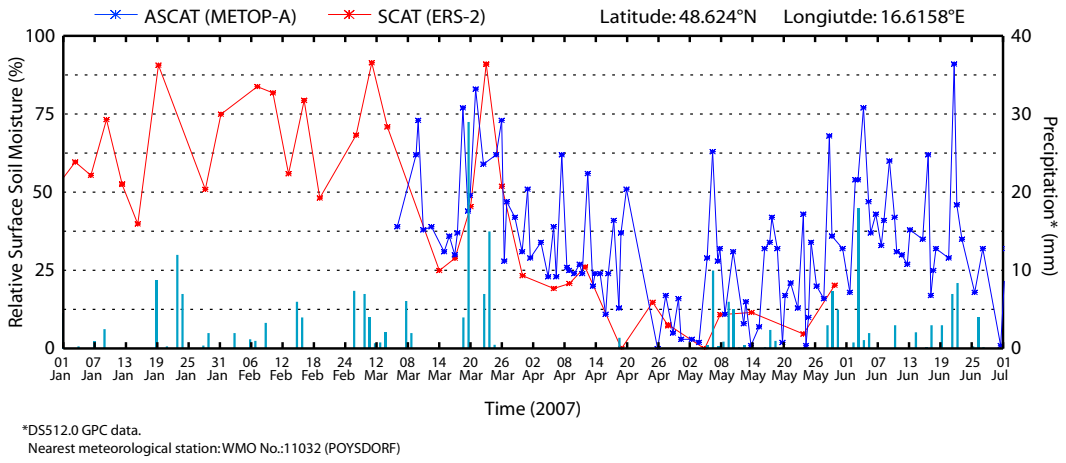

Figure 4-29. Soil moisture time series retrieved from SCAT and ASCAT data.

a)

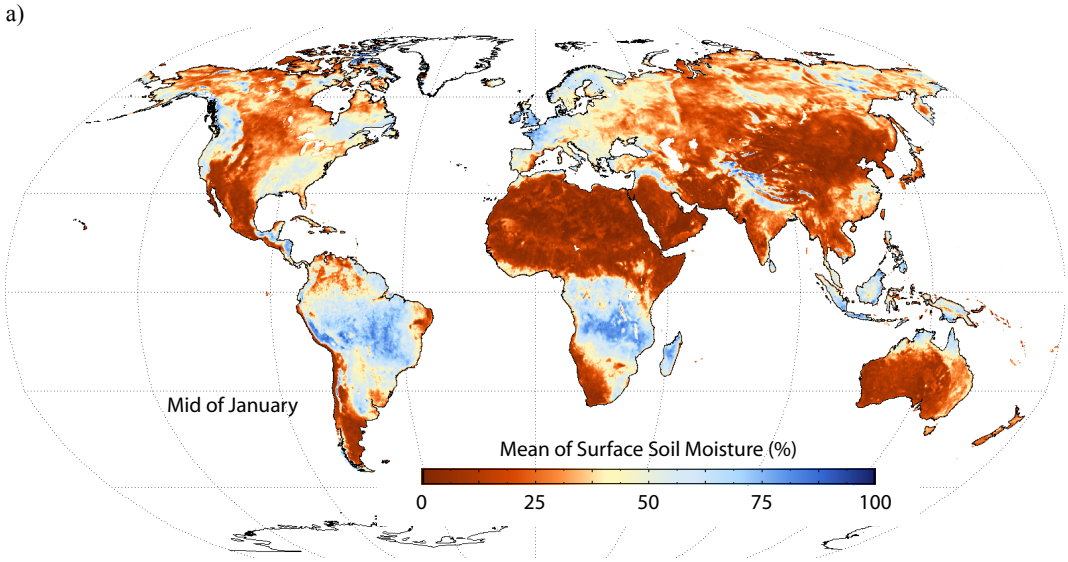

b)

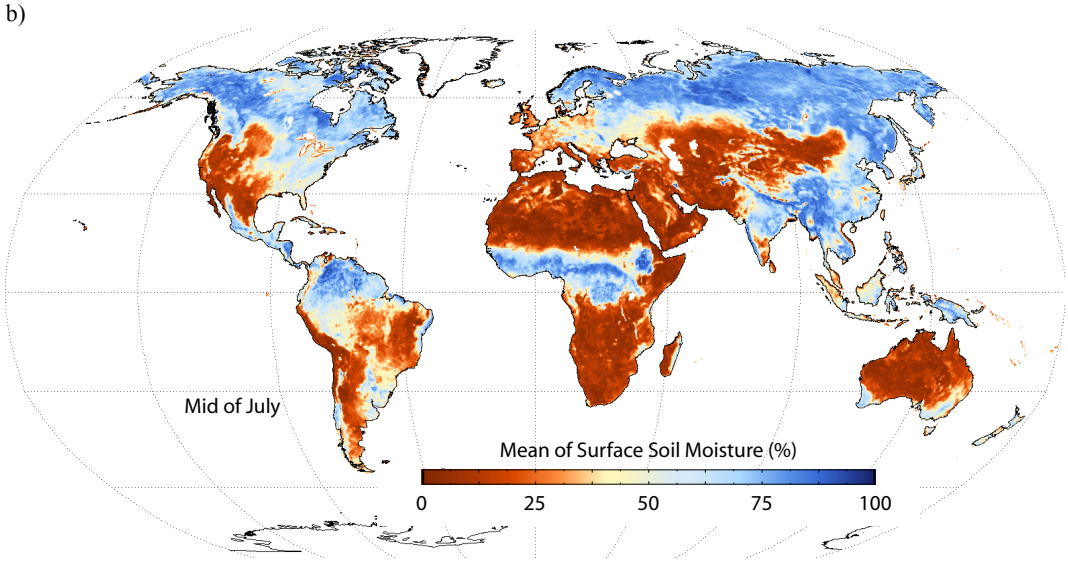

Figure 4-30. The estimated soil moisture in mid of; a) January and b) July averaged over the long-term scatterometer observations from August 1991 to May 2007.

5. Noise of Backscatter

5.1. Radiometric Resolution

The backscattering signals measured by scatterometers are affected by instrument noise as well as the noise induced by geophysical phenomena. In the ERS scatterometer signal processing system, to improve the instrument accuracy, the receiver noise power is measured separately and then subtracted from the backscattered signal. The noise measurements and system calibration are obtained within a dwell period between the transmission of each pulse and the arrival of the first radar echo signal (Attema 1991). A commonly used parameter for evaluation of the backscattering measurement accuracy is "Kp", defined as the normalized standard deviation of σ^0 , which is a measure of radiometric resolution of the scatterometer, expressed in percentage. The radiometric resolution of the instrument indicates the ability of the sensor to differentiate the backscattered energy. A general goal in scatterometer design is to minimize the Kp value (Naderi et al. 1991). In this way each σ^0 value is described by the accuracy at which it has been measured. The Kp of the averaged measurement in each node, $\overline{\sigma}^0_{node}$ is estimated as the standard noise within the averaging area defined by the Hamming window (Wilson et al. 2005):

$$Kp = \frac{\sqrt{\mathrm{var}(\sigma^0_{node})}}{\overline{\sigma}^0_{node}}, \tag{5-1}$$

Figure 5-1 shows the mean values of Kp averaged over three months of the year 1996, which are measured by the ERS-2 scatterometer separately for each triplet beams. It should be noted that the Kp value is an engineering parameter to measure the instrument efficiency and does not reflect the noise of geophysical parameter. Therefore an appropriate noise model is needed to be developed in relation to the geophysical model function. The noise model enables the quality of the data and geophysical retrieval method to be assessed.

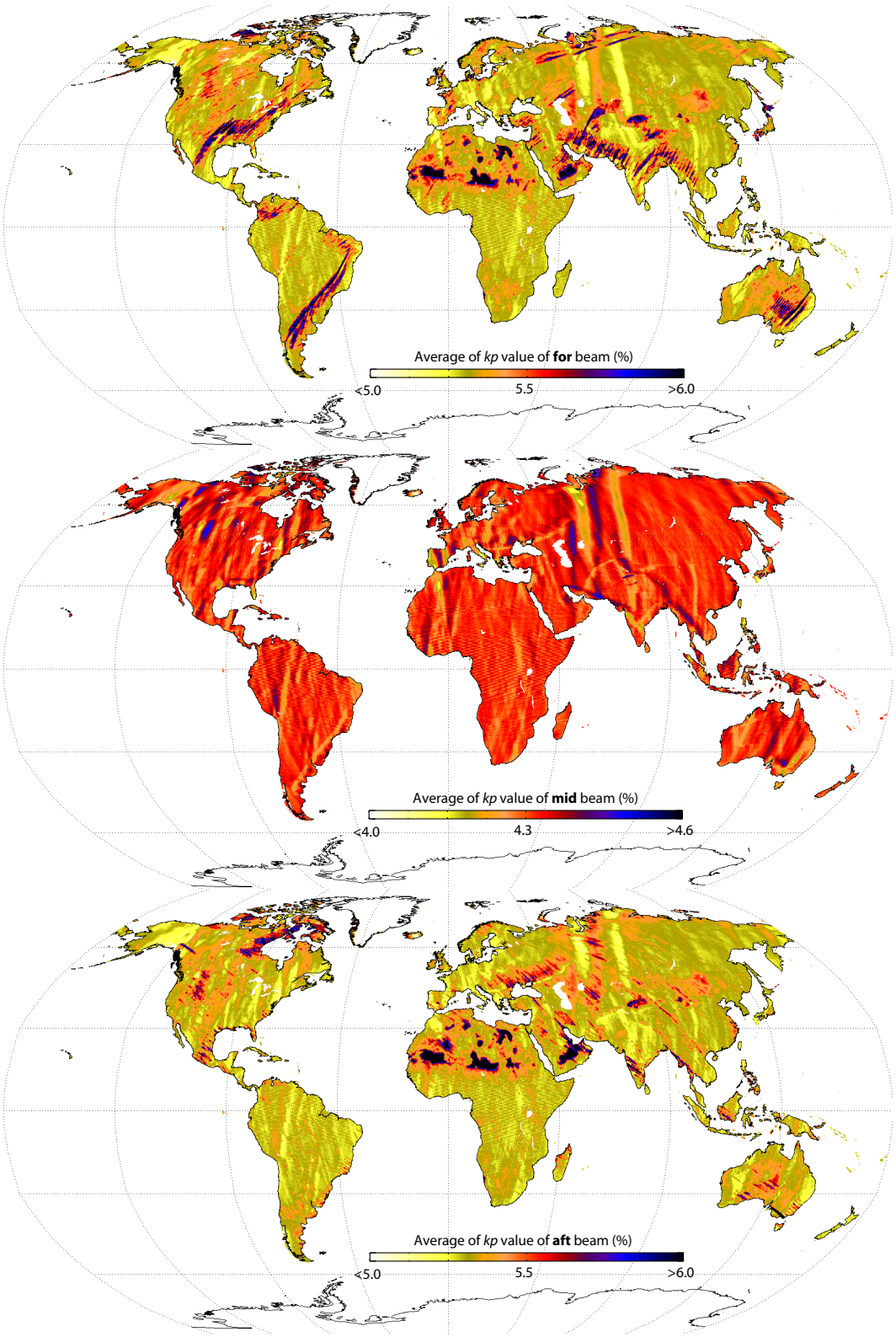

Figure 5-1. SCAT *kp* values averaged over three month of the year 1996.

5.2. Azimuthal Anisotropy of Backscatter

The intensity of the backscatter from rough surfaces depends on azimuthal look direction. Two of three side looking antennas of AMI-SCAT (the same is valid for ASCAT having two sets of triplet-antennas on each side of the satellite track) look at the surface with the same incidence angle but from two different azimuth angles. Discrepancy between fore and aft backscattering coefficients indicates azimuthal dependency plus the noise level of the individual σ^0 measurements (Early and Long 1997).

$$\delta = \sigma^0_{fore} - \sigma^0_{aft} \ , \tag{5-2}$$

where σ^0_{fore} and σ^0_{aft} denote for fore and aft beam antenna measurements. δ reflects the geophysical noise due to the surface anisotropy together with the noise of independent measurements and also include other types of error like speckle and geolocation errors (Figure 5-2). Geolocation errors may occur because the fore and aft beam antennas do not illuminate exactly the same area because of different antenna patterns on the ground.

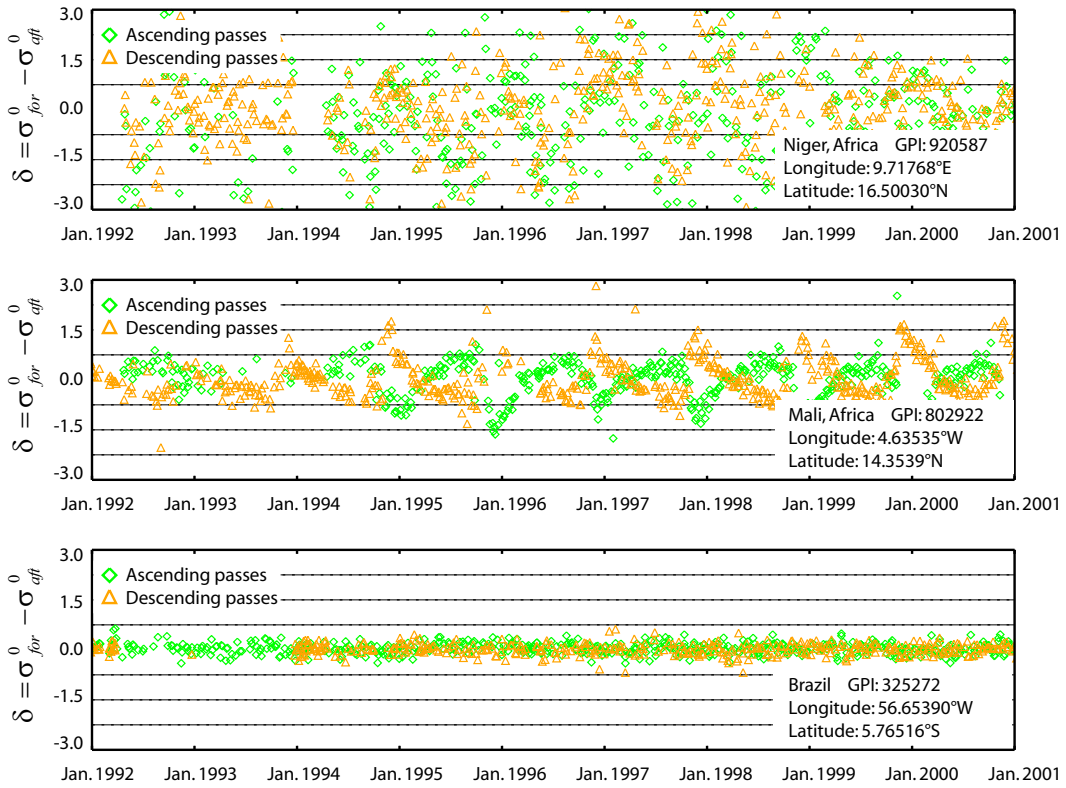

Figure 5-2. Illustration of the δ time series calculated for three different grid points.

5.2.1. Spatial Correlation of the Backscatter Measurements

Spatially independent data show the same variability regardless of the location of data points. However, spatial data in most cases are not spatially independent. Data values, which are spatially close together show less variability than data values which are farther away from each other. Existing spatial correlation in a dataset characterizes the spatial continuity or roughness of a dataset. In case of existing spatial correlation, the estimated variance could be an underestimation of the true error of measurements. This should be considered when estimating parameters and related errors in a spatially distributed dataset.

The oversampled scatterometer data are spatially distributed within the search area of each DGG point. The presence of spatial autocorrelation in δ values in equation 5-2 may violate the assumption of independency among samples. Figure 5-3-a and 5-3-b show δ values of several ascending passes within the sampling area of two different DGG points. Equation 5-3 known as the semivariogram equation is used to assess the existence of spatial correlation between δ values.

$$\zeta = \frac{1}{2n}\sum\left[\delta(x)-\delta(x+h)\right]^2 \quad , \tag{5-3}$$

where h is the distance between two paired samples, x and $x+h$ denote the positions of two sample pairs and n is the number of pairs.

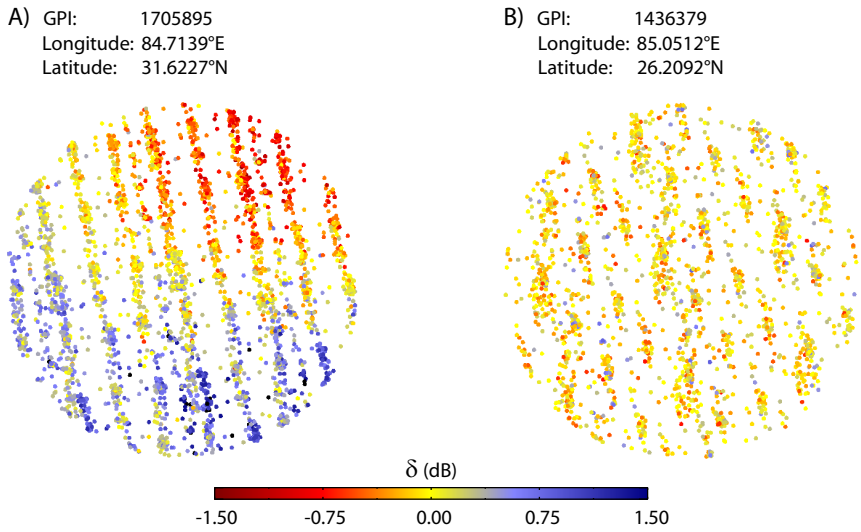

Figure 5-3. δ measurements within the search area of two different grid points

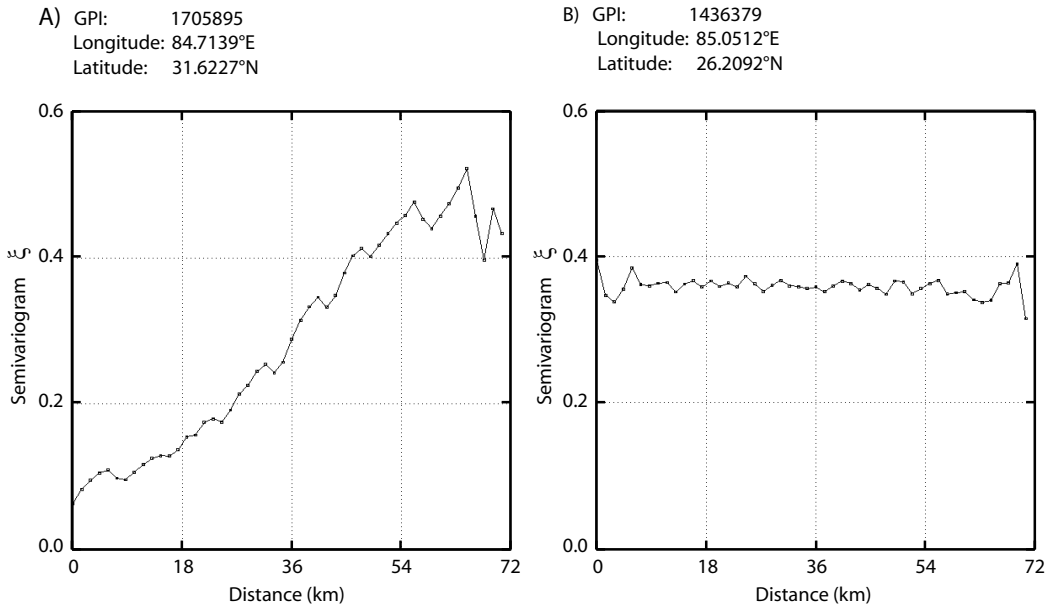

Figure 5-4. Variogramms of the grid points in figure 5-3.

The semivariogram in Figure 5-4-a indicates a strong spatial correlation between δ values. The samples which are spatially close together show less variability than those which are far away from each other. Conversely, the samples in Figure 5-4-b show almost equal variations in all distances. Spatial correlation might be due to a certain pattern on the surface or definitely an oversampling of the measurements in neighboring nodes during the processing chain of the backscattering signal. To examine the last assumption, an autocorrelation procedure was performed between SCAT measurements over the rainforests. Rainforest acts almost like an isotropic surface for scatterometer backscattering. It behaves as a volume scatterer over a wide range of incidence angles. The transmitted signal is equally scattered in all directions. Most of the scattered radiation of the incident radar is from the crown area and tend to have a slow incidence angle θ_{inc} variation which can be characterized by the following equation (Hawkins et al. 1999):

$$\gamma = \text{constant} = \sigma^0 / \cos\theta_{inc} \qquad (5\text{-}4)$$

The signal processing of SCAT measurements are done in frames of 19×19 nodes. Any oversampling of measurements is detectable by performing autocorrelation test for the measurements in a frame. The results of autocorrelation between γ values in a frame do not show any significant correlation between the measurements (Figure 5-5-a). However in

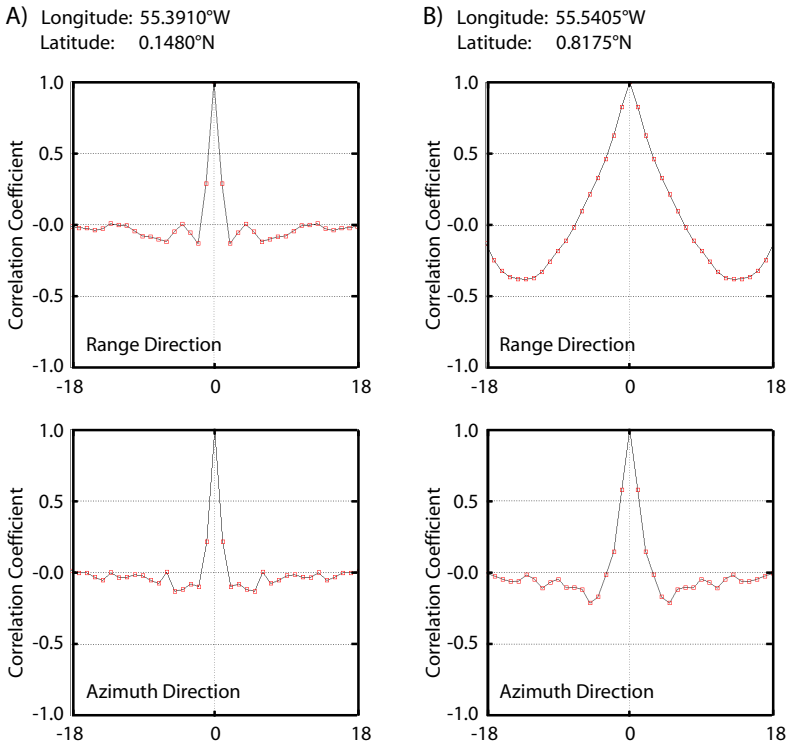

Figure 5-5. Autocorrelation between measurements in two different frames of SCAT measurements.

some cases, γ measurements reveal slight correlation along range direction (Figure 5-5-b). But this type of correlation is due to natural geophysical correlation between γ values and not because of oversampling. As another example of existing natural correlation between γ values is the strong correlation found between local precipitation over tropical rainforest in Guyana and the backscattered signal (Woodhouse et al. 1999). Even over the rainforests the γ values do not always remain constant.

The microwave dielectric constant of dry vegetative matter is much smaller than the dielectric constant of water. Since a vegetation canopy is usually composed of more than 99% air by volume, the canopy can be modeled as a water cloud whose droplets are held in place by the vegetative matter. Therefore the backscattering coefficient is a function of: volumetric moisture content of the soil, volumetric water content of the vegetation, and plant height (Attema and Ulaby 1978). In case of precipitation over a dense vegetative area, the number of water droplets located on the vegetation canopy increases which this consequently intensifies the backscattering of the canopy. Annual variations in γ measurements were also observed by Hawkins *et al.* (1999) in ERS-2 scatterometer data,

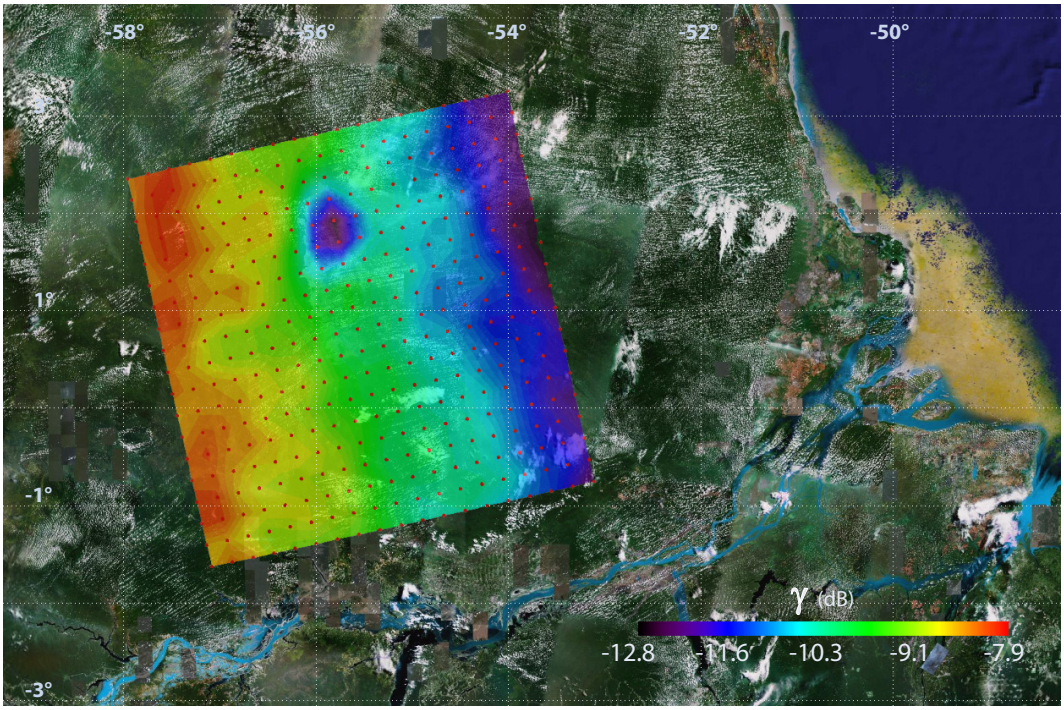

Figure 5-6. Variation of gamma values illustrated in a SCAT frame over rainforest.

which were thought to be geophysical in nature. Hence we can conclude that the spatial correlation observed in SCAT measurements is not related to oversampling of the measurements in neighboring nodes, but occurs due to geophysical phenomena. Furthermore the spatial correlation, which was monitored in δ measurements in a number of DGG resampling areas, is cause by certain natural features like lakes, sand-dunes, or mountains. As a result, the effect of spatial correlation of scatterometer measurements if any is negligible in noise calculations.

5.2.2. Estimated Standard Deviation of Backscatter

In TU-Wien model, the variation of σ^0 with respect to azimuthal angle is neglected and therefore the azimuthal anisotropy of backscatter is considered as noise. If a large number of backscattering pairs (fore and aft beam) are available, then the average of δ is an indication of surface anisotropy. Since both fore and aft beams have equal incidence angles then for an isotropic medium $\delta = 0$. To estimate the azimuthal noise of backscatter signal σ^0, an inverse error propagation is applied to (5-2). In other words, we measure uncertainties in the dependent variable δ, which is carried over the uncertainties in the independent variables σ^0_{fore} and σ^0_{aft}, to estimate the noise of σ^0.

The following approximation known as the error propagation equation introduced in chapter 1, is used for $\delta(\sigma^0_{fore}, \sigma^0_{aft})$ measurements.

$$\begin{aligned} \mathrm{var}(\delta) \approx \mathrm{var}\left(\sigma^0_{for}\right)\left(\frac{\partial\delta}{\partial\sigma^0_{fore}}\right)^2 + \mathrm{var}\left(\sigma^0_{aft}\right)\left(\frac{\partial\delta}{\partial\sigma^0_{aft}}\right)^2 + \\ .... + 2\times\mathrm{covar}\left(\sigma^0_{fore}, \sigma^0_{aft}\right)\left(\frac{\partial\delta}{\partial\sigma^0_{fore}}\right)\left(\frac{\partial\delta}{\partial\sigma^0_{aft}}\right) + ... \end{aligned} \tag{5-5}$$

In general, the first two terms dominate the uncertainties. The third term is the average of the cross terms involving products of deviations in σ^0_{fore} and σ^0_{aft} expressed as the covariance of fore and aft beam backscatter measurements, weighted by the product of the partial derivatives. On average, we should expect the third term to vanish in the limit of a large random selection of observation since σ^0_{fore} and σ^0_{aft} are independent measurements and uncorrelated, exclusive of soil moisture variations. Equation 5-5 reduces to 5-6 considering that all three scatterometer beams have the same noise level:

$$\mathrm{var}(\delta) = 2\,\mathrm{var}\left(\sigma^o\right) \tag{5-6}$$

Subsequently, the estimated standard deviation of σ^0 is formulated as the standard deviation of δ divided by the square root of 2:

$$ESD(\sigma^0) = \frac{StDev(\delta)}{\sqrt{2}}\ , \tag{5-7}$$

where $StDev(\delta)$ is the standard deviation of δ. This is an estimate of the real standard deviation of the backscatter signal. We call it Estimated Standard Deviation (ESD) of backscatter or azimuthal noise because the fore and aft beam antennas illuminate one point on the earth's surface only from two specific azimuth angles from 360°. But in practice we approach this assumption using multi-year data including both ascending and descending passes. Figure 5-7 indicates ESD values calculated globally using long-term ERS-1 and ERS-2 scatterometer measurements.

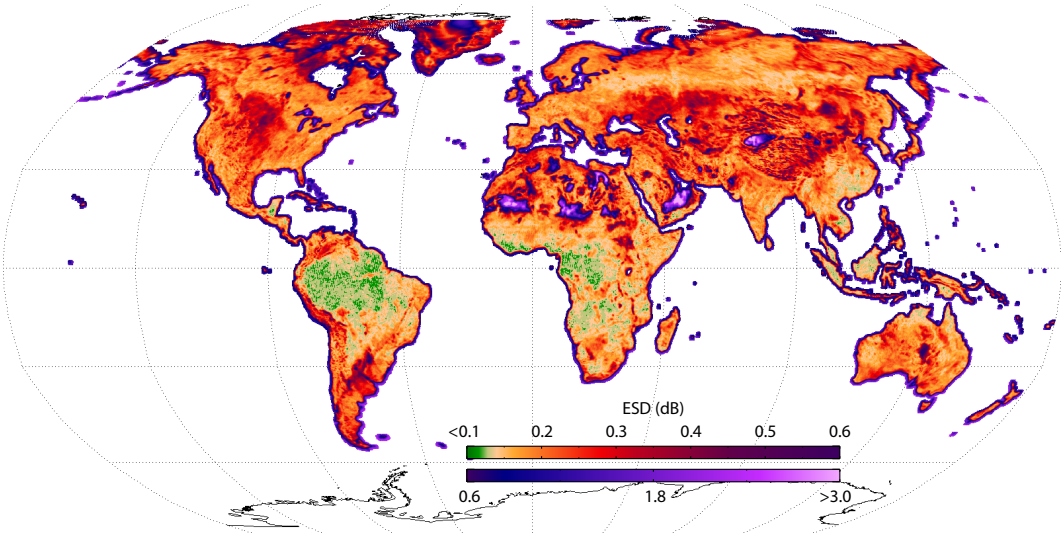

Figure 5-7. Global distribution of ESD.

5.3. Azimuthal Error Sources

Azimuthal noise is basically composed of 1) systematic errors like instrument noise and speckle; 2) and geophysical error depending on the land surface anisotropy. It is informative to know the extend of their influence on *ESD*, although in TU-Wien model any kind of azimuthal discrepancy in backscatter disregarding of its origin is considered as noise.

5.3.1. Instrumental Noise

One solution for measuring instrument noise is measuring backscattering coefficients over the rainforests. Rainforest in microwave radiations at X, C, and L-band behave as a volume scatterer over a wide range of incidence angles. The transmitted signal is equally scattered in all directions. Hence the Amazon rainforest has been chosen as the reference natural target in some Earth Observation missions like ERS-1, ERS-2, JERS-1, and RADARSAT (Crapolicchio and Lecomte 2003). The azimuthal noise over rainforest areas can be approximated as the noise of instrument. The instrument noise has random behavior with a Gaussian distribution and is independent of geophysical characteristics of the surface. The frequency distribution of *ESD* values of a selected DGG points over a dense vegetated area in Amazon rainforest shown in figure 5-8, indicates that the normality of *ESD* distribution is preserved for the DGG points with $ESD \le 0.14\,dB$ .Beyond this value the geophysical error influence the *ESD*. The average of the *ESD* values of the selected DGG points can be an approximation of instrument noise, which is about $\xi_{instrument} \approx 0.13\,dB$.

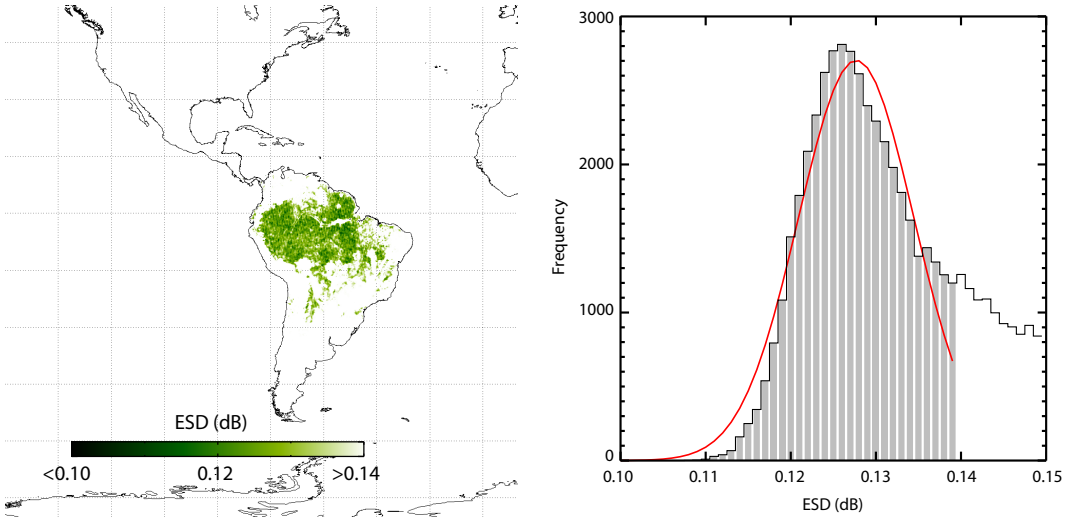

Figure 5-8. Instrumental noise. The average value of ESD over Amazon rain forest.

5.3.2. Influence of Land Cover on the Azimuthal Noise

The structural properties of the surface and the three dimensional architecture of vegetation have a clear influence on the azimuthal noise. However, because of the large footprint size of scatterometer sensor, the impact of land cover on the azimuthal noise is not obvious in areas that are characterized by a mixture of different classes of land cover. To asses the influence of the surface characteristics on the azimuthal noise, three global datasets are used in the study: 1) 1-km resolution Global Land Cover Classification Data (GLCC) in 25 classes, which is generated by using AVHRR NDVI composites as core dataset and other auxiliary datasets like Digital Elevation Model (DEM) and Ecoregions data (USGS 1999) (Figure 5-9), 2) 30-second resolution Global Lakes and Wetlands Database (GLWD) in 14 classes (Lehner and Doell 2004) (Figure 5-10), 3) 30-second resolution Global Digital Elevation Data (GTOPO30) (USGS 1996) (Figure 5-11). GLCC and GLWD datasets were resampled to the WARP5 DGG using the Hamming function (equation 4-1). The radius of the chosen window function corresponds to the spatial resolution of the SCAT. As a result, the percentage occupied by each class within the sampling area of each DGG point was obtained separately for GLCC and GLWD datasets by summing up the percentage area belonging to each class. GTOPO30 data were also resampled to DGG using the same window function. The standard deviation of heights within the sampling area calculated with respect to the weights assigned by interpolation procedure to the points. At last data are globally normalized with respect to the lowest and highest values. Figure 5-12 shows the global average and standard deviations of ESD calculated separately for different land cover classes for the grid points that have more than 80% coverage of a certain class.

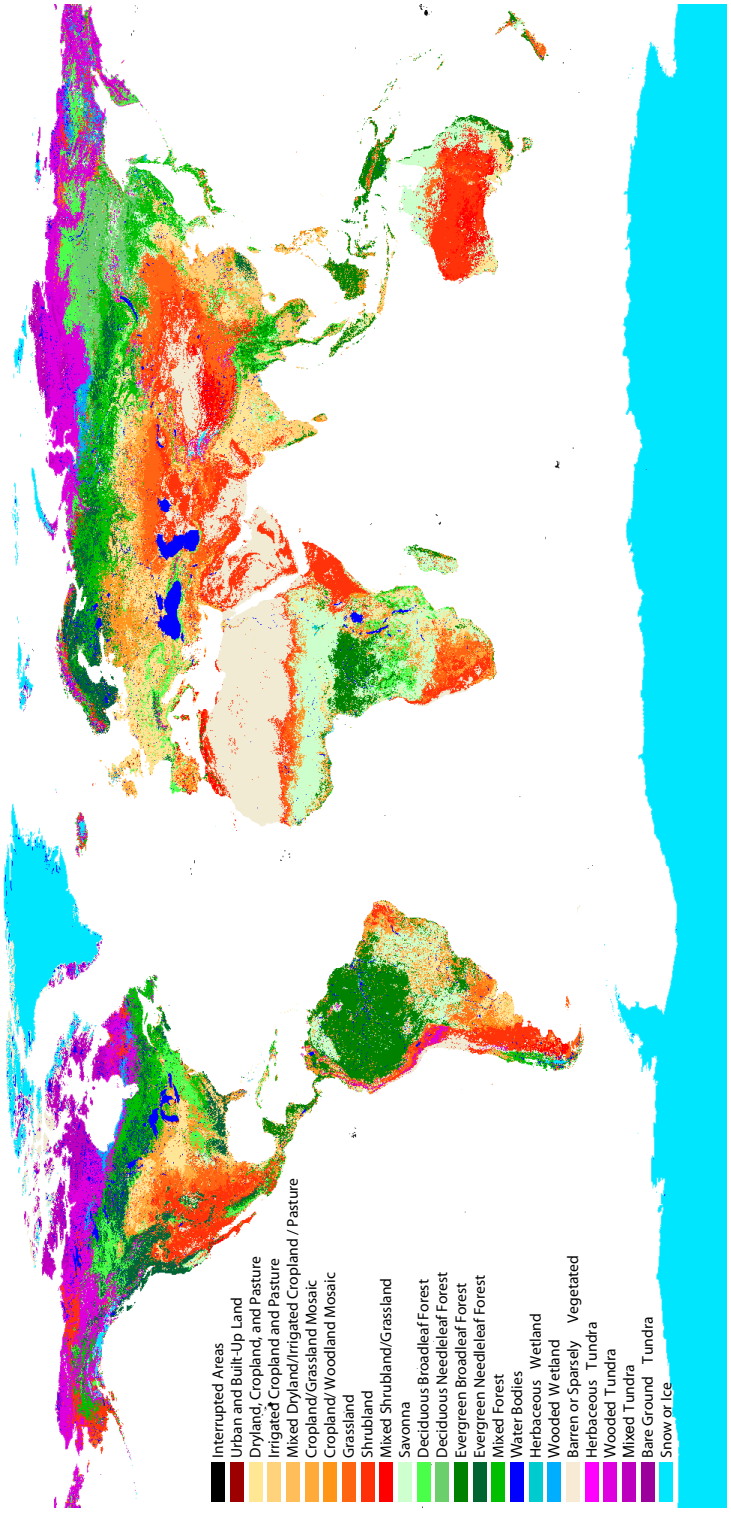

Figure 5-9. 1-kilometer resolution Global Land Cover Classification Data (GLCC).

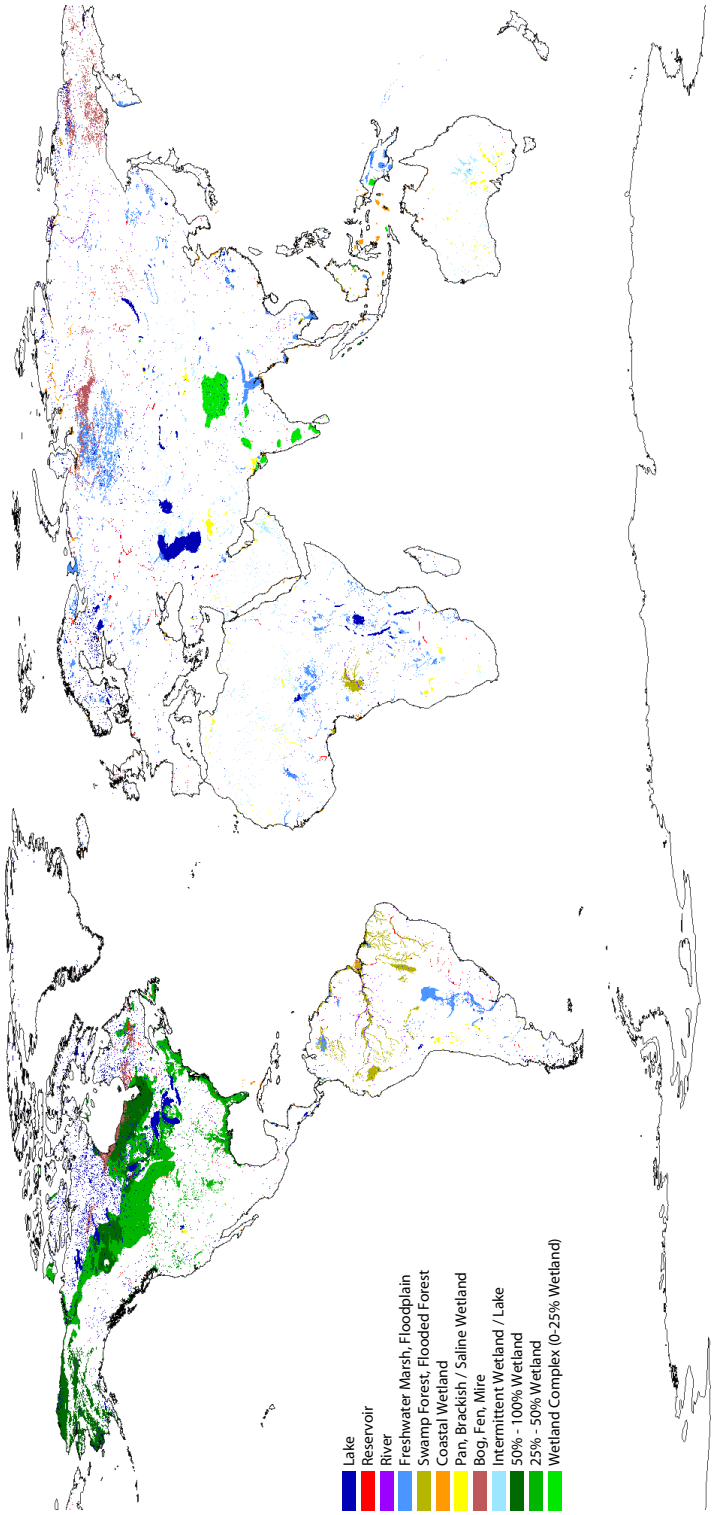

Figure 5-10. 30-second resolution Global Lakes and Wetlands Database (GLWD).

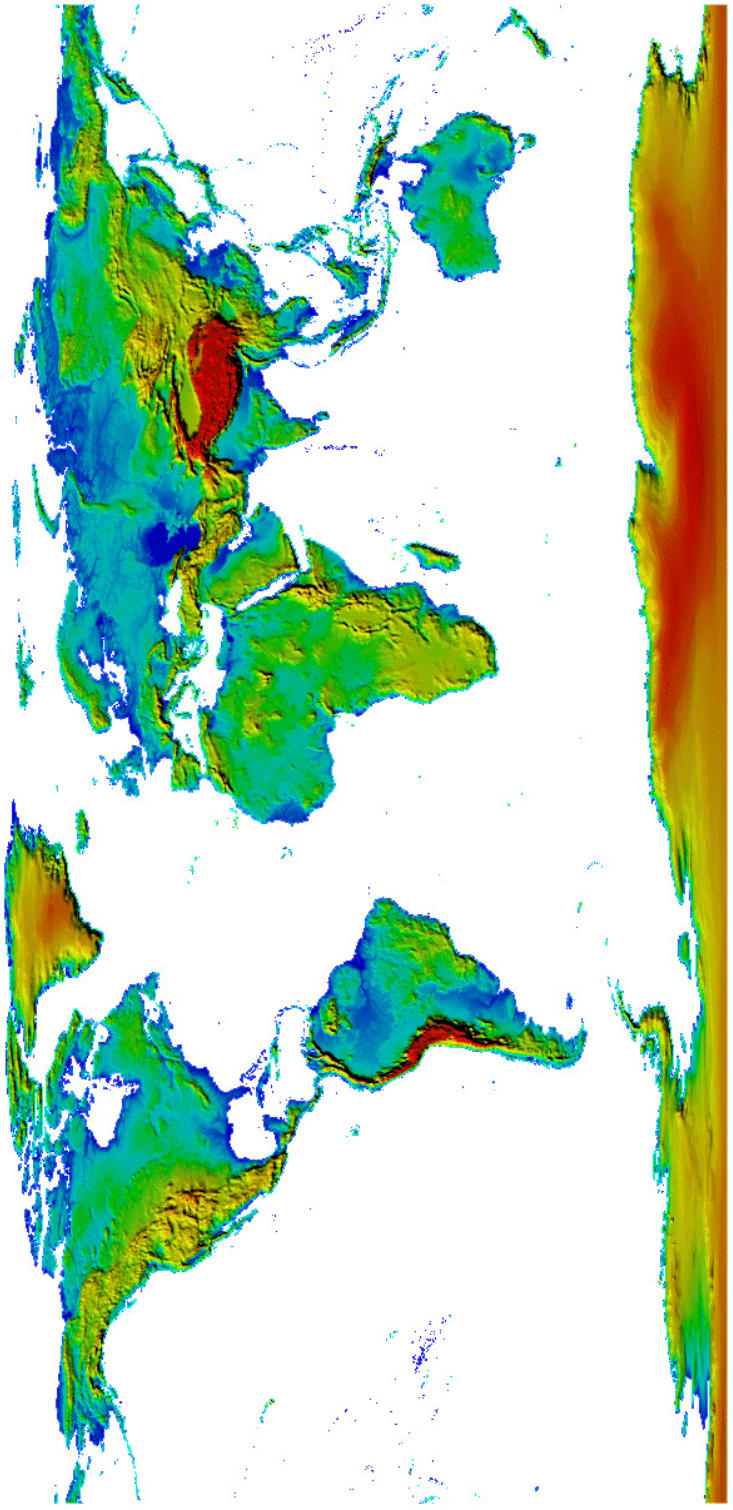

Figure 5-11. 30-second resolution Global Digital Elevation Data (GTOPO30).

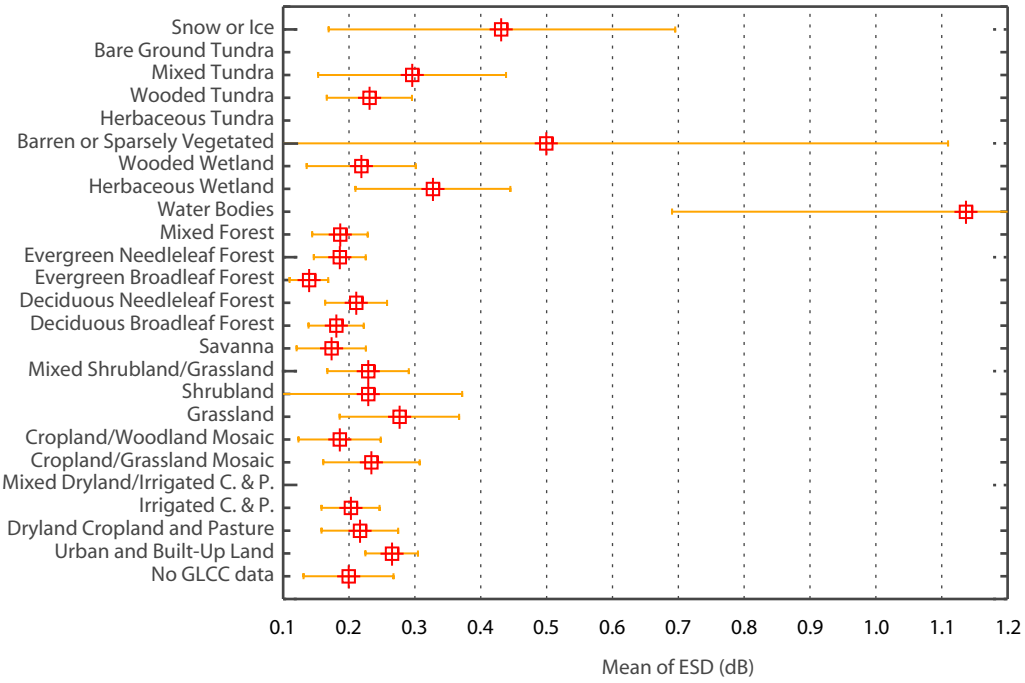

Figure 5-12. ESD values averaged for different land cover classes.

As it mentioned above, the azimuthal behavior of the target to the radar signal depends on the structure and the extent of surface isotropy. The most significant land cover types or factors, which have influence on the azimuthal noise, are as following.

Water

Backscattering from water depends on the roughness of the water surface. When the water surface is calm then specular reflection occurs and σ^0 is very low. Opposite, wind generates water waves spread out across the surface that increase scattering in backward direction. The difference between fore and aft beam backscatter is maximum when the radar looks into the upwind or downwind direction. The main contributions do not come from large waves, even if they are many meters height. Rather, scattering is dominated by little water ripples on the surface (Ulaby et al. 1982). Figure 5-13 shows values over the Great Lakes in northern America. In addition to the large water reservoirs, shallow bodies of water like swamps, marshes, estuaries, rivers and any set of small bodies of water cause different backscattering in fore and aft direction (figure 5-14). The range of ESD depends on the extend of the water body in comparison with spatial resolution of scatterometer and the roughness of water surface, which is related to the water flow and wind strength. Figure 5-15 shows ESD values over an area in Bangladesh encompassing many small ponds

and rice farms. The area is also categorized as flood plain. Large and spread out rivers like the Amazon river have also a significant influence on ESD values, although the land cover of river-side plays an important role in total backscattering (Figure 5-16).

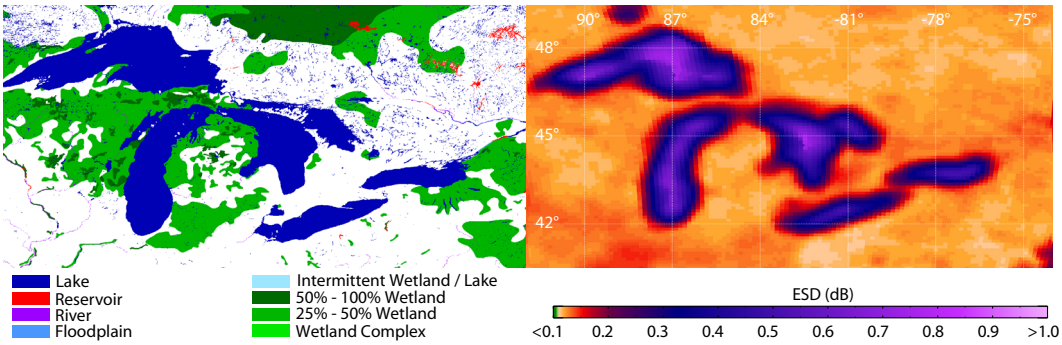

Figure 5-13. ESD values over Great Lakes, northern America.

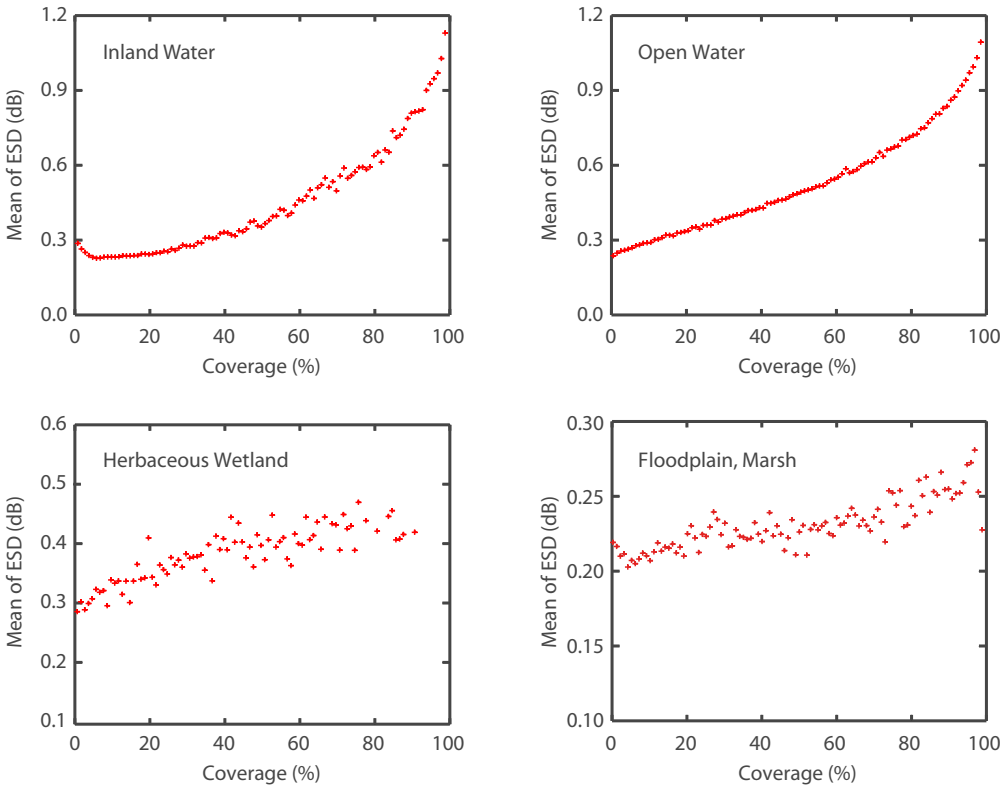

Figure 5-14. Mean of ESD versus the coverage of water bodies.

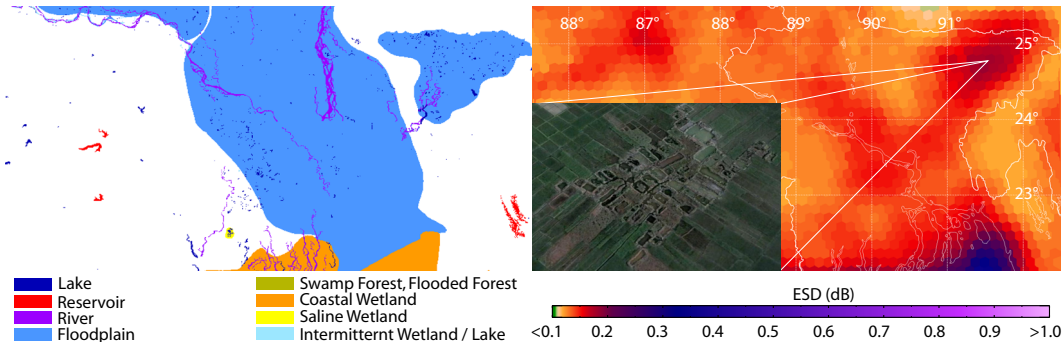

Figure 5-15. Bangladesh, ESD values in flooding areas.

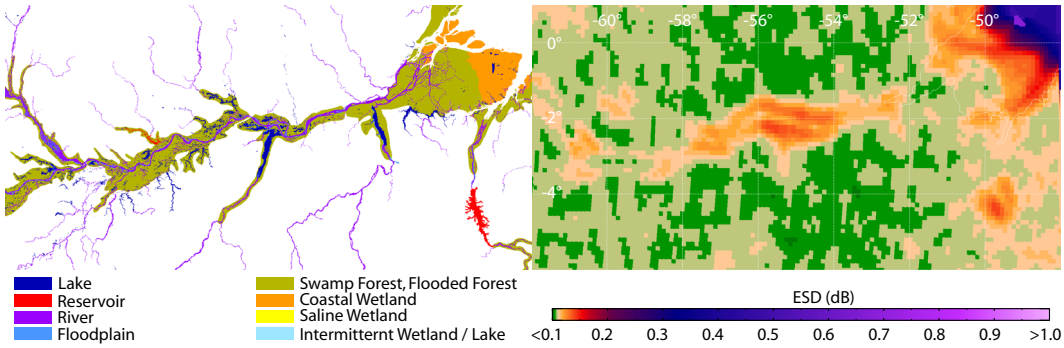

Figure 5-16. Brazil, ESD values of Amazon river.

Desert-Sand Dunes

The same anisotropy like the one found over the open water is also observable over sand desert areas. Wind erosion in large sand covered areas is similar in many ways to how wind interacts with the ocean surface, how water transports sediments on a river bed or how snow drifts (Bagnold 1941). However, asymmetric backscatter response of the sand areas is more complicated. The interaction of microwaves with such sand features may happen not only on the surface layer but also in the deeper layers in form of volume scattering. The penetration of microwave in soil relates inversely to soil wetness condition. At the beginning of the raining season, the backscatter from sand layers may decrease slightly as surface scattering is become stronger than volume scattering and thereafter with increasing moisture amount the backscatter regularly increases. Moreover the azimuthal response is sensitive to the orientation of small-scale (millimeters to meters) wind induced sand ripples, rather than the larger scale dune orientation (Bateson and Woodhouse 2004). Figure 5-17 shows ESD values over the Taklamakan sand desert in Central Asia.

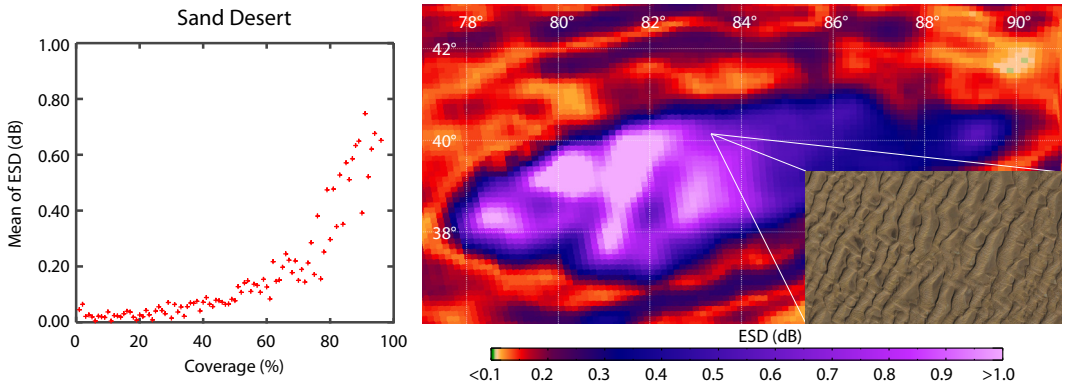

Figure 5-17. Taklamakan desert, Central Asia, ESD values in sand desert areas.

Urban and Built-Up Land

Because of so-called corner reflectors effect, the backscattering coefficient from urban areas is in general higher than from their surroundings. Azimuthal noise is also higher due to multiple reflections, which take place depending on the scatterometer antenna look direction. Figure 5-18 indicates the response of azimuthal noise over Paris and neighborhoods with increasing density of built-up areas.

Dense Vegetation

In general, backscatter from land surfaces covered by vegetation is governed by the scattering properties of the geometrical elements that can be considered to be made up by vegetation, soil surface and the interaction between the vegetation volume and soil surface in the form of multiple scattering:

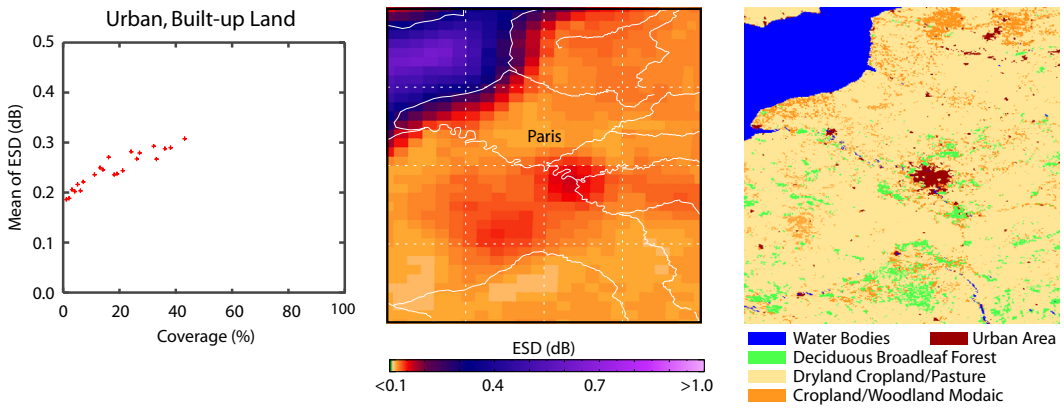

Figure 5-18. ESD values measured in urban areas.

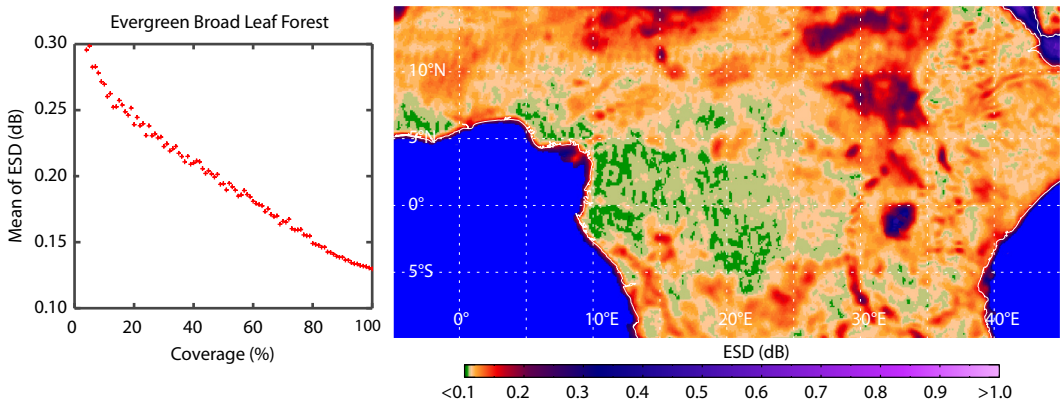

Figure 5-19. ESD values of rain forest.

$$\sigma^0 = (1-C)\sigma^0_{bare\ soil} + C \cdot \sigma^0_{Canopy} + (1-C)^0_{int} \tag{5-8}$$

where C is the fraction of the illuminated area that is vegetation-covered, $\sigma^0_{baresoil}$ is the backscattering coefficient of exposed surface, σ^0_{canopy} is the backscattering coefficient of canopy, and σ^0_{int} is an interaction component accounting for multiple reflections as in a corner reflector (Ulaby et al. 1986).

The azimuthal noise of backscatter from such surfaces firstly depends on the fraction of area that is vegetation-covered and secondly on the quantity of biomass as well as three-dimensional architecture of the vegetation (size, shape, and orientation of trunks, branches, and foliage). The minimum value of ESD is observable in surfaces covered by dense vegetation wherein volume scattering is dominant. Figure 5-19 shows the average values of ESD versus the coverage of evergreen broadleaf forest.

Topography

When the scatterometer beam reaches the base of a slant feature such as a mountainside tilted towards the satellite track, the local incidence angles of the fore and aft beams varies depending on the look angle of the scatterometer antennas and the slope of the mountainside. Maximum deviation of local incidence angle occurs when the satellite track is parallel to the slant surface. If the look direction becomes perpendicular to the orientation of surface feature, a large portion of incident energy will be reflected back to the sensor. The more oblique look direction in relation to the feature orientation, the less energy will be returned to the sensor. The look direction can significantly influence the azimuthal noise,

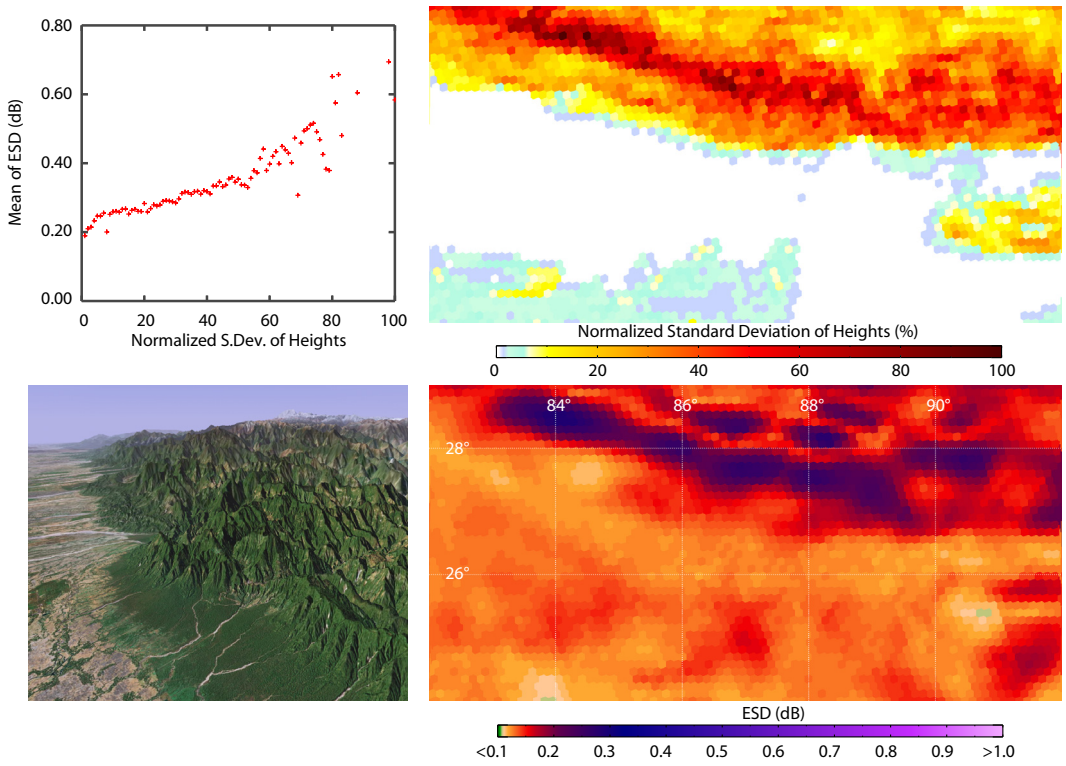

Figure 5-20. Azimuthal noise is higher in areas with complex topography.

particularly when ground features are arranged in a linear structure, such as mountain ranges. The higher azimuthal noise is observable in areas with complex topography, where the standard deviation of elevation is large. Figure 5-20 illustrates the effect of complex topography on azimuthal noise.

Snow Cover and Frozen Soil

At microwave frequencies, freezing of soil results in a strong decrease of the dielectric constant and consequently low backscatter. The backscatter of dry and frozen soils are similar, however in case of the presence of vegetation canopy the impact of freezing is more complex. Backscatter measurements are also sensitive to snow properties. Dry snow consists of frozen water as ice particles distributed in an air medium. The scattering behavior of snow depends on the dielectric properties of the ice particles and on their distribution and density. As freezing cause a strong drop off the dielectric constant of the medium, dry snow is more or less transparent at C-Band (Mätzler and Schanda 1984). Backscatter of dry snow is therefore strongly affected by reflections from the soil below the cover. A study of ERS Scatterometer data over the Canadian Prairies has shown that a dry

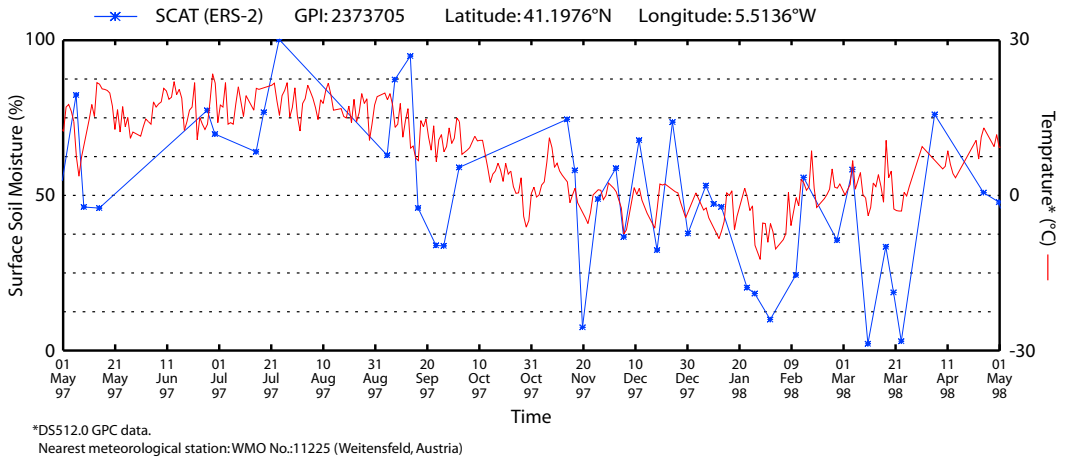

Figure 5-21. Soil moisture values decrease drastically when temperature drops below 0°C.

shallow snow pack overlying a soil is almost identical to the backscatter of the snow free situation (Wagner 1995). In the presence of liquid water dielectric constant of snow strongly increases resulting in a more complex backscatter behavior. The penetration depth for wet snow with a liquid water content of 2-4 vol. % is typically of the order of one wavelength (Mätzler and Schanda 1984). The dominating scattering mechanism is therefore surface scattering and the backscatter intensity depends on snow surface roughness. Figure 5-21 shows how a layer of snow adulterates the soil moisture estimate depending on the temperature. In this particular example, dry snow has low backscatter characteristics leading to low soil moisture estimates. During melting events backscatter increases leading to high soil moisture estimates. Unfortunately it is not possible from scatterometer data alone to detect the presence of snow or differentiate between backscatter of dry and frozen soil, although in high latitudes the begin and end of freeze/thaw periods are clearly observable in the time series of the azimuthal deviation of backscatter (figure 5-22). In conclusion, soil moisture cannot be retrieved under frozen or snow conditions and such observations should be carefully masked using external data.

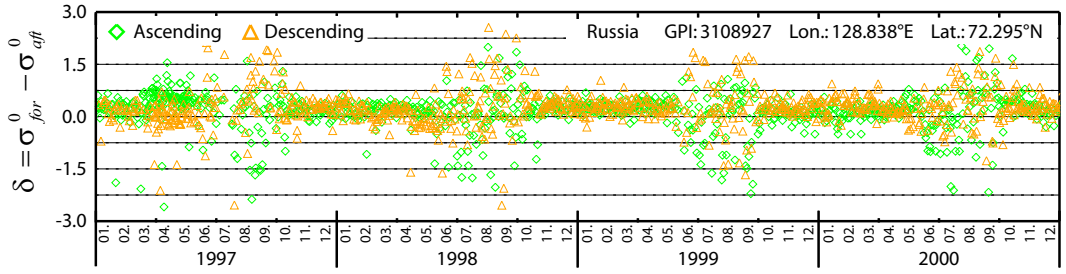

Figure 5-22. Freeze/thaw period is observable in the δ time series.

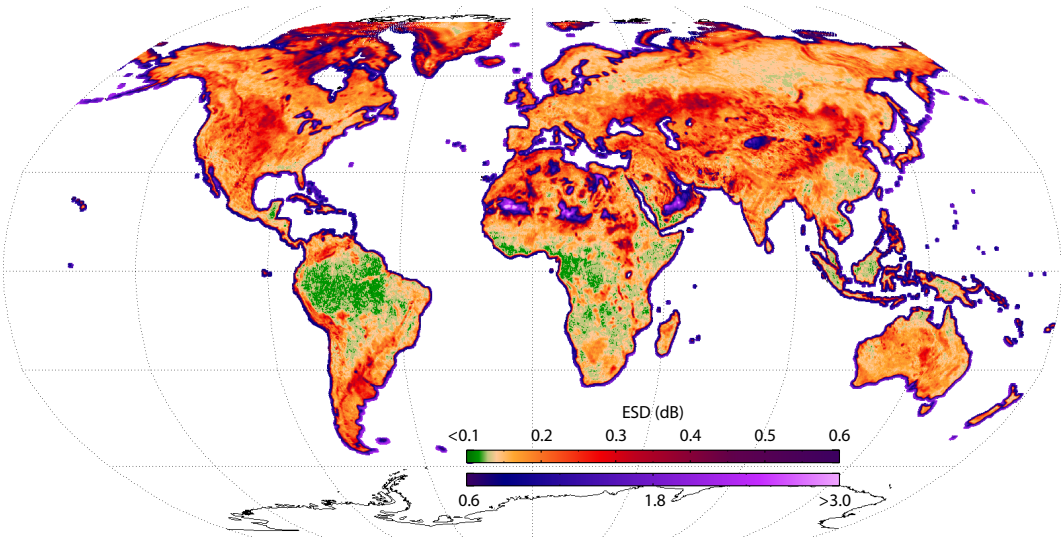

Figure 5-23. ESD after azimuthal correction.

5.4. Azimuthal Noise Correction

As it discussed in 5.2.2, the azimuthal anisotropy of backscatter is considered as noise. In the WARP5 processing algorithm, the azimuthal noise is reduced to some extent using an azimuthal anisotropy modification method (Bartalis et al. 2006). In this method triplet measurements of backscattering are split up to six groups of σ^0_{fore}, σ^0_{mid}, and σ^0_{aft} separately for ascending and descending passes plus a seventh group including the whole measurement time series. The backscattering measurements in each group are considered as a function of their incidence angles. After eliminating outliers, a second-order polynomial function is applied to measurements in each group. For each individual measurement, the difference between the function value of the relative group and the function value acquired from the whole backscattering measurements at the same incidence angle, is considered as a correction factor. Figure 5-23 shows ESD values after azimuthal correction. Frequency distributions of different versions of ESD are shown in figure 5-24.

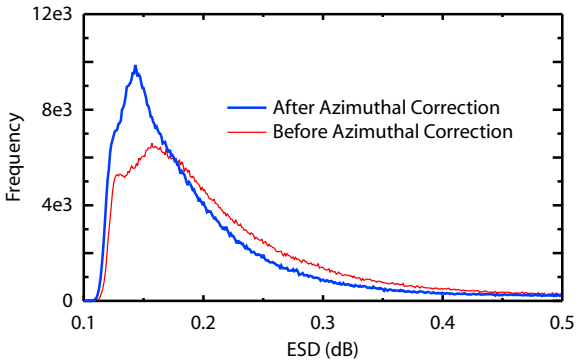

Figure 5-24. ESD frequency distribution before and after azimuthal correction.

6. Uncertainty Propagation

Uncertainty is a measure of the goodness of a result. The best method for assessing uncertainty in an experiment is through model validation, a process in which the model predictions are compared to the true measurements or numerous independent datasets. Unfortunately the exact model validation of the scatterometer derived soil moisture data is limited because of lack of in-situ measurements in regional and global scale. A feasible approach to perform a quantitative uncertainty analysis is using either analytical or numerical techniques to propagate uncertainties in the model's components to obtain an assessment of the uncertainty in the overall result. In order to build an uncertainty propagation approach we need to: 1) determine uncertainties of each individual terms in the model; 2) and develop a structured method to aggregate uncertainties into the final result.

6.1. Initialization of Error Propagation in WARP5

In WARP5, parallel to the soil moisture retrieval algorithm, an error analysis is carried out to determine the uncertainties associated with the measurements and the model's parameters. The error model is initialized with the azimuthal noise (ESD), which has been described in detail in the chapter 5. The azimuthal noise together with the uncertainties of the model's parameters in each processing step are propagated through the retrieval algorithm (figure 6-1). In the WARP5 uncertainty propagation procedure, a combined

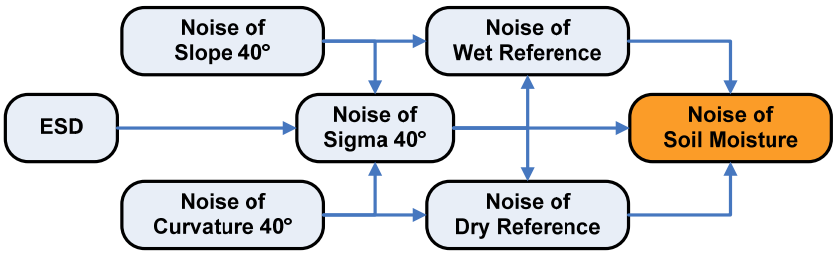

Figure 6-1. Major components of the WARP5 error propagation procedure.

analytical and numerical propagation approach is used. For relatively simple model equations, in which the knowledge of error sources is available, a variance propagation technique (equation 1-12) is performed and in situations where the variance propagation technique may not be practical or be more difficult to apply, a quasi-Monte Carlo uncertainty propagation is used.

The preliminary step in any error propagation method is identification of the uncertainties related to the model's parameters. The error sources in the TU-Wien soil moisture retrieval algorithm can be categorized as: 1) uncertainties linked to the data acquisition including backscatter noise, uncertainty of the gain parameters, geometry, and data resampling; 2) uncertainties associated with the geophysical model function. The input data of the WARP5 noise model are the uncertainties of the backscattering coefficient and incidence angle. These are propagated through the retrieval algorithm to calculate uncertainties associated with the model's parameters.

6.1.1. Noise of Backscatter

The azimuthal noise of backscatter (ESD) indicates anisotropic behavior of σ^0 measurements and represents the first component of the above mentioned uncertainties. It reflects the noise of independent measurements, which have Gaussian random behavior, in addition to the other possible errors like speckle and geolocation inaccuracy. Using ESD values in the error propagation procedure has the advantage of excluding backscattering variations due to the geophysical characteristics of the target since the variations of backscatter appear similarly in both fore and aft beams.

6.1.2. Incidence Angle Uncertainty

The uncertainty range of the incidence angle can be referred to the geometry calculation error of the scatterometer/satellite with respect to the ground surface. The target localization error is about 5km for ERS scatterometer (Attema 1991) and about 4.4 for ASCAT (Figa-Saldana et al. 2002). According to the equation 6-1 and figure 6-2, a 5km inaccuracy in localization corresponds to less than about 0.5° uncertainty of incidence angle measurements, which varies depending on incidence angle value.

$$\xi_\theta = \arctan\left(\frac{h \cdot \tan(\theta) + \Delta x}{h}\right) - \theta \qquad (6\text{-}1)$$

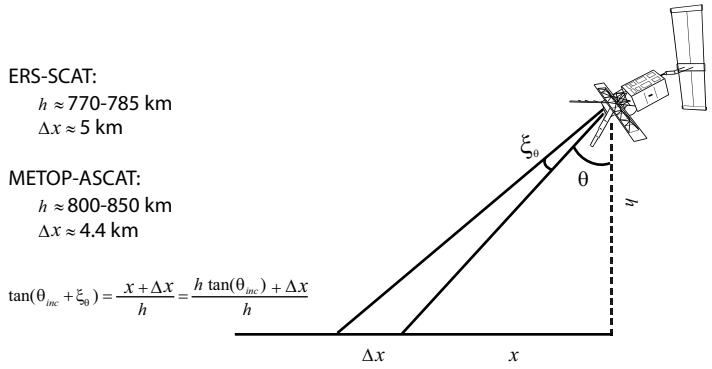

Figure 6-2. Uncertainty estimation of the incidence angle with respect to the nominal localization error.

6.2. Noise of Slope and Curvature

The slope and curvature parameters in the WARP5 algorithm are calculated using the Monte Carlo simulation method (equations 5-6 and 5-7). In MC simulation the model is fed with pseudo random inputs of paired backscatter measurements to calculate local slope values and consequently the slope and curvature at 40° incidence angle for a given day t and within a certain time window length τ (figure 6-3). In WARP model, it is assumed that the dependency of backscatter to the incidence angle does not change during this period. But in reality the duration of this period depends on biomass development rate and the time of year. For example with the beginning of the rainfall season, vegetation starts to develop and reaches to its maturity after a definite period, which relates to the climate and atmospheric forces. Similarly with the beginning of the dry season, biomass starts to decrease and after a

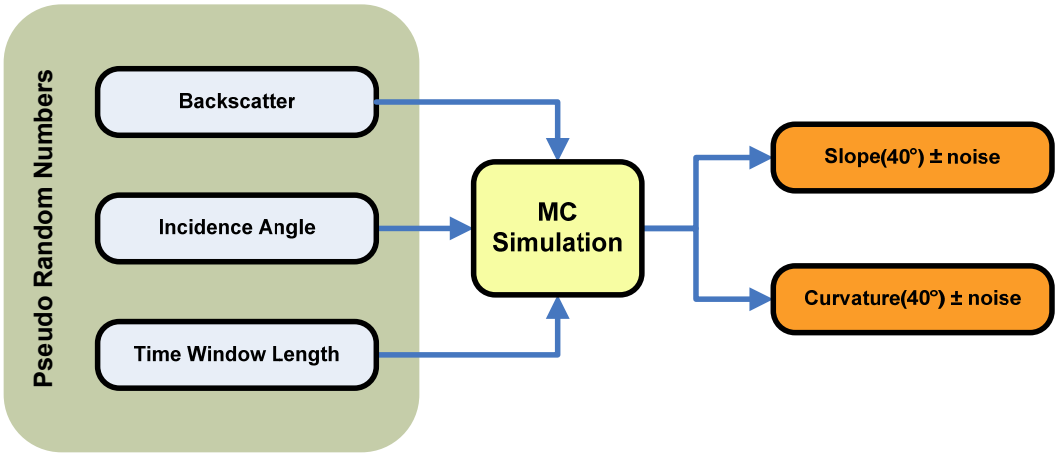

Figure 6-3. Calculation of the slope and curvature parameters and relative uncertainties.

certain period it reaches to its lowest amount. Estimating a unique period, in which vegetation is supposed to not alter, causes uncertainties in slope and curvature calculations. In addition, the duration of vegetation development differs from place to place. Changes in biomass amount can be happened within two weeks up to several weeks. Hence in each MC iteration, τ is set randomly from 14 days to 84 days. The input random values for each input parameter (triplet backscatter values and incidence angles) are sampled from the respective normal distribution with the mean equal to the real measurement and standard deviation equal to the noise of that parameter according to:

$$\rho(\theta_r) = \frac{1}{\xi_{\theta_i}\sqrt{2\pi}} e^{-(\theta_r-\theta_i)^2/2\xi_{\theta_i}^2} \tag{6-2}$$

$$\rho(\sigma_r) = \frac{1}{\xi_{\sigma_i}\sqrt{2\pi}} e^{-(\sigma_r-\sigma_i)^2/2\xi_{\sigma_i}^2} \tag{6-3}$$

where θ_r σ_r are random backscatter and incidence angle numbers, $\xi_{\theta_i} = 0.5$ and $\xi_{\sigma_i} = ESD$. The random numbers are generated separately for each triplet (fore, mid, aft).

After generating random numbers considering the equations 6-2 and 6-3 for each triplet, a large number of MC trials are performed. The result of simulation converges to $\sigma'(40,t)$ and $\sigma''(40,t)$ functions and consequently the relative uncertainties in calculation of slope and curvature at 40° are determined as follows:

$$\xi_{\sigma'_{40}}(t) = \sqrt{\frac{1}{M-1}\sum_{i=1}^{M-1}\left(\sigma'(40,\tau_i,t) - \sigma'(40,t)\right)} \tag{6-4}$$

$$\xi_{\sigma''_{40}}(t) = \sqrt{\frac{1}{M-1}\sum_{i=1}^{M-1}\left(\sigma''(40,\tau_i,t) - \sigma''(40,t)\right)} \tag{6-5}$$

where M is the number of MC trials, $\sigma'(40,t)$ and $\sigma''(40,t)$ are slope and curvature functions calculated using equations 4-6 and 4-7. $\xi_{\sigma'_{40}}(t)$ and $\xi_{\sigma''_{40}}(t)$ are resembling the standard deviations of $\sigma'(40,t)$ and $\sigma''(40,t)$ functions calculated for each day of year t.

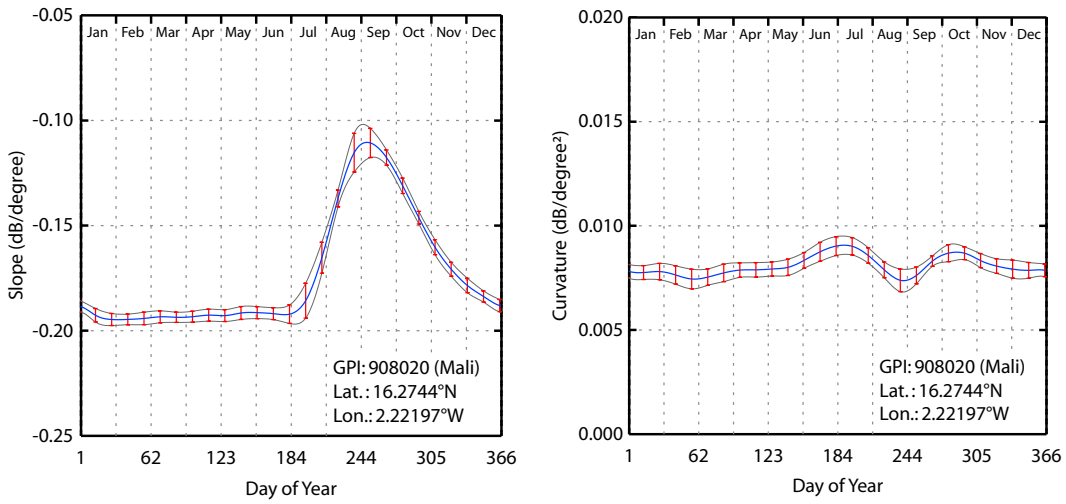

Figure 6-4. Mali, Africa, The slope and curvature functions and their respective uncertainty ranges.

Figure 6-4 indicates the outcome of MC simulation for a grid point located in Mali. The slope function has the highest uncertainties around July and August when the vegetation in this region starts to develop. The maximum slope is visible between August and September. During dry season both slope and curvature are almost consistent with the lowest uncertainty ranges. Contrary to figure 6-4, figure 6-5 shows another example from southern hemisphere, southern Australia, with the highest slope values around November and the lowest in June. Global plots of the min. and max. noise of the slope and curvature during the year are illustrated in figure 6-6 and 6-7. Figure 6-8 illustrates global plots showing the month of year when the slope and curvature functions have the highest uncertainty.

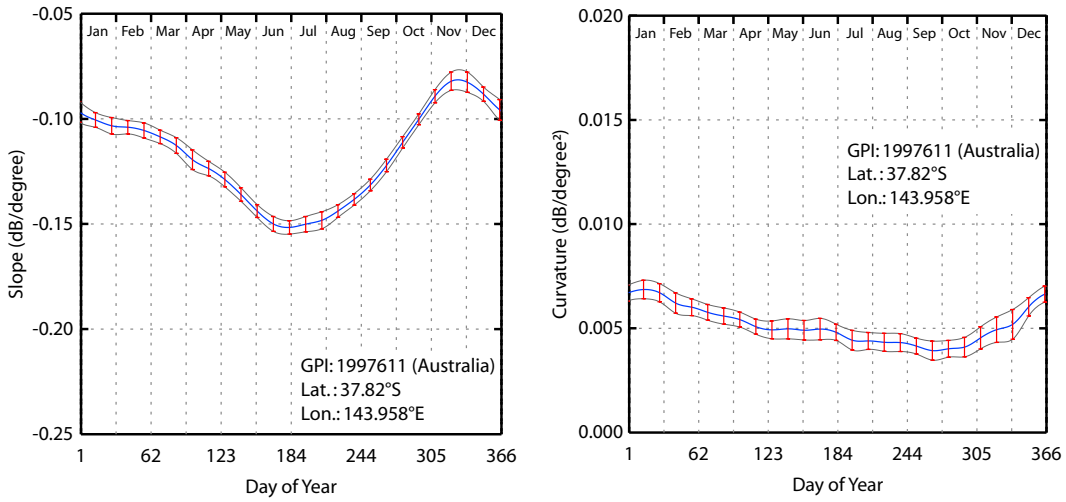

Figure 6-5. Victoria, Australia, the slope and curvature functions and their respective uncertainty ranges.

a)

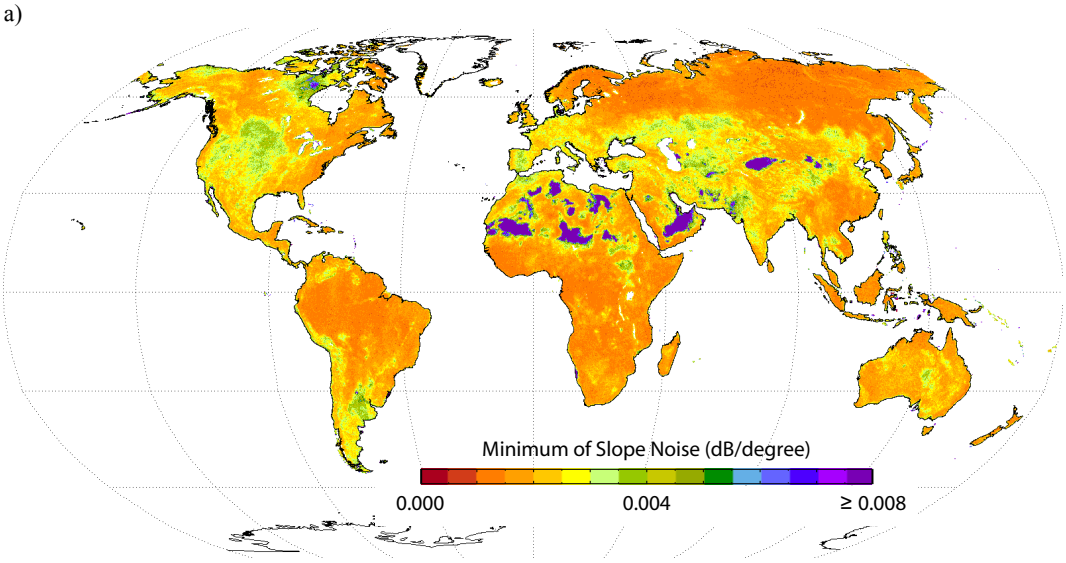

b)

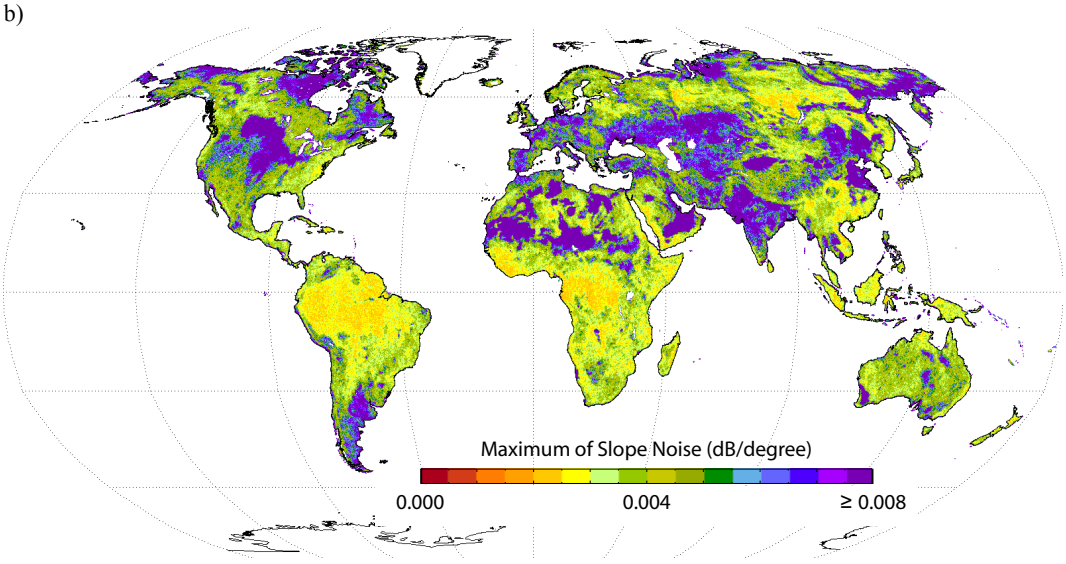

Figure 6-6. a) Minimum noise level of the slope function. b) Maximum noise level of the slope function.

a)

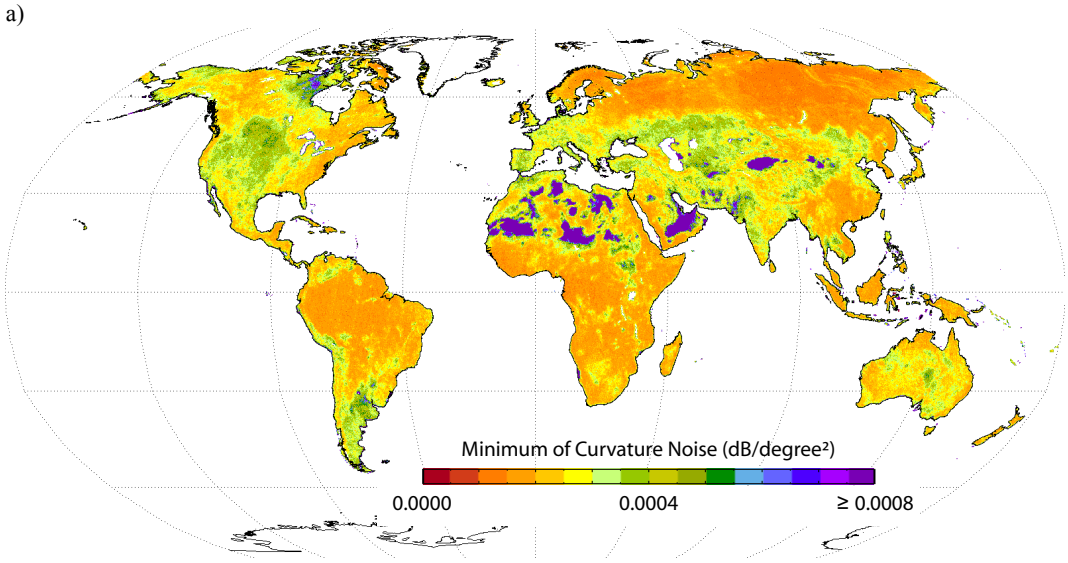

b)

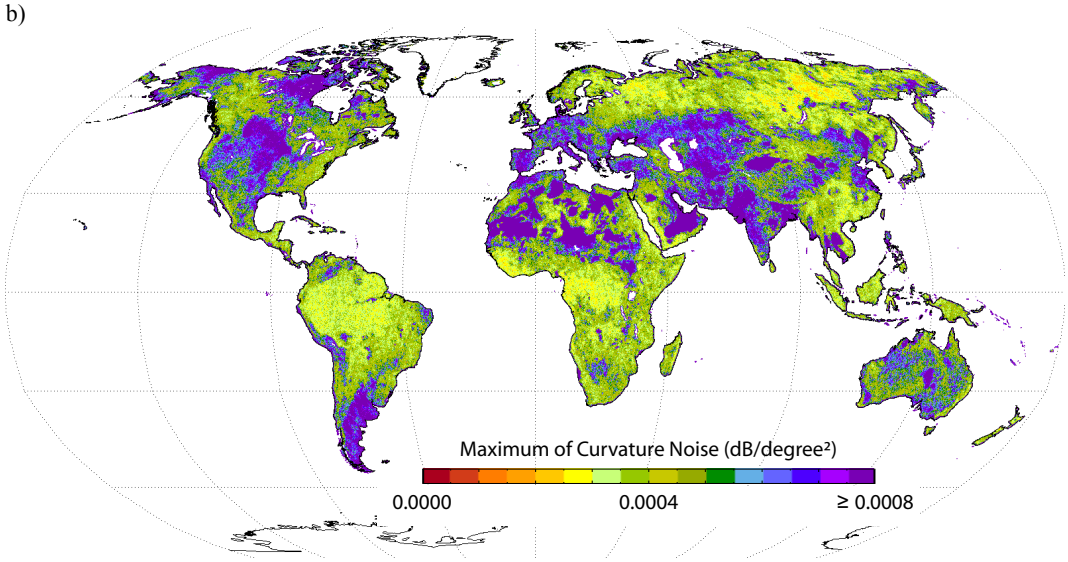

Figure 6-7. a) Minimum noise level of the curvature function. b) Maximum noise level of the curvature function.

a)

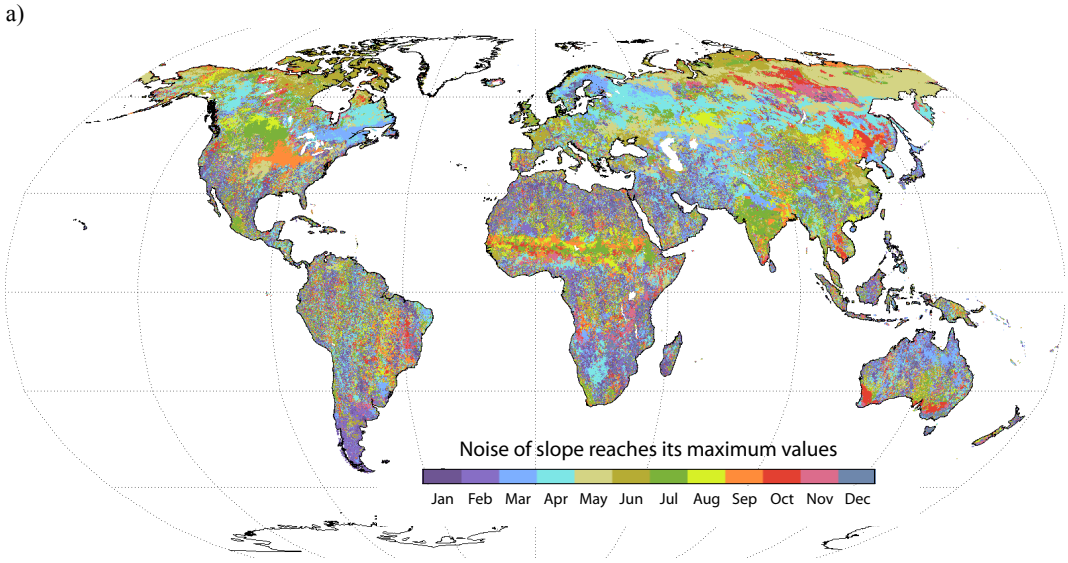

b)

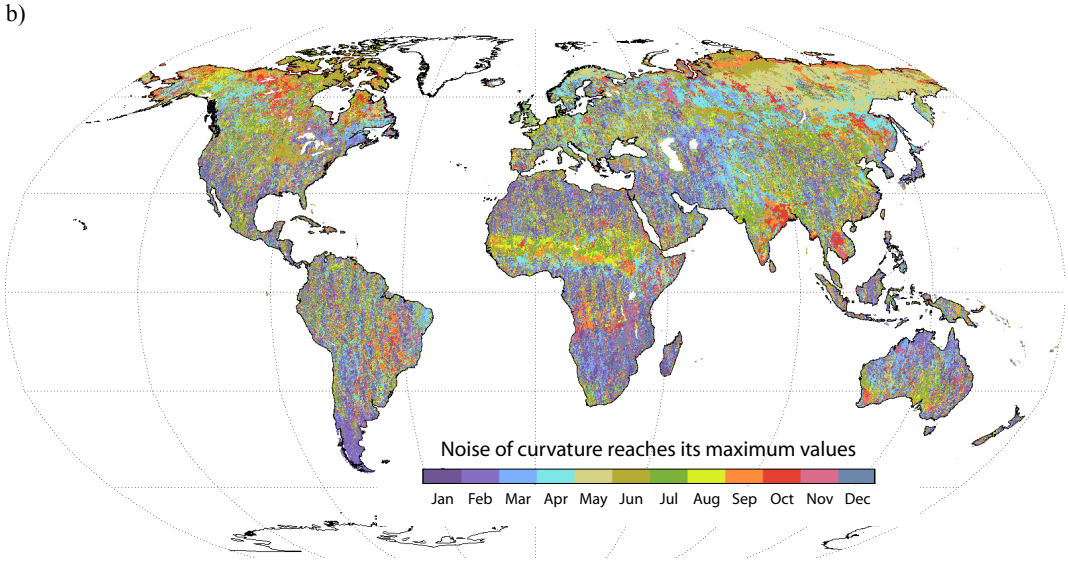

Figure 6-8. a) Time of year with the highest uncertainty in slope calculation. b) Time of year with the highest uncertainty in curvature calculation .

6.3. Noise of Normalized Backscatter

The error sources in $\sigma^0(40)$ calculation can be separated to the uncertainties related to the extrapolation procedure of the backscattering coefficients to the reference incidence angle and the uncertainties coming from the scatterometer observations like instrument noise, speckle, and azimuthal effects. The consequent noise of the backscatter normalized at 40° is estimated by applying the error propagation rules for the equation 4-8:

$$\xi_{\sigma(40)}(t) = \frac{1}{3}\sqrt{\sum_{i=1}^{3} \xi^2_{\sigma_i(40)}(t)} \tag{6-6}$$

where $\xi_{\sigma_i(40)}(t)$ is the noise of normalized backscatter of the *ith* beam.

Using the error propagation equation 1-12 for the equation 3-6 results the following derivation:

$$\begin{aligned}
\xi^2_{\sigma_i(40)} = ESD^2 &\left(\frac{\partial\sigma(40)}{\partial\sigma_i^0}\right)^2 + 2r_{\sigma^0\theta} \cdot ESD \cdot \xi_\theta \cdot \left(\frac{\partial\sigma(40)}{\partial\sigma_i^0}\right)\cdot\left(\frac{\partial\sigma(40)}{\partial\theta_i}\right) \\
&+ 2r_{\sigma^0\sigma'_{40}} \cdot ESD \cdot \xi_{\sigma'_{40}} \cdot \left(\frac{\partial\sigma(40)}{\partial\sigma_i^0}\right)\cdot\left(\frac{\partial\sigma(40)}{\partial\sigma'_{40}}\right) \\
&+ 2r_{\sigma^0\sigma''_{40}} \cdot ESD \cdot \xi_{\cdot\sigma''_{40}} \cdot \left(\frac{\partial\sigma(40)}{\partial\sigma_i^0}\right)\cdot\left(\frac{\partial\sigma(40)}{\partial\sigma''_{40}}\right) \\
+\xi^2_{\sigma'_{40}} &\cdot \left(\frac{\partial\sigma(40)}{\partial\sigma'_{40}}\right)^2 + 2r_{\sigma'_{40}\sigma''_{40}} \cdot \xi_{\sigma'_{40}} \cdot \xi_{\cdot\sigma''_{40}} \cdot \left(\frac{\partial\sigma(40)}{\partial\sigma'_{40}}\right)\cdot\left(\frac{\partial\sigma(40)}{\partial\sigma''_{40}}\right) \\
+\xi^2_{\theta} &\cdot \left(\frac{\partial\sigma(40)}{\partial\theta_i}\right)^2 + 2r_{\sigma'_{40}\theta} \cdot \xi_{\sigma'_{40}} \cdot \xi_\theta \cdot \left(\frac{\partial\sigma(40)}{\partial\sigma'_{40}}\right)\cdot\left(\frac{\partial\sigma(40)}{\partial\theta_i}\right) \\
+\xi^2_{\sigma''_{40}} &\cdot \left(\frac{\partial\sigma(40)}{\partial\sigma''_{40}}\right)^2 + 2r_{\sigma''_{40}\theta} \cdot \xi_{\cdot\sigma''_{40}} \cdot \xi_\theta \cdot \left(\frac{\partial\sigma(40)}{\partial\sigma''_{40}}\right)\cdot\left(\frac{\partial\sigma(40)}{\partial\theta_i}\right)
\end{aligned} \tag{6-7}$$

where r denotes the correlation between the respective parameters.

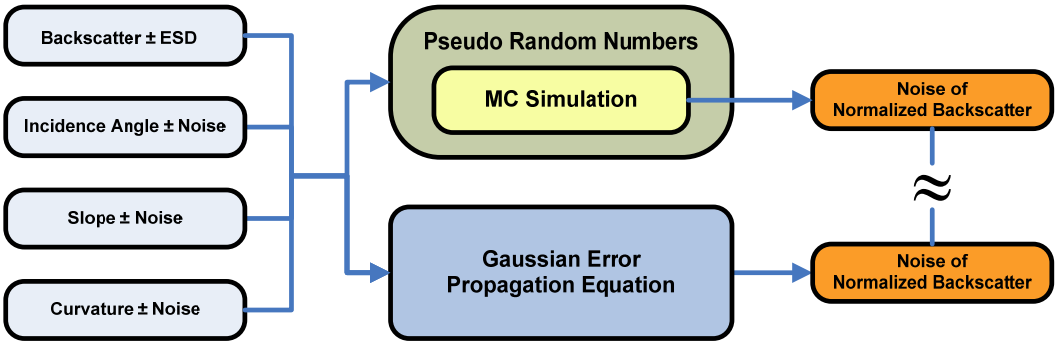

Figure 6-9. The Gaussian error propagation and MC simulation provide equivalent results.

Assuming that the correlations between the parameters are negligible, the equation 6-7 is simplified to Gaussian error propagation:

$$\xi^2_{\sigma_i(40)} = ESD^2 + \xi^2_{\sigma'_{40}} \cdot (40-\theta_i)^2 + \xi^2_{\sigma''_{40}} \cdot \left(-\frac{1}{2}(\theta_i - 40)^2\right)^2 + \xi^2_{\theta} \cdot \left(-\sigma'_{40} - \sigma''_{40} \cdot \theta_i + 40\sigma''_{40}\right)^2 \quad (6\text{-}8)$$

In parallel to classical error propagation method (equation 6-8) for estimating the uncertainty of $\sigma^0(40)$, an experiment based on the Monte Carlo simulation with 10^4 trials has been performed (figure 6-9) to find the impact of using Gaussian error propagation instead of full uncertainty propagation. The MC uncertainty propagation is an experimental probabilistic method compatible with analytical methods (Papadopoulos and Yeung 2001), which is used to solve difficult deterministic problems since computers can easily simulate a large number of experimental trials. The advantage of the Monte Carlo method to the classical methods is that it readily takes into account all nonlinearities and partial correlations of input uncertainties. Figure 6-10-a and b illustrate the results of comparison of two methods for two different grid points, one located in northern hemisphere (Mali, Africa) and the other one in southern hemisphere (Victoria, Australia). The correlation between two calculated noise values is above 0.94 with RMSE of less than about 0.008 dB indicating that the equation 6-8 is actually a reasonable approximation of equation 6-7. Although the MC simulation represents a comprehensive and ideal error propagation method encompassing all kind of error sources, the Gaussian propagation equation is preferable for operational and near real time processing as the MC propagation could be a time consuming process.

According to equation 6-8, the $\xi_{\sigma(40)}$ varies depending on the time of year and deviation of incidence angle from 40°. Figure 6-11 shows the average of $\xi_{\sigma(40)}$ on global scale.

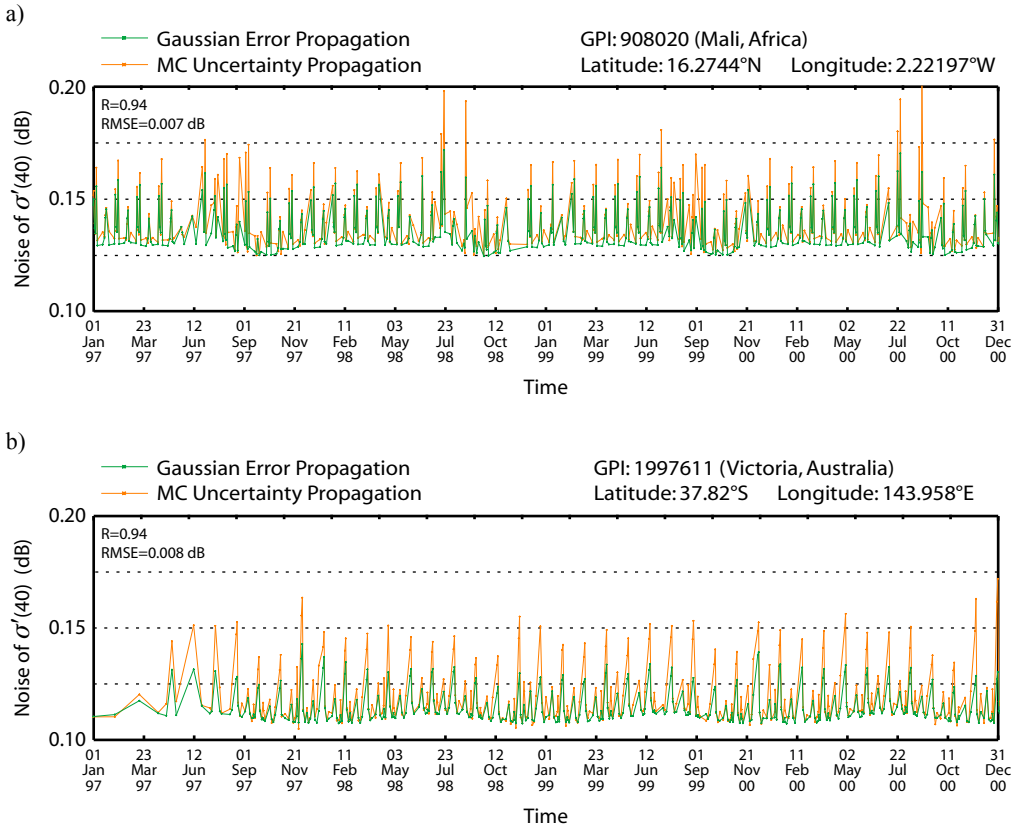

Figure 6-10. Comparison of the Gaussian error propagation and MC uncertainty propagation with 10e4 trials for two grid points located in a) Mali, Africa; b) Victoria, Australia.

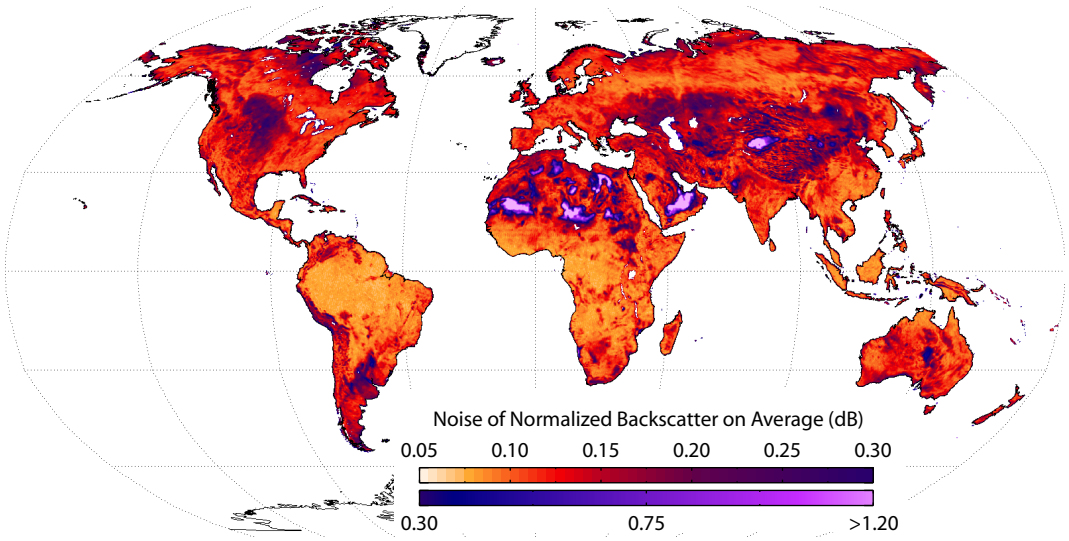

Figure 6-11. Mean of the normalized backscatter noise on global scale.

6.4. Uncertainties Related to Dry and Wet References

As it mentioned in chapter 4, dry and wet references in WARP5 are calculated by considering an uncertainty range of measurements (equation 4-9). The uncertainty range is determined using the noise of $\sigma^0(\theta_{dry})$ and $\sigma^0(\theta_{wet})$, which are obtained as following by applying Gaussian error propagation for equation 3-3:

$$\xi^2_{\sigma(\theta_{dry})} = \xi^2_{\sigma(40)} + \xi^2_{\sigma'_{40}} \cdot (\theta_{dry} - 40)^2 + \xi^2_{\sigma''_{40}} \cdot \left(\frac{1}{2}(\theta_{dry} - 40)^2\right)^2 + \xi^2_{\theta_{dry}} \cdot \left(\sigma'_{40} + \sigma''_{40} \cdot \theta_{dry} + 40\sigma''_{40}\right)^2 \tag{6-9}$$

$$\xi^2_{\sigma(\theta_{wet})} = \xi^2_{\sigma(40)} + \xi^2_{\sigma'_{40}} \cdot (\theta_{wet} - 40)^2 + \xi^2_{\sigma''_{40}} \cdot \left(\frac{1}{2}(\theta_{wet} - 40)^2\right)^2 + \xi^2_{\theta_{wet}} \cdot \left(\sigma'_{40} + \sigma''_{40} \cdot \theta_{wet} + 40\sigma''_{40}\right)^2 \tag{6-10}$$

where in WARP5, the crossover angles are set as $\theta_{dry} = 25°$ and $\theta_{wet} = 40°$ with uncertainties of $\xi_{\theta_{dry}}$ and $\xi_{\theta_{wet}}$.

According to equation 4-12 and 4-13 after substituting $\xi_{C^0_{dry}}$ and $\xi_{C^0_{wet}}$ respectively with $\xi_{\sigma(\theta_{dry})}$ and $\xi_{\sigma(\theta_{wet})}$, the uncertainties in calculation of dry and wet references are estimated as following:

$$\xi^2_{\sigma_{dry}(40)} = \xi^2_{\sigma(40)} + 2\xi^2_{\sigma'_{40}} \cdot (\theta_{dry} - 40)^2 + 2\xi^2_{\sigma''_{40}} \cdot \left(\frac{1}{2}(\theta_{dry} - 40)^2\right)^2 + 2\xi^2_{\theta_{dry}} \cdot \left(\sigma'_{40} + \sigma''_{40} \cdot \theta_{dry}\right)^2 + 2\xi^2_{\theta_{dry}} \cdot \left(40\sigma''_{40}\right)^2 \tag{6-11}$$

$$\xi^2_{\sigma_{wet}(40)} = \xi^2_{\sigma(40)} + 2\xi^2_{\sigma'_{40}} \cdot (\theta_{wet} - 40)^2 + 2\xi^2_{\sigma''_{40}} \cdot \left(\frac{1}{2}(\theta_{wet} - 40)^2\right)^2 + 2\xi^2_{\theta_{wet}} \cdot \left(\sigma'_{40} + \sigma''_{40} \cdot \theta_{wet}\right)^2 + 2\xi^2_{\theta_{wet}} \cdot \left(40\sigma''_{40}\right)^2 \tag{6-12}$$

The uncertainties of crossover angles needs more extensive investigations, which is beyond the scope of current study, but as first guess for equation 6-9 and 6-10, they are considered as $\xi_{\theta_{dry}} = \xi_{\theta_{wet}} = \pm 1°$

6.5. Noise of Surface Soil Moisture

Uncertainty of soil moisture estimation is obtained by using the Gaussian error propagation equation for the equation 3-9:

$$\xi_{\Theta}^{2} = \xi_{\sigma(40)}^{2}\left(\frac{100}{\sigma_{wet}^{0}(40)-\sigma_{dry}^{0}(40)}\right)^{2} + \xi_{\sigma_{dry}(40)}^{2}\left(\frac{100\times\left(\sigma^{0}(40)-\sigma_{wet}^{0}(40)\right)}{\left(\sigma_{wet}^{0}(40)-\sigma_{dry}^{0}(40)\right)^{2}}\right)^{2} + \xi_{\sigma_{wet}(40)}^{2}\left(\frac{100\times\left(\sigma^{0}(40)-\sigma_{dry}^{0}(40)\right)}{\left(\sigma_{wet}^{0}(40)-\sigma_{dry}^{0}(40)\right)^{2}}\right)^{2} \quad (6\text{-}13)$$

By using equation 6-13, a range of possible error sources in soil moisture retrieval algorithm are taken into account. The noise of relative soil moisture reflects the contribution of all noise parameters in the retrieval procedure on the condition that the validity of model's initial assumptions is preserved. The factors influencing the noise estimation of soil moisture can be categorized as:

A) Invariable in time

- Estimated standard deviation of backscatter (ESD)
- Incidence angle uncertainty (ξ_{θ})
- Uncertainty of dry and wet crossover angles ($\xi_{\theta_{dry}}$ and $\xi_{\theta_{wet}}$)
- Dry and wet crossover angles (θ_{dry} and θ_{wet})

B) Variable in time

depending on day of the year:

- Slope and curvature at 40° (σ'_{40} , σ''_{40})
- Noise of slope and curvature ($\xi_{\sigma'_{40}}$, $\xi_{\sigma''_{40}}$)
- Dry and wet references ($\sigma_{dry}^{0}(40)$ and $\sigma_{wet}^{0}(40)$)

depending on data acquisition:

- Incidence angle (θ)
- Normalized backscatter at 40° ($\sigma^{0}(40)$)

Figure 6-12 shows how all above mentioned factors affect the soil moisture noise estimations in two different regions. The estimated noise in some regions has seasonal fluctuations. The periodic behavior of soil moisture noise is because of the annual variations of slope and curvature functions, which also influence the noise of dry reference through vegetation correction procedure. Figure 6-13 illustrates the averaged value of soil moisture

noise on global scale. Comparing the global distribution of ESD values in figure 5-23 and sensitivity map (figure 4-28-b) with the spatial patterns visible in figure 6-13 indicates that the major components of soil moisture error model are ESD and sensitivity ($\sigma^0_{wet}(40) - \sigma^0_{dry}(40)$). Mountainous areas with high standard deviation of elevation, water bodies, sand desert, and dense vegetated areas cause the highest uncertainty in soil moisture calculation.

Although the WARP5 noise model comprises the most errors sources coming from instrument, azimuthal anisotropy, and model's parameters, it should not be considered as a full validation of scatterometer derived soil moisture. For example the retrieval algorithm fails in estimation of soil moisture when the soil surface is frozen or covered by snow. Backscattering from snow covered areas or frozen soil surface cause imperceptible uncertainty in soil moisture calculation, which cannot be detected from scatterometer observations. Therefore such circumstances should be flagged or masked carefully using external data. The estimated noise parameter shows the quality of retrieval algorithm in time and space and provides useful information for many applications e.g. data assimilation.

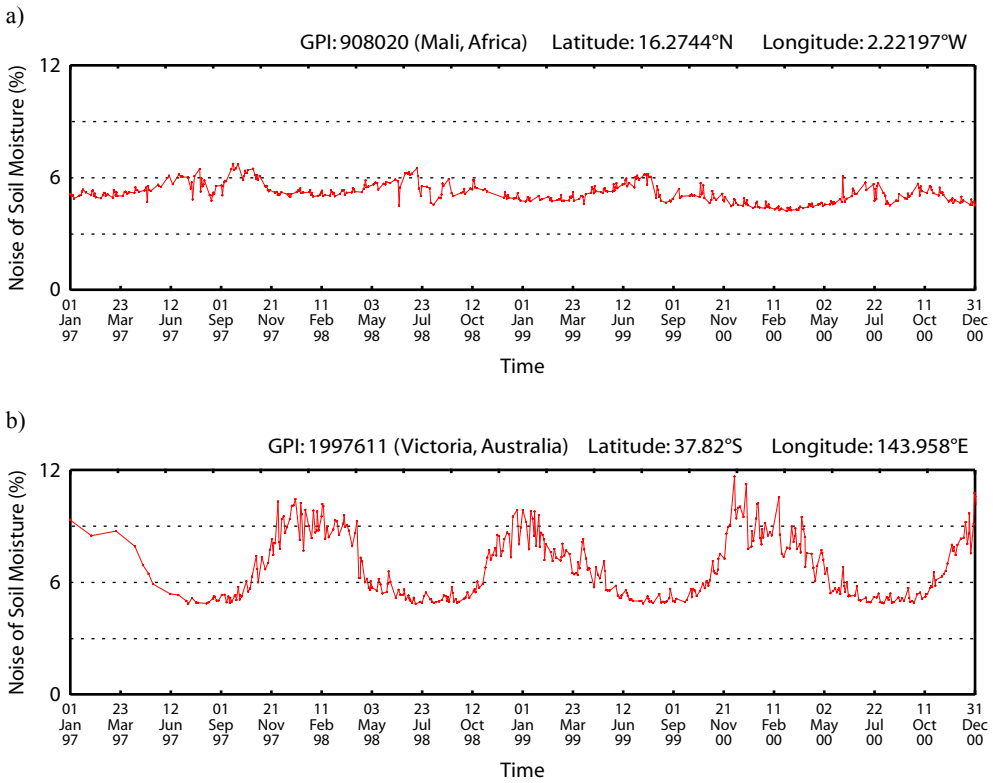

Figure 6-12. Estimated noise of soil moisture as time series for two grid points located in a) Mali, Africa; b) Victoria, Australia.

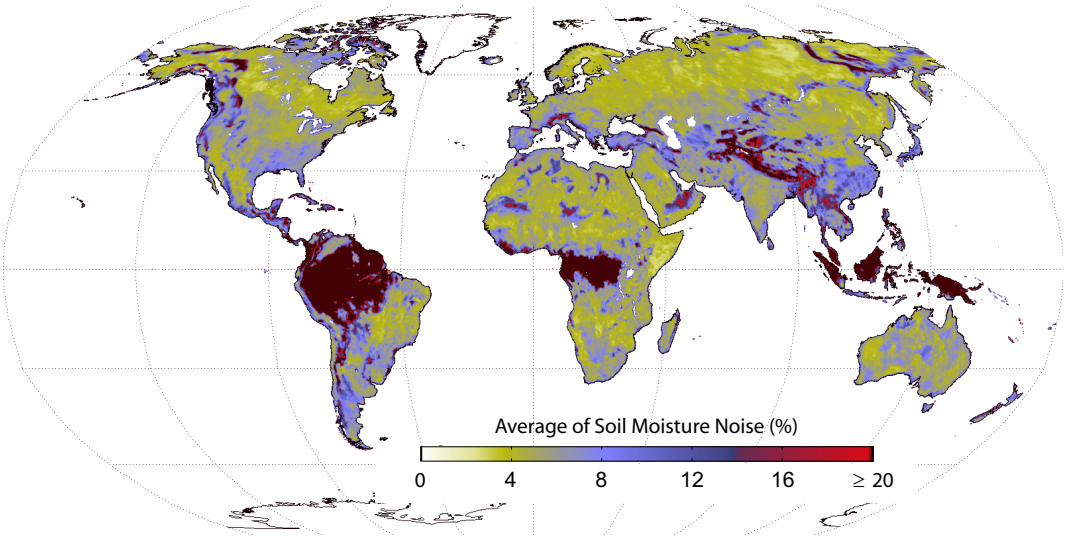

Figure 6-13. Global noise estimation of soil moisture on average.

7. Model Validation & Data Quality Assessment

The new soil moisture retrieval algorithm, WARP5, results in a more consistent and uniform product with higher resolution than the earlier method, WARP4 (Figure 7-1). Although the outcomes of the both algorithms are highly correlated, in some regions the two algorithms produce considerably different results. Figure 7-2 illustrates the correlation coefficients and root mean square of deviations between the two products. To find out the significance of the improvements in the new method, the datasets need to be compared with in-situ observations.

Quantitative validation of the remotely sensed soil moisture data using field observations seems to be challenging because of the high spatial and temporal variability of the top soil water content (Western et al. 1998). There are too many processes affecting soil water balance including precipitation, surface runoff, evaporation and evapotranspiration, vertical and lateral flow, and snowmelt (Hillel 1998). Due to the dynamic nature of these processes, there is an accuracy limitation of verification of remotely sensed measurements with in-situ observations (Schmugge and Jackson 1996). Scaling issues are also of great importance when comparing two datasets with different resolutions. Formulations of physical processes appropriate at a given scale level usually are not applicable to extrapolate immediately to the

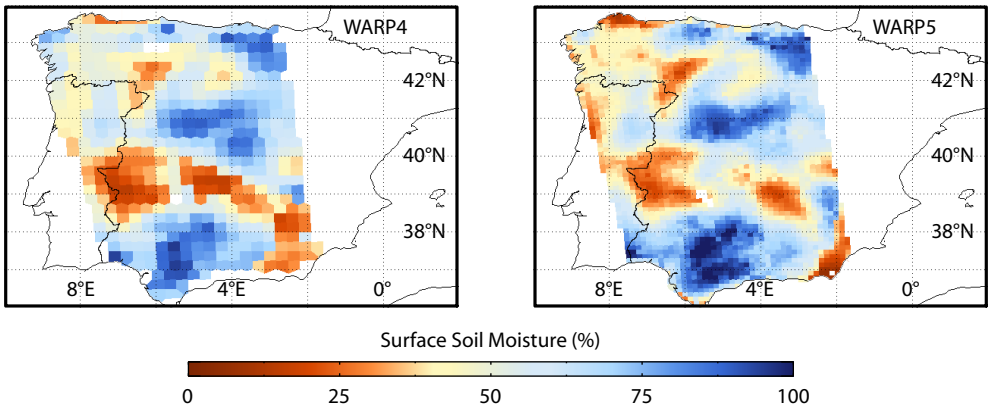

Figure 7-1. Iberian Peninsula, comparison of WARP4 and WARP5 soil moisture data.

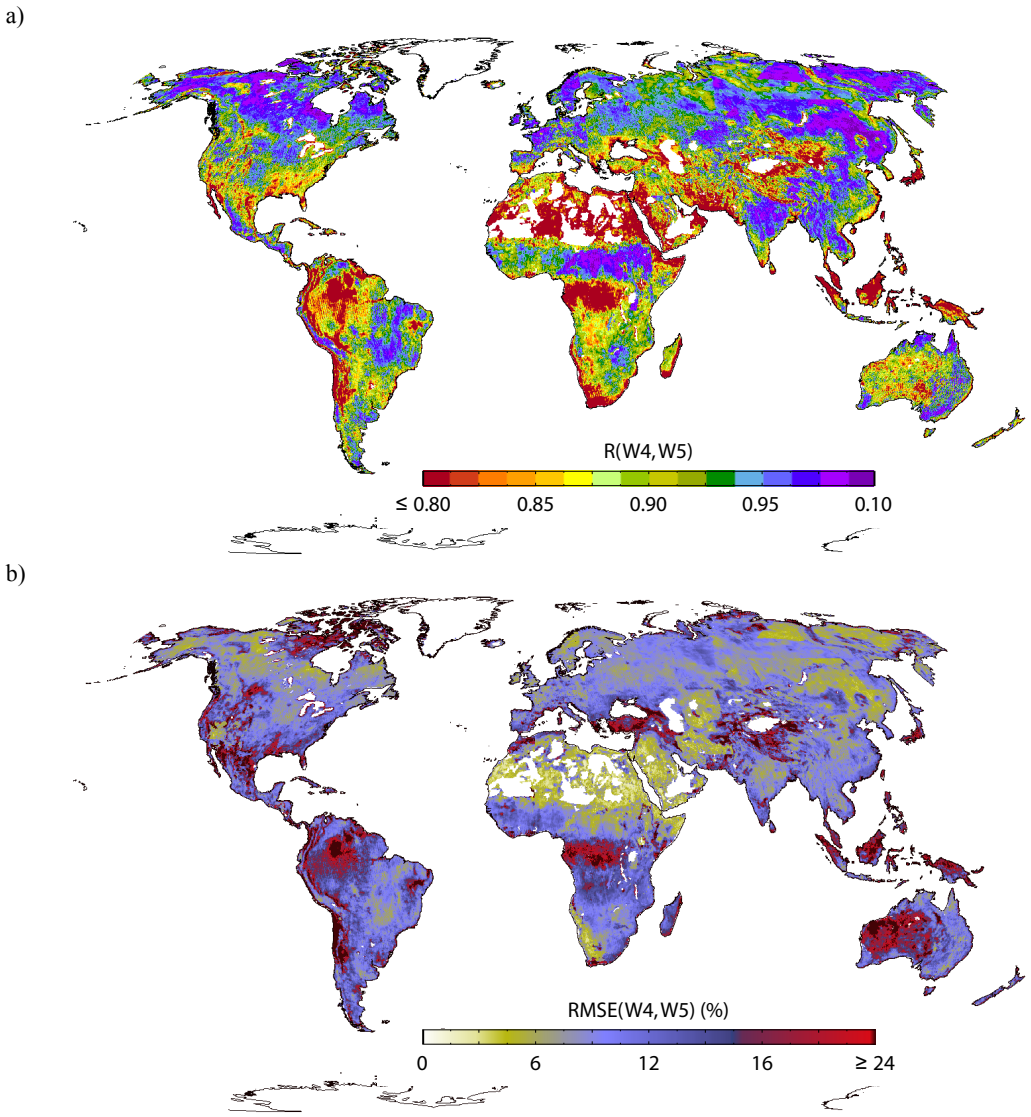

Figure 7-2. Comparing WARP4 with WARP5: a) Correlation coefficients, b) Root Mean Square Error.

adjoining levels (Klemes 1983). The spatial resolution of the Scatterometers onboard ERS and Metop is on the order of tens of kilometers. Unfortunately, there are only few soil moisture networks worldwide, which can provide field measurements comparable in this scale level.

To validate the model modifications made in WARP5, two different in-situ and two modeled soil moisture datasets are used. The scatterometer derived soil moisture data are compared with the in-situ soil moisture observed in the MESONET network located in Oklahoma state, USA and REMDEHUS network located in Salamanca, Spain and also with a multi-modeled reanalysis dataset from Global Soil Moisture Project (GSWP) and the ECMWF's global reanalysis data, which is an output of the ERA-Interim project.

7.1. Oklahoma MESONET Network

7.1.1. Study Area

Oklahoma state is located in the south central region of the United States of America covering an area of 181196 km². Oklahoma is the 28th most populous and 20th largest state in United States. Forests cover 24% of the area and a broad band of prairie and steppe shelter expansive ecosystems in the state's central and western portions, although cropland has largely replaced native grasses. Oklahoma is situated between the Great Plains and the Ozark Plateau in the Gulf of Mexico watershed, sloping from the high plains in the west to the southeastern low wetlands. The highest peak, Black Mesa (1516 m above sea level), located in the northwest corner in the Oklahoma Panhandle and the state's lowest point is on the Little River near its far southeastern boundary (88 m above sea level). Figure 7-3 illustrates the region's land cover (USGS 1999) and topography (USGS 1996). Oklahoma is placed in a temperate region with continental climate. Because of its position between zones of differing prevailing temperature and winds, weather patterns within the state can vary widely between relatively short distances. The southern and eastern portions of the state are influenced heavily by warm and humid air moving northward from the Gulf of Mexico but transitions to a semi-arid zone in the western parts and the high plains of the Panhandle are less frequently affected by southern moisture. Precipitation and temperature fall from east to west accordingly. The southeast areas have an annual average temperature of 17 °C and an annual rainfall of 1420 mm, while in areas of the panhandle average temperature is 14 °C and annual rainfall is under 430 mm. Drought is a recurring part of Oklahoma's climate cycle. In Oklahoma region summers are long and usually quite hot. Winters are shorter and less rigorous than those of the more northern states. Periods of extreme cold are infrequent, and those lasting more than a few days are rare (Arndt 2003).

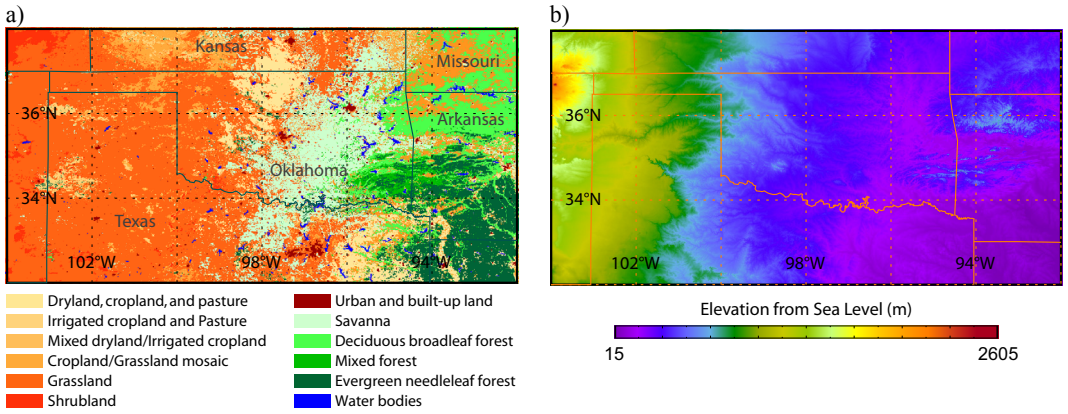

Figure 7-3. a) Oklahoma's land cover map. b) Oklahoma's topography map.

7.1.2. Mesonet Soil Moisture Observation Network

The Oklahoma Mesonet network consists of 127 automated meteorological monitoring sites including soil moisture sensing devices (Brock et al. 1995). Stations are distributed across Oklahoma with at least one station in every county. The soil moisture sensors installed at Oklahoma Mesonet sites are heat dissipation sensors manufactured by Campbell Scientific known as 229-L and deployed at four different depths (5, 25, 60, and 75 cm below the surface). Data are collected every 30 minutes and a series of automated and manual processes performs a quality control and convert the raw data into daily average values. The 229-L sensors measure a temperature difference, which is the change in sensor temperature after a heat pulse has been introduced (Basara and Crawford 2000). Because the specific heat and thermal conductivity of water are different from that of the porous ceramic matrix, the magnitude of heat dissipation varies with varying contents of soil water. Thus, a constant interval of heating leads to different temperature rises depending upon the water content of the soil. The soil water content depends strongly on soil texture while soil matric potential is exponentially related to soil wetness. Therefore a normalized parameter of the sensor response called Fractional Water Index (FWI) is used to measure soil moisture dynamics. FWI is a unitless value ranging from 0 for very dry soil to 1 for soil at field capacity. FWI is a linear quantity, which is not limited by varying soil texture at each site (Illston et al. 2004).

7.1.3. Results of Comparison

In this study we used the 5cm layer FWI measurements in a period of 3 years (2004-2006). Figure 7-4 illustrates in-situ soil moisture time series measured in one of the Mesonet stations compared with the scatterometer observations. In-situ measurements are fairly accurate but they are point measurements. Since soil moisture has an extreme spatial

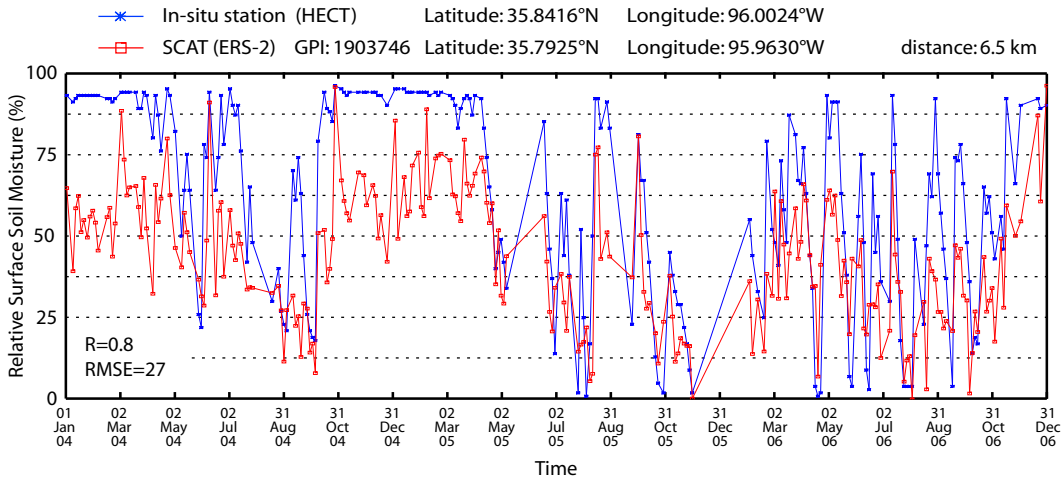

Figure 7-4. Comparison of field measurements with scatterometer observations in Oklahoma, USA.

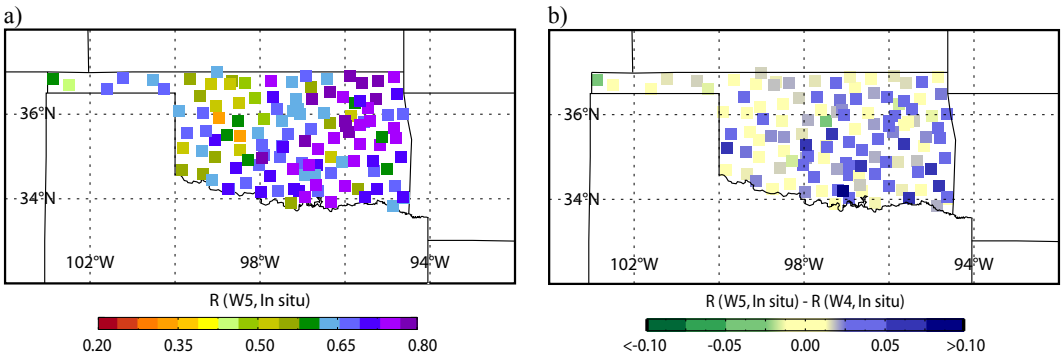

Figure 7-5. a) Correlation coefficients between WARP5 soil moisture data and Oklahoma Mesonet in-situ observations. b) Difference of the correlation coefficients obtained from comparing WARP4 and WARP5 data with in-situ observations.

variability behavior at small scale, it is very difficult to estimate catchment average soil moisture from such point measurements (Western et al. 2002). Therefore comparison of in-situ observations with scatterometer data can be reasonable only if the in-situ data are linked to the atmospheric-forcing related component of soil moisture at regional scale. Figure 7-5-a shows the correlation coefficients between in-situ and WARP5 soil moisture data. As it is expected lower correlation coefficients are observable in irrigated cropland areas, where point measurements usually do not follow the regional averages. In general the comparison of in-situ data with WARP5 and WARP4 soil moisture measurements indicates remarkable improvements in soil moisture estimation using the new algorithm. The difference in correlation coefficients in some stations is up to 0.1 (figure 7-5-b).

7.2. Salamanca REMEDHUS Network

7.2.1. Study Area

The study area is covering about 1,285 km² and is located in the central sector of the Duero basin in the Salamanca province, Spain. The climate in this area is described as semi-arid continental Mediterranean with a mean annual rainfall of 385 mm. The Salamanca's climate is fairly dry with a mean temperature about 12°C and annual potential evapotranspiration of 908 mm with any rainy weather and showers clearing quickly. Winter weather in the Salamanca area can be breezy, with occasional heavy showers but frosty weather and snow is uncommon. The most abundant soils in the studied area are Luvisols and Cambisols, with a predominantly sandy texture (mean sand content, 71%), especially at the surface horizons. Occasionally, there are clayey horizons at the bottom of the profiles. The organic matter content is very low (mean, 0.9%). Throughout almost all the territory, the soil is used for agricultural purposes, rain-fed crops being the norm (80% cereals).

7.2.2. REMEDHUS Soil Moisture Observation Network

The REMEDHUS network consists of 23 soil-moisture measuring stations, which are set up evenly in the area (Ceballos et al. 2002). The stations are spread irregularly based on the distribution of the main physiographic and pedological units of the area. Each station is equipped with two-wire Time Domain Reflectometry (TDR) probes, installed horizontally at depths of 5, 25, 50 and 100 cm. In this study, the only probes that were used were those installed at 5 cm depth, which represents approximately the 2–8 cm soil-moisture layer. Measurements were taken fortnightly at each of the stations. All stations can be considered to be hydrologically independent even though they are all included within the same climatic context. Gravimetric measurements were used for calibration of the formulas used for the soil moisture extraction.

7.2.3. Results of Comparison

The soil moisture observation in each REMEDHUS station varies locally due to changing soil types, topography and land use, however the large-scale atmosphere-driven soil moisture component is preserved. The local-scale variations of soil moisture make the comparison of point-like in-situ measurements with scatterometer data difficult as the whole covering area of the network is comparable to only one scatterometer pixel. The other problem is the acquisition time difference between in-situ and scatterometer observation that is on average above three days. Figure 7-6 shows an example of in-situ observations compared with the scatterometer time series, which are already scaled between the lowest and highest values of in-situ data. The correlation coefficient between the average value of the in-situ data observed over 20 stations and WARP5 data is about 0.65. There is no significant improvement observable in the new soil moisture dataset in this area, although the correlation coefficients of WARP5 data are slightly higher than in WARP4.

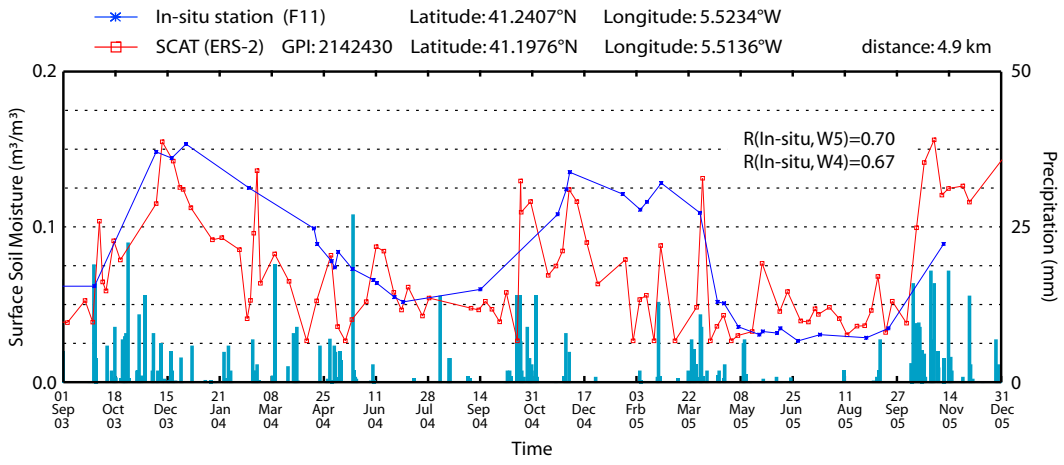

Figure 7-6. Comparison of field observation from one of the REMEDHUS stations (F11) with WARP5 data.

7.3. Comparison of Scatterometer Data with Modeled Data

To carry out a global evaluation of the new retrieval method, the WARP4 and WARP5 soil moisture data are compared to modeled datasets. However, the interpretation of results has to be done carefully as modeled datasets do not necessarily represent the truth. Each modeled data has own strengths and weaknesses. Robock *et al.* (1998) noted that the agreement of both the amplitude and the interannual variation of soil moisture between 30 different atmospheric general circulation models was poor. The intention here is not to determine the absolute accuracy of the scatterometer soil moisture data but to evaluate how changes in the retrieval procedure compares to modeled data.

7.3.1. Comparison with GSWP Dataset

The Global Soil Moisture Project (GSWP) is an environmental modeling research activity of the Global Land-Atmosphere System Study (GLASS). GSWP-2 is a multi reanalysis model, wherein over a dozen different land surface schemes are used. The bulk of the data are reported at a daily interval. The models all adhere to the same land-sea mask, and as closely as possible to the supplied datasets of vegetation distribution and properties, soil properties, surface albedos, etc. The model simulations for GSWP are conducted globally over land (excluding Antarctica) on a regular 1° × 1° grid, with results reported for the 10-year core period 1986-1995 (Dirmeyer et al. 2006).

In this study the scatterometer derived soil moisture data are compared with the multi-model analysis of soil wetness in a period of four years (1991-1995). Because of lower resolution of GSWP data, the nearest scatterometer observations to GSWP grid points are taken to the comparison procedure. The correlation coefficients of comparison are indicated in figure 7-7. Although in most regions high correlation between modeled and scatterometer data is evident, the comparison results do not show any significant difference between WARP4 and WARP5 datasets. This is because of very coarse resolution of GSWP data and also unavailability of long-term modeled data.

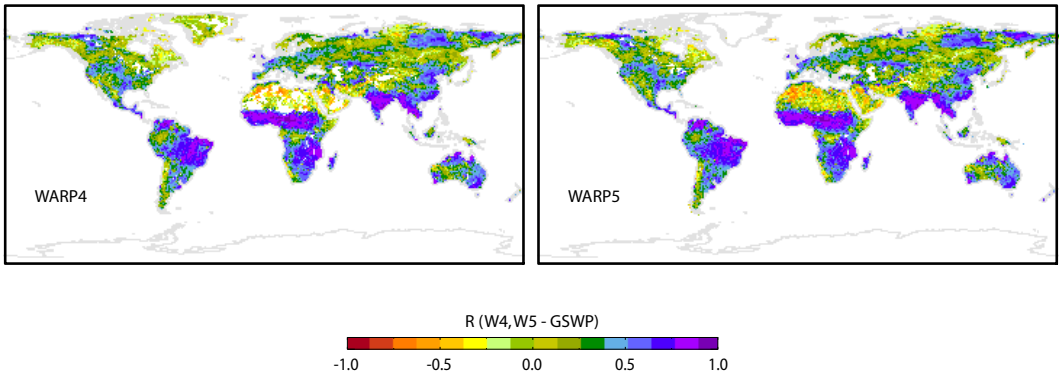

Figure 7-7. Correlation coefficients (R) between WARP5 and WARP4 with GSWP.

7.3.2. Comparison with ERA-Interim Dataset

ERA-Interim soil moisture data is outcome of the ECMWF's (European Center for Medium-range Weather Forecasts) reanalysis project based on the Integrated Forecast Model, a global numerical weather prediction model. The dataset used in this study covers the entire lifetime of the ERS satellites and is an advanced version of the widely used ERA-40 reanalysis dataset (Uppala et al. 2005). ERA-Interim uses mostly the sets of observations acquired for ERA-40, supplemented by data for later years from ECMWF's operational archive. The data has a spatial resolution of 50km. Land surface processes are described by the Tiled ECMWF Scheme for Surface Exchanges over Land (TESSEL) (Van den Hurk et al. 2000). Soil moisture is analyzed every day at 00, 06, 12, 18 UTC using an optimum interpolation scheme of screen level observations. To facilitate the comparison, each dataset has been collocated to a regular 0.25 degree grid using a nearest neighbor resampling method and satellite observations have been pooled into six hourly files. Observations were masked if one of the data sets indicated missing observations or if the ERA-Interim reanalysis indicated freezing or snow covered conditions.

Figure 7-8 shows the correlation between the modeled and scatterometer observed soil moisture (WARP5) and Figure 7-9 indicates areas where the correlation coefficients are improved using the new algorithm. In general, the correlation is positive over large parts of the land surface, with maximum values around 0.9. At 85% of the land points the correlation is significant at the 0.05 level. The spatial distribution of the correlation clearly reflects zonal climate patterns. As expected, the correlation is high in areas characterized by a strong seasonal soil moisture cycle (for example in Monsoon areas). Over deserts the correlation becomes negative. This problem has also been reported by Wagner *et al.* (2003) and can be

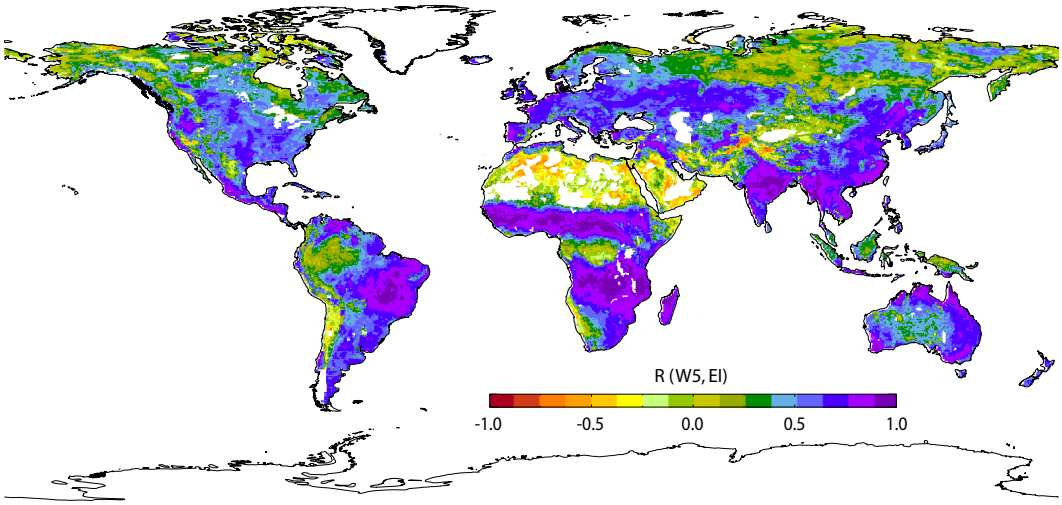

Figure 7-8. Correlation coefficients (R) between WARP5 and ERA-Interim soil moisture data.

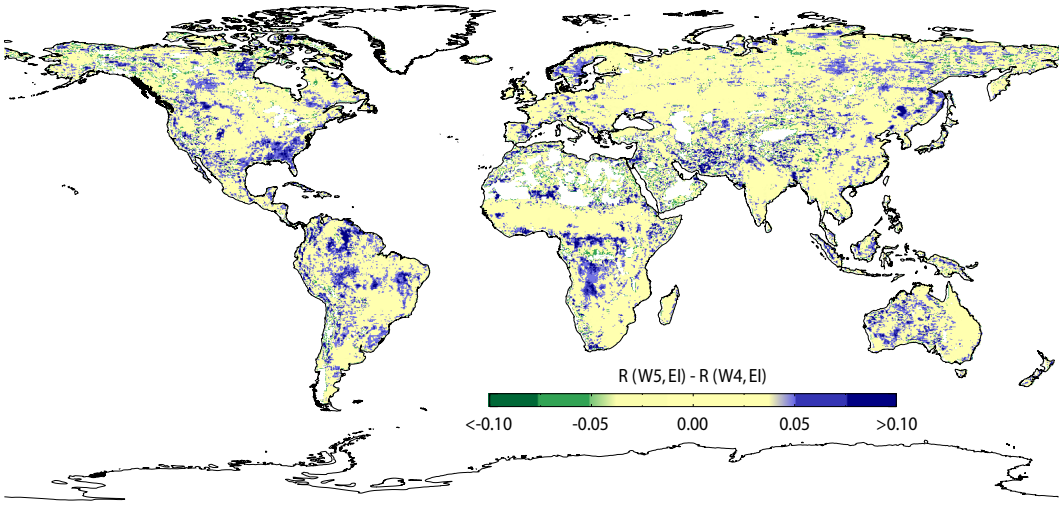

Figure 7-9. Difference of correlation coefficients between ERA-Interim and WARP5 compared to the correlation coefficients of ERA-Interim and WARP4.

attributed to a shortcoming in the satellite retrieval method. The maps also exhibit some unexpected features. Over Europe, the correlation is comparably high. Similarly, the correlation is high over South East China which is supposed to be characterized by a low sensitivity of the microwave signal to soil moisture due to a high amount of above ground biomass. The high correlations over Spain are specifically encouraging. The climate in this area has a wet winter and a dry summer. Consequently, soil moisture and vegetation behave anti-cyclical, while in the other climate types vegetation and soil moisture are often highly correlated. Under the latter conditions, imperfections in the backscatter model may be hidden because vegetation may act as a proxy indicator for soil moisture or vice versa. Over Spain such imperfections of the retrieval method would yield inconsistent results.

Figure 7-9 shows examples of how the new processing scheme works in practice in the problematic regions. The scatterometer soil moisture estimations in northern China (right image) are heavily affected by azimuthal viewing effects due to large scale farming activities (Bartalis et al. 2006). These effects are most clearly visible during winter. During this time the soil is frozen and temperatures are well below 0°C. For the scatterometer the frozen soil appears comparable to a completely dry soil. The variation visible in the soil moisture signal is therefore completely artificial, caused by azimuthal anisotropies. In WARP4 processing this variation can make up to 40%. In WARP5 the effect is substantially lowered to a value of 10%. Also during summer the improved functioning of the retrieval is confirmed by a better fit of satellite observations to modeled soil moisture. Consequently, the correlation coefficients in this region increase up to more than 0.2. The new processing

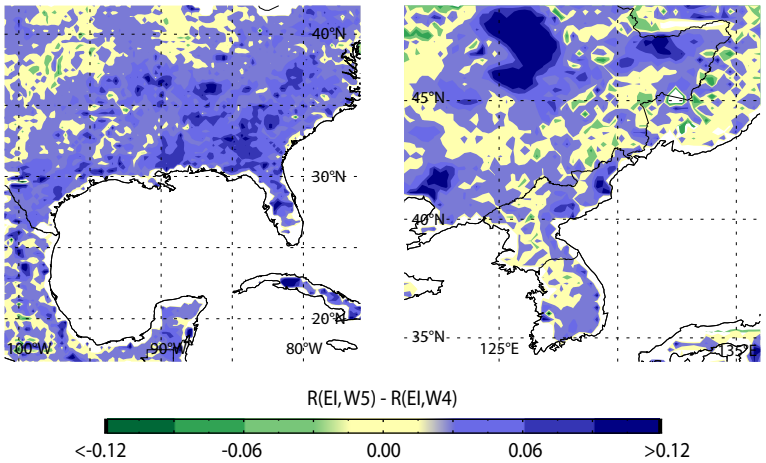

Figure 7-10. Difference of correlation coefficients between ERA-Interim and WARP5 compared to the correlation between ERA-Interim and WARP4 in two different regions.

also leads to spatially more uniform soil moisture estimates over the southeastern parts of USA. Over this region wrong estimation of the dry/wet references in WARP4 led to inconsistence soil moisture estimates compared to the adjacent regions. The improvements made in WARP5 algorithm corrects irregularities of soil moisture patterns in this area that is confirmed by the modeled soil moisture data (figure 7-10 left image).

Some part of the discrepancy between the modeled and scatterometer data can be described by the estimated retrieval noise. Figure 7-11 shows how the correlation between ERA-Interim and WARP5 data decreases by increasing the retrieval noise in lower latitudes.

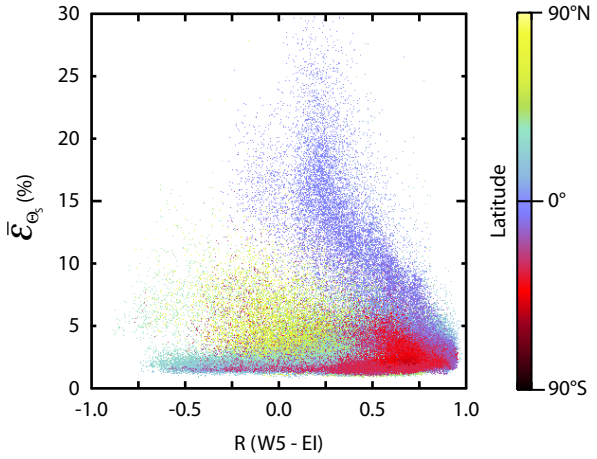

Figure 7-11. Correlation between WARP5 and ERA-Interim soil moisture data increases clearly by decreasing the estimated soil moisture retrieval noise excluding the higher latitudes.

Summary and Conclusions

Soil moisture has been recognized as an important component of the water cycle in hydrological and natural environmental processes. Soil moisture information is demanding for a wide range of applications concerning water supply, agriculture, weather forecasting, climate modeling, and etc. High sensitivity of dielectric properties of the water content in the soil to low frequency microwaves makes the microwave remote sensing very attractive for the measurement of soil moisture variations. Compared to conventional in-situ measurements, soil moisture remote sensing using spaceborne sensors have the advantage of high temporal sampling rate with global coverage.

In this study an enhanced algorithm for soil moisture retrieval based on TU-Wien change detection method was presented using long-term backscattering data acquired by the scatterometers, active microwave instruments onboard the ERS and Metop satellites. The backscattering coefficient σ^0 measured by the scatterometers from the land surface depends on the surface roughness, texture, soil moisture, vegetation cover, and the local incidence angle. All these factors affect backscatter signal in different scales. The surface roughness and soil texture is in general considered to be stable over time at the scatterometers' observation scale (25-50 km). Vegetation is expected to vary from days to weeks depending on the regional climate zone. Soil moisture has a very temporal behavior and can to be altered in few minutes to hours by precipitation, evapotranspiration, and infiltration.

To extract soil moisture dynamics from the backscatter coefficients, the incidence angle dependency of backscatter and consequently the annual variation of vegetation are modeled using multi-looking capability of the scatterometers. The model parameters, slope σ' and curvature σ'' are used to remove the incidence angle dependency of the backscatter signal and also to correct for vegetation influenced signal. An accurate estimation of the slope and curvature functions $\sigma'(t)$ and $\sigma''(t)$ was succeeded by using a quasi-Monte Carlo simulation technique. The Monte Carlo simulation, performed in the new methodology, made it possible to approach to an optimal time window length for sampling of the calculated local slope values. This is important to avoid filtering high-frequency vegetation dynamics in calculations and simultaneously obtain more sensitive and consistent slope and curvature parameters. In some regions, the correction amount of the slope value calculated

in the new method exceeds 0.01 dB/degree. Simulation experiments show that a wrong calculation of the slope parameter by the earlier method could lead to more than 10% error in soil moisture estimation. The new slope and curvature functions are spatially more uniform with smooth temporal variation.

Besides soil moisture retrieval in the WARP5 algorithm, an uncertainty analysis was performed for each step of processing. The WARP5 error modeling is initialized with the azimuthal noise of backscatter (ESD) and propagated together with the noise of the model's parameters in each processing step through the retrieval algorithm. The azimuthal noise of backscatter represents surface anisotropy induced by different land cover types. The most important surface features influencing backscatter anisotropy are water bodies, areas with complex topography, urban areas, and sand deserts. Lakes, rivers, coastal areas, and floodplains increase the azimuthal noise significantly up to more than 1.2 dB depending on the coverage area compared to the scatterometer's footprint. The highest ESD values are observable in sand desert areas. Backscatter mechanism of sand desert is presumed to be a mixture of surface and volume scattering and therefore more complicated to model. On the opposite, rain forests indicate an isotropic response to scatterometer signals. The average of ESD values in very dense vegetated areas is about 0.13 dB, which can be considered as the noise of instrument. In WARP5 to propagate uncertainty of measurements through the model, a combined method of numerical and analytical solutions was used. The uncertainties in calculation of the slope and curvature parameters were determined by the Monte Carlo simulation. The Monte Carlo method has the advantage of direct computation of uncertainty when there is a lack of knowledge or even when the model contains discontinuities or extreme nonlinearities, although the methodology needs intensive computations. Subsequently using the Gaussian error propagation equation, uncertainties of the model's parameters are carried over in each stage of processing to determine the noise of soil moisture for each individual measurement. The estimated noise of soil moisture shows a periodic behavior as it is influenced by seasonal variation of the slope and curvature functions and their relative noise values as well as the dry and wet references. The WARP5 error analysis not only provides quality information about the product but also helps to improve the calculation of model parameters during the retrieval process. Dry and wet references, determined based on the noise of signal, approximate truthful extreme events and therefore result in spatially uniform references for scaling the normalized backscatter.

The improvements obtained by the new methodology result in a more uniform performance of the model and consequently spatially consistence soil moisture product with a better resolution. The artificial variations in soil moisture due to inconsistence estimation of model's parameters or caused by the azimuthal effects are effectively weakened through

the new parameterization. Comparison of satellite data with in-situ observations and modeled data confirms the improvements made in the new algorithm especially in regions characterized with high azimuthal noise. For example the comparison of Mesonet in-situ observations with the new soil moisture data shows up to 0.1 larger correlation coefficients than with the earlier model.

Although the new method yields several significant improvements, the results show that more work is required on soil moisture retrieval over deserts to understand the complex backscatter mechanism in such regions. Determination of the right dry/wet crossover angles and respective uncertainty are important and remain to be fully investigated as they impact considerably the calculation of the dry/wet references as well as the vegetation correction procedure. More work is also needed for the correction of wet reference in the areas, where soil never reaches the saturation point. In the current retrieval algorithm, only SCAT time series are used to produce model's parameter database. In the near future a more robust parameter database can be established by combining SCAT and ASCAT datasets when enough ASCAT data are acquired.

9. Bibliography

Alvarez-Mozos, J., J. Casali, M. Gonzalez-Audicana and N. E. C. Verhoest (2005), Correlation between ground measured soil moisture and RADARSAT-1 derived backscattering coefficient over an agricultural catchment of Navarre (North of Spain), *Biosystems Engineering*, Vol. *92*, pp. 119.

Ahmed, N. U. (1995), Estimating soil moisture from 6.6 GHz dual polarization, and/or satellite derived vegetation index, *International Journal of Remote Sensing*, Vol. *16*, pp. 687.

Albergel, C., C. Ruediger, D. Carrer, J. C. Calvet, N. Fritz, V. Naeimi, Z. Bartalis and S. Hasenauer (2008), An evaluation of ASCAT surface soil moisture products with in-situ observations in southwestern France, *Hydrology and Earth System Sciences Discussions*, Vol. *5*, pp. 2221-2250.

Anguela, T. P., M. Zribi, S. Hasenauer, F. Habets and C. Loumagne (2008), Analysis of surface and root-zone soil moisture dynamics with ERS scatterometer and the hydrometeorological model SAFRAN-ISBA-MODCOU at Grand Morin watershed (France), *Hydrology and Earth System Sciences Discussions*, Vol. *5*, pp. 1903-1926.

Arndt, D. (2003), The climate of Oklahoma, Oklahoma Climatological Survey, Norman, Oklahoma.

Attema, E. P. W. (1991), The Active Microwave Instrument on-board the ERS-1 satellite, *Proceedings of the IEEE*, Vol. *79*, pp. 791.

Attema, E. P. W. and F. T. Ulaby (1978), Vegetation Modeled as a Water Cloud, *Radio Science*, Vol. *13*, pp. 357.

Bagnold, R. A. (1941), The Physics of Blown Sand and Desert Dunes, Methuen & Co., London.

Baronti, S., F. Del Frate, P. Ferrazzoli, S. Paloscia, P. Pampaloni and G. Schiavon (1995), SAR polarimetric features of agricultural areas, *International Journal of Remote Sensing*, Vol. *16*, pp. 2639.

Bartalis, Z., K. Scipal and W. Wagner (2006), Azimuthal anisotropy of scatterometer measurements over land, *IEEE Transactions On Geoscience and Remote Sensing*, Vol. *44*, pp. 2083-2092.

Basara, J. B. and T. M. Crawford (2000), Improved installation procedures for deep-layer soil moisture measurements, *Journal of Atmospheric and Oceanic Technology*, Vol. *17*, pp. 879-884.

Bateson, L. and I. H. Woodhouse (2004), Observations of scatterometer asymmetry over sand seas and derivation of wind ripple orientation, *International Journal of Remote Sensing*, Vol. *25*, pp. 1805-1816.

Bevington, P. R. (1969), *Data reduction and error analysis for the physical sciences*, XV, pp. 336 , McGraw-Hill, New York.

Blackman, R. B. and J. W. Tukey (1959), Particular pairs of windows, *The measurement of power spectra from the point of view of communications engineering*, pp. 98-99, New York: Dover.

Brock, F. V., K. C. Crawford, R. L. Elliott, G. W. Cuperus, S. J. Stadler, H. L. Johnson and M. D. Eilts (1995), The Oklahoma Mesonet: A Technical Overview, *Journal of Atmospheric and Oceanic Technology*, Vol. *12*, pp. 5-19.

Cacuci, D. G. (1981), Sensitivity theory for nonlinear systems. I. Nonlinear functional analysis approach, *Journal of Mathematical Physics*, Vol. *22*, pp. 2794-2802.

Ceballos, A., K. Scipal, W. Wagner and J. Martinez-Fernandez (2005), Validation of ERS scatterometer-derived soil moisture data in the central part of the Duero Basin, Spain, *Hydrological Processes*, Vol. *19*, pp. 1549-1566.

Cognard, A. L., C. Loumagne, M. Normand, P. Olivier, C. Ottle, D. Vidalmadjar, S. Louahala and A. Vidal (1995), Evaluation Of The Ers-1 Synthetic Aperture Radar Capacity To Estimate Surface Soil-Moisture - 2-Year Results Over The Naizin Watershed, *Water Resources Research*, Vol. *31*, pp. 975-982.

Crapolicchio, R. and P. Lecomte (2003), On the stability of Amazon rainforest backscattering during the ERS-2 Scatterometer mission lifetime, ASAR workshop 2003, Canada.

Crow, W. T. and X. W. Zhan (2007), Continental-scale evaluation of remotely sensed soil moisture products, *Ieee Geoscience and Remote Sensing Letters*, Vol. *4*, pp. 451-455.

Davidson, M. W. J., T. Le Toan, F. Mattia, G. Satalino, T. Manninen and M. Borgeaud (2000), On the characterization of agricultural soil roughness for radar remote sensing studies, *IEEE Transactions On Geoscience And Remote Sensing*, Vol. *38*, pp. 630-640.

De Jeu, R. A. M., W. Wagner, T. R. H. Holmes, A. J. Dolman, N. C. van de Giesen and J. Friesen (2008), Global Soil Moisture Patterns Observed by Space Borne Microwave Radiometers and Scatterometers, *Surveys in Geophysics*, Vol., pp. 1-22.

De Ridder, K. (2000), Quantitative estimation of skin soil moisture with the Special Sensor Microwave/Imager, *Boundary-Layer Meteorology*, Vol. *96*, pp. 421-432.

De Wit, A. M. and C. A. van Diepen (2007), Crop model data assimilation with the Ensemble Kalman filter for improving regional crop yield forecasts, *Agricultural and Forest Meteorology*, Vol. *146*, pp. 38-56.

Deroin, J. P., A. Company and A. Simonin (1997), An empirical model for interpreting the relationship between backscattering and arid land surface roughness as seen with the SAR, *IEEE Transactions on Geoscience and Remote Sensing*, Vol. *35*, pp. 86.

Dirmeyer, P. A., X. Gao, M. Zhao, Z. Guo, T. Oki and N. Hanasaki (2006), GSWP-2: Multimodel analysis and implications for our perception of the land surface, *Bulletin of the American Meteorological Society*, Vol. *87*, pp. 1381-1397.

Dirmeyer, P. A., Z. Guo and X. Gao (2004), Comparison, validation, and transferability of

eight multiyear global soil wetness products, *Journal of Hydrometeorology*, Vol. *5*, pp. 1011.

Drusch, M., E. F. Wood, H. Gao and A. Thiele (2004), Soil moisture retrieval during the Southern Great Plains Hydrology Experiment 1999: A comparison between experimental remote sensing data and operational products, *Water Resources Research*, Vol. *40*.

Dubois, P. C., J. van Zyl and T. Engman (1995), Measuring soil moisture with imaging radars, *IEEE Transactions on Geoscience and Remote Sensing*, Vol. *33*, pp. 915.

Eagleman, J. R. and W. C. Lin (1976), REMOTE SENSING OF SOIL MOISTURE BY A 21-cm PASSIVE RADIOMETER, *J Geophys Res*, Vol. *81*, pp. 3660.

Early, D. S. and D. G. Long (1997), Azimuthal modulation of C-band scatterometer over Southern Ocean sea ice, *IEEE Transactions on Geoscience and Remote Sensing*, Vol. *35*, pp. 1201.

Entekhabi, D., E. G. Njoku, P. Houser, M. Spencer, T. Doiron, Y. Kim, J. Smith, R. Girard, S. Belair, W. Crow, T. J. Jackson, Y. H. Kerr, J. S. Kimball, R. Koster, K. C. McDonald, P. E. O'Neill, T. Pultz, S. W. Running, J. Shi, E. Wood and J. Van Zyl (2004), The hydrosphere state (hydros) satellite mission: An earth system pathfinder for global mapping of soil moisture and land freeze/thaw, *IEEE Transactions on Geoscience and Remote Sensing*, Vol. *42*, pp. 2184.

Entin, J. K., A. Robock, K. Y. Vinnikov, S. E. Hollinger, S. X. Liu and A. Namkhai (2000), Temporal and spatial scales of observed soil moisture variations in the extratropics, *Journal of Geophysical Research-Atmospheres*, Vol. *105*, pp. 11865-11877.

Ferrazzoli, P., S. Paloscia, P. Pampaloni, G. Schiavon, S. Sigismondi and D. Solimini (1997), The potential of multifrequency polarimetric sar in assessing agricultural and arboreous biomass, *IEEE Transactions on Geoscience and Remote Sensing*, Vol. *35*.

Figa-Saldana, J., J. W. Wilson, E. Attema, R. Gelsthorpe, M. R. Drinkwater and A. Stoffelen (2002), The advanced scatterometer (ASCAT) on the meteorological operational (MetOp) platform: A follow on for European wind scatterometers, *Canadian Journal of Remote Sensing*, Vol. *28*, pp. 404-412.

Fontaine, B., S. Louvet and P. Roucou (2007), Fluctuations in annual cycles and inter-seasonal memory in West Africa: rainfall, soil moisture and heat fluxes, *Theoretical And Applied Climatology*, Vol. *88*, pp. 57-70.

Frison, P. L., E. Mougin and P. Hiernaux (1997), Observations and simulations of the ERS wind scatterometer response over a sahelian region, *Igarss '97 - 1997 International Geoscience And Remote Sensing Symposium,* Vol., pp. 1832-1834.

Fung, A. K. (1994), *Microwave Scattering and Emission Models and Their Applications*, pp. 592, Artech House Norwood, MA.

Fung, A. K., Z. Q. Li and K. S. Chen (1992), Backscattering From A Randomly Rough Dielectric Surface, *Ieee Transactions On Geoscience And Remote Sensing*, Vol. *30*, pp. 356-369.

Grippa, M. and I. H. Woodhouse (2003), Retrieval of bare soil and vegetation parameters from wind scatterometer measurements over three different climatic regions, *Remote Sensing of Environment*, Vol. *84*, pp. 16-24.

Hajnsek, I., E. Pottier and S. R. Cloude (2003), Inversion of surface parameters from po-

larimetric SAR, *IEEE Transactions on Geoscience and Remote Sensing*, Vol. *41*, pp. 727.

Hallikainen, M. T., F. T. Ulaby, M. C. Dobson, M. A. El-Rayes and L.-K. Wu (1985), microwave dielectric behavior of wet soil - part i: emprical models and experimental observations, *IEEE Transactions on Geoscience and Remote Sensing*, pp. 25.

Hawkins, R., E. Attema, R. Crapolicchio, P. Lecomte, J. Closa, P. Meadows and S. Srivastava (1999), Stability of Amazon Backscatter at C-band: Spaceborne Results from ERS-1/2 and RADARSAT-1, paper presented at CEOS SAR Workshop, ESA-SP450.

Hillel, D. (1998), *Introduction to Soil Physics*, pp. 365, Academic Press, San Diego.

Hoffman, P. (1998), *The Man Who Loved Only Numbers: The Story of Paul Erdos and the Search for Mathematical Truth*, pp. 238-239, Hyperion, New York.

Huete, A., K. Didan, T. Miura, E. P. Rodriguez, X. Gao and L. G. Ferreira (2002), Overview of the radiometric and biophysical performance of the MODIS vegetation indices, *Remote Sensing of Environment*, Vol. *83*, pp. 195.

Illston, B. G., J. B. Basara and K. C. Crawford (2004), Seasonal to interannual variations of soil moisture measured in Oklahoma, *International Journal of Climatology*, Vol. *24*, pp. 1883-1896.

ISO/GUM (1995), *Guide to the expression of uncertainty in measurement*, VIII, pp. 101, Bureau International des Poids et, Mesures, Genève.

Jackson, T. J., T. J. Schmugge and P. O'Neill (1982), passive microwave remote sensing of soil moisture from an aircraft platform, *Remote Sensing of Environment*, Vol. *14*, pp. 135-151.

Jarlan, L., P. Mazzega and E. Mougin (2002), Retrieval of land surface parameters in the Sahel from ERS wind scatterometer data: A "brute force" method, *Ieee Transactions On Geoscience And Remote Sensing*, Vol. *40*, pp. 2056-2062.

Karam, M. A., A. K. Fung, R. H. Lang and N. S. Chauhan (1992), A microwave scattering model for layered vegetation, *IEEE Transactions on Geoscience and Remote Sensing*, Vol. *30*, pp. 767.

Kerr, Y. H., P. Waldteufel, J.-P. Wigneron, J.-M. Martinuzzi, J. Font and M. Berger (2001), Soil moisture retrieval from space: The Soil Moisture and Ocean Salinity (SMOS) mission, *IEEE Transactions on Geoscience and Remote Sensing*, Vol. *39*, pp. 1729-1735.

Kidd, R. (2005), Discrete Global Grid Systems. ASCAT Soil Moisture Report Series, No. 4, Institute of Photogrammetry and Remote Sensing, Vienna University of Technology, Vienna.

Kirchner, J. (2001), Uncertainty Analysis and Error propagation, University of California, Berkeley, California.

Klaes, D. and K. Holmlund (2007), The EPS/Metop system: overview and first results, paper presented at Joint 2007 EUMETSAT Meteorological Satellite Conference and the 15th Satellite Meteorology & Oceanography Conference of the American Meteorological Society, Amsterdam, The Netherlands, 24-28 September 2007.

Klemes, V. (1983), Conceptualization and scale in hydrology, *Journal of Hydrology*, Vol. *65*, pp. 1-23.

Klir, G. J. and T. A. Folger (1988), *Fuzzy sets, uncertainty, and information*, pp. 355, Prentice-Hall Internat, London.

Kottek, M., J. Grieser, C. Beck, B. Rudolf and F. Rubel (2006), World map of the Koppen-Geiger climate classification updated, *Meteorologische Zeitschrift*, Vol. *15*, pp. 259-263.

Le Hegarat-Mascle, S., M. Zribi, F. Alem, A. Weisse and C. Loumagne (2002), Soil moisture estimation from ERS/SAR data: Toward an operational methodology, *Ieee Transactions On Geoscience And Remote Sensing*, Vol. *40*, pp. 2647-2658.

Lecomte, P. (1998), The ERS scatterometer instrument and the on-ground processing of its data, *Proceeding of Emerging Scatterometer Application Workshop ESTEC, Noordwijk, the Netherlands 5-7 October 1998*, Vol., pp. 241.

Lehner, B. and P. Doell (2004), Development and validation of a global database of lakes, reservoirs and wetlands, *Journal of Hydrology*, Vol. *296*, pp. 1-22.

Magagi, R. D. and Y. H. Kerr (2001), Estimating surface soil moisture and soil roughness over semiarid areas from the use of the copolarization ratio, *Remote Sensing of Environment*, Vol. *75*, pp. 432-445.

Mätzler, C. and E. Schanda (1984), Snow Mapping with Active Microwave Sensors, *International Journal of Remote Sensing*, *Vol. 5, No. 2*, pp. 247-355.

Metropolis, N. and S. Ulam (1949), The Monte Carlo Method, *Journal of the American Statistical Association*, Vol. *44*, pp. 335-341.

Moeremans, B. and S. Dautrebande (1998), Use of ERS SAR interferometric coherence and PRI images to evaluate crop height and soil moisture and to identify crops, *Remote Sensing For Agriculture, Ecosystems, And Hydrology*, Vol. *3499*, pp. 9-19.

Moran, M. S., D. C. Hymer, J. Qi and E. E. Sano (2000a), Soil moisture evaluation using multi-temporal synthetic aperture radar (SAR) in semiarid rangeland, *Agricultural and Forest Meteorology*, Vol. *105*, pp. 69.

Moran, M. S., D. C. Hymer, J. G. Qi and E. E. Sano (2000b), Soil moisture evaluation using multi-temporal synthetic aperture radar (SAR) in semiarid rangeland, *Agricultural and Forest Meteorology*, Vol. *105*, pp. 69-80.

Morgen, B. J. T. (1984), *Elements of simulation*, ed., XIII, 351 S. pp., Chapman & Hall, London.

Mougin, E., D. Loseen, S. Rambal, A. Gaston and P. Hiernaux (1995), A Regional Sahelian Grassland Model To Be Coupled With Multispectral Satellite Data .1. Model Description And Validation, *Remote Sensing Of Environment*, Vol. *52*, pp. 181-193.

Naderi, F. M., M. H. Freilich and D. G. Long (1991), Spaceborne radar measurement of wind velocity over the ocean--An overview of the NSCAT scatterometer system, *Proceedings of the IEEE*, Vol. *79*, pp. 850.

Niederreiter, H. (1992), *Random number generation and quasi-Monte Carlo metods*, pp. 241, Society for Industrial and Applied Mathematics, Philadelphia.

Njoku, E. G. and D. Entekhabi (1996), Passive microwave remote sensing of soil moisture, *Journal of Hydrology*, Vol. *184*, pp. 101.

Njoku, E. G., T. J. Jackson, V. Lakshmi, T. K. Chan and S. V. Nghiem (2003), Soil mois-

ture retrieval from AMSR-E, *Ieee Transactions on Geoscience and Remote Sensing*, Vol. *41*, pp. 215-229.

Njoku, E. G., W. J. Wilson, S. H. Yueh, S. J. Dinardo, F. K. Li, T. J. Jackson, V. Lakshmi and J. Bolten (2002), Observations of soil moisture using a passive and active low-frequency microwave airborne sensor during SGP99, *Ieee Transactions on Geoscience and Remote Sensing*, Vol. *40*, pp. 2659-2673.

Oh, Y., K. Sarabandi and F. T. Ulaby (1992), An Empirical-Model And An Inversion Technique For Radar Scattering From Bare Soil Surfaces, *Ieee Transactions On Geoscience And Remote Sensing*, Vol. *30*, pp. 370-381.

Oki, T. and S. Kanae (2006), Global hydrological cycles and world water resources, *Science*, Vol. *313*, pp. 1068.

Oldak, A., T. J. Jackson, P. Starks and R. Elliott (2003), Mapping near-surface soil moisture on regional scale using ERS-2 SAR data, *International Journal of Remote Sensing*, Vol. *24*, pp. 4579-4598.

Owe, M., R. de Jeu and J. Walker (2001), A methodology for surface soil moisture and vegetation optical depth retrieval using the microwave polarization difference index, *Ieee Transactions on Geoscience and Remote Sensing*, Vol. *39*, pp. 1643-1654.

Papadopoulos, C. E. and H. Yeung (2001), Uncertainty estimation and Monte Carlo simulation method, *Flow Measurement and Instrumentation*, Vol. *12*, pp. 291-298.

Parajka, J., V. Naeimi, G. Bloeschl, W. Wagner, R. Merz and K. Scipal (2006), Assimilating scatterometer soil moisture data into conceptual hydrologic models at the regional scale, *Hydrology and Earth System Sciences*, Vol. *10*, pp. 353-368.

Pellarin, T., J. C. Calvet and W. Wagner (2006), Evaluation of ERS scatterometer soil moisture products over a half-degree region in southwestern France, *Geophysical Research Letters*, Vol. *33*.

Pulliainen, J. T., T. Manninen and M. T. Hallikainen (1998), Application of ERS-1 wind scatterometer data to soil frost and soil moisture monitoring in boreal forest zone, *Ieee Transactions On Geoscience And Remote Sensing*, Vol. *36*, pp. 849-863.

Quesney, A., S. Le Hegarat-Mascle, O. Taconet, D. Vidal-Madjar, J. P. Wigneron, C. Loumagne and M. Normand (2000), Estimation of watershed soil moisture index from ERS/SAR data, *Remote Sensing of Environment*, Vol. *72*, pp. 290-303.

Renze, J. "Outlier." From MathWorld--A Wolfram Web Resource, created by Eric W. Weisstein.

Robock, A., C. A. Schlosser, K. Y. Vinnikov, N. A. Speranskaya, J. K. Entin and S. Qiu (1998), Evaluation of the AMIP soil moisture simulations, *Global and Planetary Change*, Vol. *19*, pp. 181-208.

Ruediger, C., J.-C. Calvet, C. Gruhier, T. Holmes, R. de Jeu and W. Wagner (2008), An Intercomparison of ERS-Scat and AMSR-E Soil Moisture Observations with Model Simulations over France, *Journal of Hydrometeorology*, *preprint*.

Saatchi, S. S., D. M. Le Vine and R. H. Lang (1994), Microwave backscattering and emission model for grass canopies, *IEEE Transactions on Geoscience and Remote Sensing*, Vol. *32*, pp. 177.

Schanda, E. (1986), *Physical fundamentals of remote sensing*, pp. 187, Springer, Berlin.

Schmugge, J. and T. Jackson (1996), Soil moisture variability, in *Scaling up in hydrology using remote sensing*, edited by J. B. Steward, E. T. Engman, R. A. Feddes and Y. Kerr, pp. 183-192, John Wiley & Sons, New York.

Schmugge, T., P. Gloersen, T. Wilheit and F. Geiger (1974), Remote Sensing Of Soil Moisture With Microwave Radiometers, *J Geophys Res*, Vol. *79*, pp. 317.

Scipal, K. (2002), Global Soil Moisture Monitoring using ERS Scatterometer Data, Dissertation thesis, Vienna University of Technology.

Scipal, K., M. Drusch and W. Wagner (2008), Assimilation of a ERS scatterometer derived soil moisture index in the ECMWF numerical weather prediction system, *Advances in Water Resources*, Vol. *31*, pp. 1101-1112.

Scipal, K., C. Scheffler and W. Wagner (2005), Soil moisture-runoff relation at the catchment scale as observed with coarse resolution microwave remote sensing, *Hydrology and Earth System Sciences*, Vol. *9*, pp. 173-183.

Stern, F., M. Muste, M.-L. Beninati and W. E. Eichinger (1999), Summary of experimental uncertainty assessment methodology with example, 37, Iowa Institute of Hydralic Research, College of Engineering, The University of Iowa, Iowa City.

Taconet, O., M. Benallegue, D. Vidal-Madjar, L. Prevot, M. Dechambre and M. Normand (1994), Estimation of soil and crop parameters for wheat from airborne radar backscattering data in C and X bands, *Remote Sensing of Environment*, Vol. *50*, pp. 287-294.

Topp, G. C., J. L. Davis and A. P. Annan (1980), Electromagnetic determination of soil water content: measurements in coaxial transmission lines, *Water Resources Research*, Vol. *16*, pp. 574.

Ulaby, F. T., R. K. Moore and A. K. Fung (1982), *Microwave remote sensing: active and passive. Volume II. Radar remote sensing and surface scattering and emission theory.*

Ulaby, F. T., R. K. Moore and A. K. Fung (1986), *Microwave remote sensing: active and passive. Volume III: from theory to applications*.

Ulaby, F. T., K. Sarabandi, K. McDonald, M. Whitt and M. C. Dobson (1990), Michigan microwave canopy scattering model, *International Journal of Remote Sensing*, Vol. *11*, pp. 1223.

Unesco (2006), United Nations World Water Developement Report 2, Water, a Shared Responsibility, p.121, Paris.

USGS (1996), GTOP30, Global Digital Elevation Model Dataset, US Geological Survey, US Geological Survey, Sioux Falls.

USGS (1999), GLCC, Global Land Cover Characteristics Data Base, US Geological Survey, US Geological Survey.

Van De Griend, A. A. and M. Owe (1993), Determination of microwave vegetation optical depth and single scattering albedo from large scale soil moisture and Nimbus/SMMR satellite observations, *International Journal of Remote Sensing*, Vol. 14, pp. 1875.

Van den Hurk, B. J. J. M., P. Viterbo, A. C. M. Beljaars and A. K. Betts (2000), *Offline Validation of the ERA-40 Surface Scheme*, pp. 43.

Verstraeten, W. W., F. Veroustraete, C. J. Van Der Sande, I. Grootaers and J. Feyen (2006), Soil moisture retrieval using thermal inertia, determined with visible and thermal

spaceborne data, validated for European forests, *Remote Sensing of Environment*, Vol. *101*, pp. 299.

Vinnikov, K. Y., A. Robock, S. A. Qiu, J. K. Entin, M. Owe, B. J. Choudhury, S. E. Hollinger and E. G. Njoku (1999), Satellite remote sensing of soil moisture in Illinois, United States, *Journal of Geophysical Research-Atmospheres*, Vol. *104*, pp. 4145-4168.

Vischel, T., G. G. S. Pegram, S. Sinclair, W. Wagner and A. Bartsch (2008), Comparison of soil moisture fields estimated by catchment modelling and remote sensing: A case study in South Africa, *Hydrology and Earth System Sciences*, Vol. *12*, pp. 751-767.

Wagner, W. (1995), Application of Low-Resolution Active Microwave Remote Sensing (C-Band) over the Canadian Prairies, Diploma Thesis, Vienna University of Technology, Vienna.

Wagner, W. (1998a), Soil Moisture Retrieval from ERS Scatterometer Data, dissertation, Dissertation thesis, pp. 111, Vienna University of Technology, Vienna.

Wagner, W. (1998b), Vegetation cover effects on ERS Scatterometer data, Technical Note No. 1.98.05, 193p, EC Joint Research Centre, Ispra, Italy.

Wagner, W., G. Blöschl, P. Pampaloni, J. C. Calvet, B. Bizzarri, J. P. Wigneron and Y. Kerr (2007), Operational readiness of microwave remote sensing of soil moisture for hydrologic applications, *Nordic Hydrology*, Vol. *38*, pp. 1-20.

Wagner, W., G. Lemoine, M. Borgeaud and H. Rott (1999a), A study of vegetation cover effects on ERS scatterometer data, *Ieee Transactions on Geoscience and Remote Sensing*, Vol. *37*, pp. 938-948.

Wagner, W., G. Lemoine and H. Rott (1999b), A method for estimating soil moisture from ERS scatterometer and soil data, *Remote Sensing of Environment*, Vol. *70*, 191-207.

Wagner, W., J. Noll, M. Borgeaud and H. Rott (1999c), Monitoring soil moisture over the Canadian Prairies with the ERS scatterometer, *Ieee Transactions on Geoscience and Remote Sensing*, Vol. *37*, pp. 206-216.

Wagner, W., K. Scipal, C. Pathe, D. Gerten, W. Lucht and B. Rudolf (2003), Evaluation of the agreement between the first global remotely sensed soil moisture data with model and precipitation data, *Journal of Geophysical Research-Atmospheres*, Vol. *108*.

Wang, J. R. and T. J. Schmugge (1980), empirical model for the complex dielectric permittivity of soils as a function of water content, *IEEE Transactions on Geoscience and Remote Sensing*, Vol. *GE-18*, pp. 288.

Western, A. W., G. Blöschl and R. B. Grayson (1998), Geostatistical characterisation of soil moisture patterns in the Tarrawarra catchment, *Journal of Hydrology*, Vol. *205*, pp. 20.

Western, A. W., R. B. Grayson and G. Blöschl (2002), Scaling of soil moisture: A hydrologic perspective, in *Annual Review of Earth and Planetary Sciences*, pp. 149.

White, M. A., S. W. Running and P. E. Thornton (1999), The impact of growing-season length variability on carbon assimilation and evapotranspiration over 88 years in the eastern US deciduous forest, *International Journal of Biometeorology*, Vol. *42*, pp. 139-145.

Wigneron, J. P., P. Ferrazzoli, A. Olioso, P. Bertuzzi and A. Chanzy (1999), A simple approach to monitor crop biomass from C-band radar data, *Remote Sensing of Environment*, Vol. *69*, pp. 179.

Wigneron, J. P., Y. Kerr, A. Chanzy and Y. Q. Jin (1993), Inversion of surface parameters from passive microwave measurements over a soybean field, *Remote Sensing of Environment*, Vol. *46*, pp. 61.

Wilson, J. J. W., J. F. Saldana and E. O'Clerigh (2005), ASCAT Product Generation Function Specification, 210, EUMETSAT.

Woodhouse, I. H. and D. H. Hoekman (2000), Determining land-surface parameters from the ERS wind scatterometer, *IEEE Transactions On Geoscience And Remote Sensing*, Vol. *38*, pp. 126-140.

Woodhouse, I. H., J. J. van der Sanden and D. H. Hoekman (1999), Scatterometer observations of seasonal backscatter variation over tropical rain forest, *IEEE Transactions on Geoscience and Remote Sensing*, Vol. *37*, pp. 859.

Zhang, X. Y., M. A. Friedl, C. B. Schaaf, A. H. Strahler, J. C. F. Hodges and F. Gao (2002), *Using MODIS data to study the relation between climatic spatial variability and vegetation phenology in northern high latitudes*, pp. 1149-1151.

Zine, S., L. Jarlan, P. L. Frison, E. Mougin, P. Hiernaux and J. P. Rudant (2005), Land surface parameter monitoring with ERS scatterometer data over the Sahel: A comparison between agro-pastoral and pastoral areas, *Remote Sensing of Environment*, Vol. *96*, pp. 438.